AD-A256 714

$E201\ 272$

②

PL-TR-92-2003

REMOTE MEASUREMENT OF UPPER ATMOSPHERIC DENSITY: INSTRUMENT DEFINITION

P. B. Hays
J. H. Yee
V. J. Abreu

University of Michigan
Space Physics Research Laboratory
Ann Arbor, MI 48109-2143

DTIC
ELECTE
SEP 2 5 1992
S C D

3 December 1991

92   9 24 052

92-25828

PHILLIPS LABORATORY
Directorate of Geophysics
AIR FORCE SYSTEMS COMMAND
HANSCOM AIR FORCE BASE, MA 01731-5000

"This technical report has been reviewed and is approved for publication"

FRANK A. MARCOS
Contract Manager
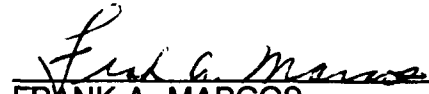
FRANK A. MARCOS
Branch Chief

FOR THE COMMANDER

WILLIAM K. VICKERY
Division Director

REPORT DOCUMENTATION PAGE

Form Approved
OMB No. 0704-0188

1. AGENCY USE ONLY (Leave blank)	2. REPORT DATE 3 December 1991	3. REPORT TYPE AND DATES COVERED Final (July 1988–October 1991)

4. TITLE AND SUBTITLE
Remote Measurement of Upper Atmospheric Density Instrument Definition

5. FUNDING NUMBERS
PE 62101F
PR 4643   TA 14   WU AB
Contract F19628-88-K-0032

6. AUTHOR(S)
P.B. Hays
J. H. Yee
V. J. Abreu

7. PERFORMING ORGANIZATION NAME(S) AND ADDRESS(ES)
University of Michigan
Space Physics Research Laboratory
Ann Arbor, MI 48109-2143

8. PERFORMING ORGANIZATION REPORT NUMBER

9. SPONSORING / MONITORING AGENCY NAME(S) AND ADDRESS(ES)
Phillips Laboratory
Hanscom AFB, MA 01731-5000

Contract Manager: Frank Marcos/GIS

10. SPONSORING / MONITORING AGENCY REPORT NUMBER
PL-TR-92-2003

11. SUPPLEMENTARY NOTES

12a. DISTRIBUTION / AVAILABILITY STATEMENT
Approved for public release; distribution unlimited

12b. DISTRIBUTION CODE

13. ABSTRACT (Maximum 200 words)

A study conducted previously at the Space Physics Research Laboratory, University of Michigan (Hays et al., 1988) has concluded that measurement of the spectral intensity of the O_2 Atmospheric band is the most feasible technique. The basic determination of the temperature can be accomplished using the optically thin transition from $O_2(^1\Sigma)$ to $O_2(^3\Sigma)$ in the (0-1) band; here local atmospheric temperature is determined uniquely by the rotational development of the emission band since the band is in thermal dynamic equilibrium. The density of molecular oxygen is determined from the (0-0) band of the same system; here self absorption by molecular oxygen is responsible for a reduction in intensity of the stronger lines in the system. This remote sensing technique has been proven to be feasible by rocket spectroscopic measurements during this funding period.

This report describes the remote sensing techniques and the optical instrument used. The results obtained from the rocket experiment are presented with evaluation of the magnitude of all the possible sources of error. A conceptual design of the instrument to implement this remote sensing technique from a satellite platform is also prepared which identifies the major hardware elements required.

14. SUBJECT TERMS
Atmospheric density
Satellite remote sensing
Resonance flourescence
Rayleigh scattering
Stellar occultation

15. NUMBER OF PAGES
86

16. PRICE CODE

17. SECURITY CLASSIFICATION OF REPORT	18. SECURITY CLASSIFICATION OF THIS PAGE	19. SECURITY CLASSIFICATION OF ABSTRACT	20. LIMITATION OF ABSTRACT
Unclassified	Unclassified	Unclassified	

Table of Contents

1. Introduction

Orbital reentry of large maneuverable vehicles and the potential to modify orbital parameters using the aerobraking technique have increased the need to understand in detail the variability of atmospheric density in the mesosphere and lower thermosphere. Acceleration data obtained during shuttle reentry illustrate the fact that the atmosphere exhibits variation which often exceeds expectation and which raise questions regarding the safe return of heavy Shuttle payloads from polar orbit. Prediction and specification of neutral density and temperature are also needed to support a variety of Air Force applications.

The variability of mass density in the mesosphere has been apparent for many years, being seen in sounding rocket data, backscatter radar profiles, and airglow optical emissions (Wasser and Donahue, 1979). The systematic variations that have been determined from these data sets are the obvious seasonal, latitudinal, and local time dependencies that are prescribed in the major models in use today. These models, however, are based on limited data and thus, are not useful in making predictions or forecasts of the effects of planetary waves or gravity wave breaking. The wave processes will never be accurately predicted, but like the weather in the troposphere we may ultimately be able to base a forecast on operational information. The primary factor holding back the improvement of these models and the development of a forecasting technique is the lack of a sufficiently large and accurate morphological data base in order to completely understand the thermal and dynamical processes in the region.

The successful launches of the Dynamics Explorer and Solar Mesosphere Explorer satellites have led to advances in our understanding of the upper thermosphere and to a lesser extent the mesosphere. These satellites were largely devoted to studies of large-scale (order of thousands of kilometers) features of Earth's upper atmosphere; for example, the seasonal and latitudinal variations in its composition, chemistry, and dynamics. The mesosphere and lower thermosphere have also been the subjects of a great deal of recent study by ground-based and other suborbital techniques, as well as theoretical and modeling work, but a global view of this region is still lacking. In the past five years, important questions have been raised regarding the basic processes that control the dynamics and chemistry of the mesosphere-lower thermosphere region. In particular, it has long been suspected that small-scale frictional processes (e.g., gravity waves) might be of substantial importance in the thermal and momentum balances of the upper part of Earth's atmosphere. The coupling between small-scale waves and the large-scale circulation and transport of the Earth's upper atmosphere is a new and challenging question whose further exploration requires global observations.

This global data base must rely on sampling techniques to provide morphologies of various atmospheric parameters, including the atmospheric density and temperature, in the critical 60 to

1

120 km region, with the consistency required to quantify the higher frequency variability. The only practical method of providing global information is to use a remote sensing technique from Earth orbit, given a technique that has the required accuracy and spatial sensitivity. Several possible techniques have been proposed which have the potential to measure the density in this important atmospheric region. These include measuring the brightness of sunlight that is rayleigh scattered by the molecular nitrogen and oxygen, measuring the absorption of starlight during stellar occultation, and measuring the intensity of molecular oxygen resonance fluorescence. A study conducted previously at the Space Physics Research Laboratory, University of Michigan (Hays et al., 1988) has concluded that measurement of the spectral intensity of the O_2 Atmospheric band is the most feasible technique. The O_2 Atmospheric system is extremely bright in both the daytime and nighttime emission airglow spectra and offers one of the best possible sources of information about the density structure in the upper mesosphere and lower thermosphere. Such a technique could be tested using first sub-orbital evaluation, and then deployment on a satellite in Earth orbit to provide the required global information.

We have developed an instrument dedicated to the remote sensing of the thermal structure and density of the atmosphere. The instrument, Density and Temperature Spectrometer (DATES), is a 1/4 meter Ebert Fastie Spectrometer using charge-couple devices (CCD) as its detector and was flown successfully on board the Michigan Airglow Package (MAP) NASA rocket in July 1989. It measures the spectral intensities of the (0-0) and (0-1) 'Atmospheric' bands of molecular oxygen, $O_2(^1\Sigma)$-$O_2(^3\Sigma)$. The basic determination of the temperature is accomplished using the optically thin transition from $O_2(^1\Sigma)$ to $O_2(^3\Sigma)$ in the (0-1) band; here local atmospheric temperature is determined uniquely by the rotational development of the emission band since the band is in thermal dynamic equilibrium. The density of molecular oxygen is determined from the (0-0) band of the same system; here self-absorption by molecular oxygen is responsible for a reduction in intensity of the stronger lines in the system.

This report describes the techniques for the remote sensing of upper atmospheric density and temperature and the type of optical instruments which were employed. The results obtained from the rocket experiment are presented with an evaluation of magnitudes of all the possible sources of error. The successful MAP flight has clearly demonstrated that the density and temperature profiles in the region between 60 and 120 km can be remotely measured through spectroscopic measurements of the O_2 atmospheric band emissions. Global measurements of this kind can provide a new capability for atmospheric model development and validation. A conceptual design of the instrument which implements this remote sensing technique from a satellite platform is also presented with the major required hardware elements identified.

2. Scientific Background and Objectives

The zonally averaged temperature structure of Earth's atmosphere is influenced by both radiative and dynamical processes. In the limit where absorption of solar radiation and emission of infrared radiation control the temperature distribution, the atmosphere can be said to be in radiative equilibrium, and variations in temperature as a function of latitude and season reflect the variations in these radiative processes. It is well known that Earth's stratosphere is fairly close to radiative equilibrium, with a warm summer stratopause and a cold winter stratopause reflecting to a substantial degree the differences in insolation as a function of season. While there are important departures from radiative equilibrium in the stratosphere, none is quite so striking as that of the high-latitude mesopause region. In contrast to the stratopause, the summer mesopause temperatures are only about 140-160K at high latitudes, approximately 50-70K colder than the high-latitude winter mesopause, even though the latter receives little or no solar radiation to provide this warmth. Thus it is clear that dynamical processes must be sufficiently rapid in the mesopause region to reverse the temperature structure that would be expected on purely radiative grounds.

The fundamental forcing mechanism responsible for driving the mesosphere away from radiative equilibrium is the momentum deposition associated with atmospheric waves. Leovy (1964) showed that the temperature and wind distributions of the mesosphere could be explained by a frictional deceleration of the zonal winds due to wave processes acting with a damping time of the order of ten days. More recent studies have shown that the radiative cooling rate in the mesosphere is even faster than hitherto believed, requiring an even faster damping time and a very rapid rate of frictional dissipation. Recent work shows that gravity waves generated in the troposphere will reach such large amplitudes at mesospheric levels that they will become convectively unstable and "break", producing momentum deposition or "friction" to decelerate the zonal winds and mixing chemical species. Theoretical studies employing parameterizations of gravity waves have achieved substantial success in modeling the average temperature and wind distributions of the mesosphere and lower thermosphere (e.g., Holton, 1982); it is particularly important to note that the strong temperature reversal near the high latitude mesosphere can be simulated by models employing such a description of the frictional processes acting in the mesosphere.

In contrast to the mesosphere, the lower thermosphere, like the stratosphere, is warm in summer and cold in winter, reflecting the fact that heating by absorption of solar radiation in the Schumann-Runge continuum and EUV regions dominates the energy balance. In addition to solar heating there is a strong heat source caused by auroral particle precipitation and Joule dissipation of ionospheric currents at high magnetic conjugate latitudes. In the mean this auroral heat source reinforces the summer-to-winter circulation in the summer hemisphere but opposes the summer-to-winter circulation in the winter hemisphere. Since the auroral heat source is highly variable and depends upon geomagnetic activity, there are correspondingly large variations in the temperature

structure in the thermosphere driven by variable solar and auroral processes (Roble et al., 1977). The aurora is a source of both large-scale propagating disturbances and smaller-scale acoustic-gravity waves that propagate disturbances equatorward from the auroral zone in the lower and the upper thermosphere. These waves are also in part responsible for the large variability observed in both the upper and lower thermosphere.

Even though the upper thermosphere has been studied extensively, there are still many unresolved problems, and, especially, the mutual interactions between the upper and lower thermosphere are poorly understood. The global dynamics of the lower thermosphere is virtually unknown but it is expected to differ considerably from that at F-region heights, which is dominated by strong ion drag forces, and from that in the mesosphere, which is primarily in geostrophic balance. The forcings in the lower thermosphere are also different from the forcings in other atmospheric regions. The changing solar optical depth in the thermosphere generates semi-diurnal, in situ components that maximize in the lower thermosphere below 200 km. The semi-diurnal components are driven by both in situ solar heating and by upward-propagating, semi-diurnal tides that are excited in the lower atmosphere. These semi-diurnal components dominate atmospheric motions, temperature, and compositional distributions of the lower thermosphere (Fesen et al., 1986); but their global structure, seasonal variations, and response to geomagnetic storms,stratospheric warmings, solar flares, etc., are not known. Knowledge of the tidal structures in temperature and density in the lower thermosphere is important for understanding dynamo processes at low and mid-latitudes.

In the lower thermosphere below about 150 km, the importance of the ion drag force, which strongly controls F-region dynamics, diminishes and becomes comparable to the coriolis force. As a result, the dynamics of the high-latitude lower thermosphere is unique in the atmosphere, acting somewhere between the geostrophic-type circulation in the lower atmosphere and the counter pressure gradient subsolar-to-antisolar circulation in the upper thermosphere. At times, especially during strong auroral activity, the high-latitude lower thermosphere can be driven by ion drag associated with magnetospheric convection. These forcings are transient, generally following geomagnetic activity, and they have been predicted to generate long-lived vortices at high latitudes that persist for many hours after the forcings subside and can wander from their point of generation much as certain vortices do in the lower atmosphere and oceans. Warm, high-pressure anticyclonic and cold, low-pressure cyclonic vortices have been predicted (Fuller-Rowell and Rees, 1981; Roble et al., 1982) that have the capability of trapping certain auroral-generated minor species such as NO. Variation in chemical reactions and radiational process are also governed by these dynamic processes because of dynamically induced composition changes and temperature-sensitive chemical reaction rates that have an important influence on the structure of the entire thermosphere (Gerard and Roble, 1986). Lindzen (1967, 1968, 1981) has argued that the solar diurnal tide should become unstable and break at altitudes near and above 90 km in the tropics. This will certainly produce mixing of chemical species in this region, and the associated

4

momentum deposition is likely to be of importance in driving the large-scale circulation there. Similarly, planetary waves break and dissipate in the middle- and high-latitude winter mesosphere. These waves can be particularly important in their modulation of the propagation of gravity waves (see, e.g., Dunkerton, 1982; Schoeberl et al., 1983). It has also been suggested that planetary scale waves may themselves be generated by breaking small-scale gravity waves (Holton, 1983). Thus it is clear that wave phenomena are of critical importance to the transport and dynamics of the mesosphere and lower thermosphere. It is likely that a spectrum of waves ranging from the smallest physical scales, such as gravity waves, to those of global extent, such as tides, all contribute individually and collectively to determine the structure of the Earth's upper atmosphere.

The energy budget of the lower thermosphere and upper mesosphere is not well understood or quantified at present. A primary heat source to the lower thermosphere, between 90 and 150 km, is the absorption of solar radiation in the Schumann-Runge continuum. Photons in this range are able to dissociate molecular oxygen, producing metastable atomic oxygen in the $O(^1D)$ state that are subsequently collisionally quenched, releasing their excess energy to the ambient gas. This, relatively well-understood heat source is, however, augmented by other, less well-quantified sources and sinks of energy. Note here that the quenching of $O(^1D)$ by O_2 gives rise to the O_2 Atmospheric band emissions that DATES is measuring. The highly variable Joule and particle heat sources, for example, peak in the lower thermosphere at high latitudes, inducing significant dynamical and transport phenomena and modifying the thermal structure both locally and, via circulation processes, on a global scale. While DATES will not directly measure all the necessary parameters to quantify these sources of heating, it will provide a full description of thermodynamic response of the mesosphere and lower thermosphere to the time-varying sources of high-latitude energy and momentum.

Also of unknown significance to the energy budget of this region are the dissipative processes associated with tides, gravity waves, and turbulence. Indirect evidence discussed above involving emission rates and turbulence echoes from radar together with chemical/dynamical modeling considerations have demonstrated the importance of the breaking of gravity waves for the dynamics and chemistry of the upper mesosphere-lower thermosphere, but the implications for the energy budget of the region are not known. Furthermore, recent modeling studies indicate that the energy released through the dissipation of the solar semi-diurnal tides can be commensurate with the Schumann-Runge source and that the tidal source of energy has a specific latitudinal/altitudinal distribution which, of itself, would have important consequences for global circulation. DATES measurements of tidal parameters (temperature and density components) will enable these heat sources to be investigated using theoretical models with a vastly improved observational database.

The number densities of metastable $O(^1D)$ atoms and O_3 molecules can also be derived from the measured $O_2(^1\Sigma)$ number density profile. O_3 is important because of its role in the radiation

(thermal) budget of the atmosphere. The concentration of ozone in this region of the atmosphere has usually been indirectly inferred from the $O_2(^1\Delta)$ 1.27 μm emission produced by the photolysis of O_3. The concentration of $O(^1D)$ atoms in this region is low, approximately 10^2-10^3 cm^{-3}, and is very difficult to measure through the 6300Å emission because of the presence of rayleigh scattering. As described before, the $O(^1D)$ atoms are very important in the mesosphere and lower thermosphere due to their involvement in the HO_x chemistry, i.e. $O(^1D) + H_2O \rightarrow 2OH$ and $O(^1D) + H_2 \rightarrow H + OH$. DATES will provide, for the first time, a viable technique to infer the concentrations of these two important O_x species along with the concentration of the major species, O_2 and atmospheric temperature.

A number of empirical/theoretical models are available for the study of processes in the mesosphere and thermosphere. They are rather fully developed and often their predictive capability far outstrips the available experimental database. These models include:

(a) A zonally averaged, chemical-dynamic model of the Stratosphere-Mesosphere-Lower Thermosphere from about 15 to 120 km (Garcia and Solomon, 1983; Garcia and Solomon, 1985). This comprehensive model includes both large-scale diabatic motions as well as the influence of breaking gravity waves on the dynamics and chemical composition of the 60 to 110 km region. This model has illustrated the important role of gravity waves in controlling the distribution of many important minor constituents.

(b) A coupled, zonally averaged planetary wave model to study the three-dimensional structure of trace species in the mesosphere and lower thermosphere (Garcia et al., 1986). This model has successfully described nitric oxide transport and the structure of the D-region winter anomaly.

(c) A self-consistent global mean model of the coupled thermosphere, ionosphere and mesosphere has been developed to examine interactions between these regions and to develop parameterizations of chemical reaction and schemes that are being incorporated into the new Mesosphere/Thermosphere/Ionosphere General Circulation Model (MTIGCM).

(d) An empirical neutral density and wind model, the mass spectrometer-incoherent scatter MSIS-86 (Hedin, 1987). This model gives global distributions of temperature, O_2, N_2, O , He, H, Ar and N densities.

In general, DATES will provide direct measurements of the density and temperature fields in the lower thermosphere and mesosphere as a function of season, time, solar and magnetic activity levels, etc. with an accuracy far better than what the existing models can predict. The global database obtained by the DATES experiment will provide real-time measurements for the validation and improvement of these models for our detailed understanding of the complex physical, chemical and dynamical processes in the region.

3. Density and Temperature Measurement Description

The Atmospheric bands of molecular oxygen originate in a transition between the excited $b^1\Sigma_g^+$ state and the ground $X^3\Sigma_g^-$ state. The O_2 Atmospheric bands are one of the brightest emission features that are seen in the visible and near infra-red region of the airglow spectra. The total band brightness is strongly coupled to the O_2 density through both the excitation mechanisms and the self-absorption processes (for the 0-0 band), with the brightness of each rotational line determined by the atmospheric temperature. Here we will describe how the observed intensities of the O_2 Atmospheric bands are used to retrieve the O_2 number density and temperature profiles in the region between 60 and 120 km.

3.1 Theoretical Background

3.1.1 Spectral Intensity of the Atmospheric Bands

Figure 1 shows the viewing geometry of a spacecraft-borne instrument measuring limb brightnesses of the O_2 Atmospheric band emissions. The measured brightness is an integrated volume emission rate along the slant path associated with a particular tangent ray altitude. When the absorption is important, such as the O_2 Atmospheric (0-0) band, the measured brightness is modified by the attenuation along the path between production region and the spacecraft.

(1) $O_2 + h\nu \rightarrow O_2(^1\Sigma)$ (2) $O + O + M \rightarrow O^*_2 + M$

       $O_2(^1\Sigma_g) \rightarrow O_2(^1\Sigma_g) + h\nu$ $O^*_2 + O \rightarrow O_2(^1\Sigma_g) + O$

(3a) $O_2 + h\nu \rightarrow O(^1D) + O_2$ (3b) $O_3 + h\nu \rightarrow O(^1D) + O_2$

 $O(^1D) + O_2 \rightarrow O_2(^1\Sigma_g) + O$ $O(^1\Gamma) + O_2 \rightarrow O_2(^1\Sigma_g) + O$
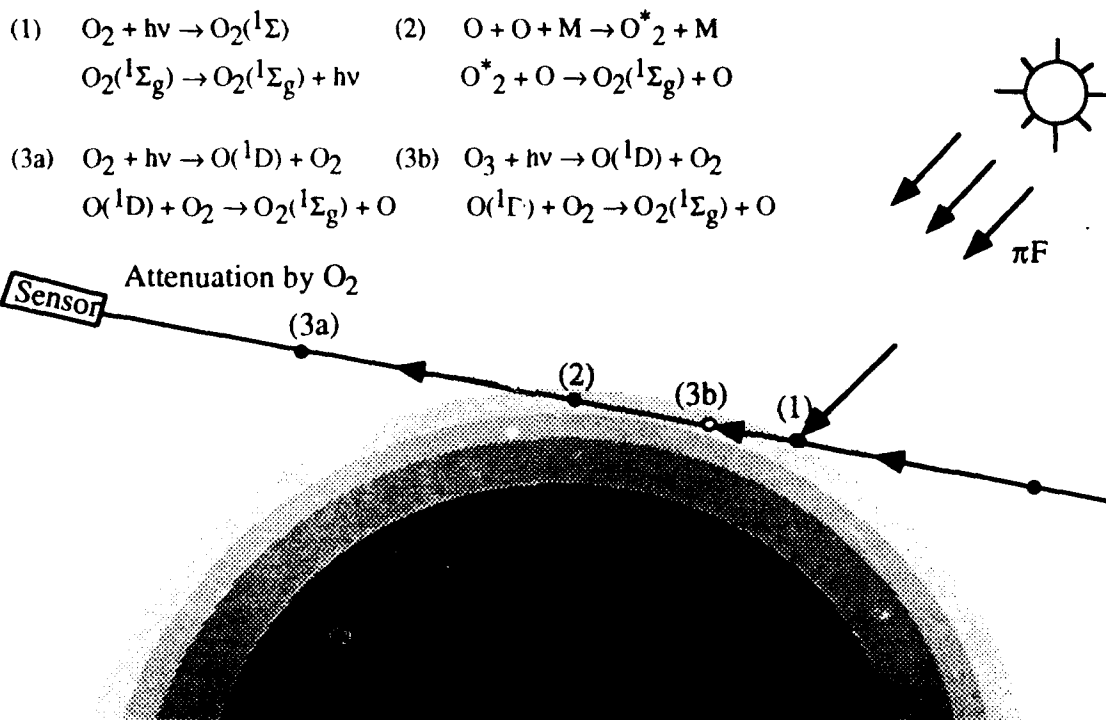
Figure 1

If we denote the total band volume emission rate at a point along the line of sight by $\eta(s)$, the observed spectral brightness, $B(\nu, z_t)$, of a rotational line at ν_j as a function of wavenumber ν and tangent height z_t is given by

$$B(\nu, z_t) = \int_{-\infty}^{\infty} \eta(s) \, f(s) \, D(\nu, s) \exp\left\{ -\int_{s}^{\infty} n(s') \, \sigma(s') \, D(\nu, s') \, ds' \right\} ds \tag{3.1}$$

where $f(s)$ is the line strength of the rotation line of interest, determined by the rotational temperature of the excited $O_2(b^1\Sigma_g^+)$ molecules and $\Sigma_{\text{all lines}} \, f = 1.0$, $D(\nu, s)$ is the line shape at temperature $T(s)$, $n(s')$ is the number density of O_2, and $\sigma(s)$ is the self-absorption cross-section.

Converting the line-of-sight integral in Eq. (3.1) to an integral in altitude z, one obtains

$$B(\nu, z_t) = \int_{z_t}^{\infty} \eta(z) \, f(z) \, D(\nu, z) \, W(z, z_t) \exp\left\{ -\Gamma(\nu, z, z_t) \right\} dz \tag{3.2}$$

$$+ \int_{z_t}^{\infty} \eta(z) \, f(z) \, D(\nu, z) \, W(z, z_t) \exp\left\{ -\Gamma(\nu, z_t \cdot z_t) - \tau(\nu, z, z_t) \right\} dz$$

where $W(z, z_t)$ is the Jacobian in the transformation $(W = \partial s / \partial z)$, or the geometric weighting function,

$$W(z, z_t) = \frac{R_e + z}{\sqrt{(R_e + z)^2 - (R_e + z_t)^2}}, \tag{3.3}$$

where R_e is Earth radius, and

$$\Gamma(\nu, z, z_t) = \int_{z}^{\infty} n(z') \, \sigma(z') \, D(\nu, z') \, W(z', z_t) \, dz', \tag{3.4}$$

$$\tau(\nu, z, z_t) = \int_{z_t}^{z} n(z') \, \sigma(z') \, D(\nu, z') \, W(z', z_t) \, dz'. \tag{3.5}$$

8

Since

$$\Gamma(v, z, z_t) = \Gamma(v, z_t, z_t) - \tau(v, z, z_t), \tag{3.6}$$

and by defining

$$\Gamma(v, z_t) = \Gamma(v, z_t, z_t), \tag{3.7}$$

we can rewrite Eq. (3.2) as

$$B(v, z_t) = 2 \int_{z_t}^{\infty} \eta(z) \, f(z) \, D(v, z) \, W(z, z_t) \exp\left[-\Gamma(v, z_t)\right] \cosh\left[\tau(v, z, z_t)\right] \, dz. \tag{3.8}$$

The above equation computes the spectral brightness, $B(v, z_t)$, of any given rotational line when the self-absorption process is considered. Since f, D and σ are a function of temperature the spectral brightness in this case not only depends upon the band volume emission rate and the O_2 number density profiles, but also on the atmospheric temperature profile. For emissions where the self-absorption process is not important, such as the O_2 Atmospheric (0-1) and (1-1) bands, Eq. (3.8) becomes the Abel integral equation (Hays et al., 1973),

$$B(v, z_t) = \int_{z_t}^{\infty} \eta(z) \, f(z) \, D(v, z) \, W(z, z_t) \, dz, \tag{3.9}$$

and the spectral brightness is determined by the volume emission rate and the atmospheric temperature profiles.

### 3.1.2 Characteristics of the O_2 Atmospheric Band Emission

O_2 Atmospheric Band Volume Emission Rate: The O_2 Atmospheric band system results from competition between processes which excite molecular oxygen to the $b^1\Sigma_g^+$ state and those that depopulate the state. They are:

A. Excitation processes
1. Resonance absorption (7650 Å)
$$O_2(X^3\Sigma) + hv \rightarrow O_2(b^1\Sigma)$$

9

2. Production of $O(^1D)$ and quenching (Ultra-violet)

$$O_2(X^3\Sigma) + h\nu \rightarrow O(^1D) + O(^3P)$$

$$O_3 + h\nu \rightarrow O(^1D) + O_2$$
Production
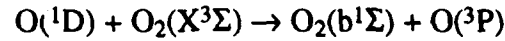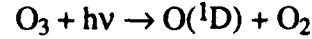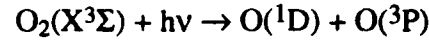
$$O(^1D) + O_2(X^3\Sigma) \rightarrow O_2(b^1\Sigma) + O(^3P)$$
Quenching

3. Chemical recombination

$$O(^3P) + O(^3P) + M \rightarrow O_2^* + M$$

$$O_2^* + O(^3P) \rightarrow O_2(b^1\Sigma) + O(^3P)$$
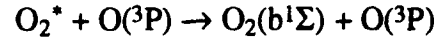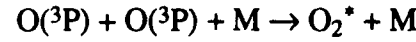
B. Loss processes
   1. Radiation
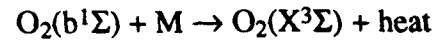
$$O_2(b^1\Sigma) \rightarrow O_2(X^3\Sigma) + h\nu$$

   2. Quenching

$$O_2(b^1\Sigma) + M \rightarrow O_2(X^3\Sigma) + heat$$

If we denote the various sources of production of $O_2(b^1\Sigma_g{}^+)$ by P_{res}, $P_{O(1D)}$ and P_{chem} and consider loss processes due to quenching and radiation in a simple photochemical equilibrium situation, we can determine the total band volume emission rate as a function of altitude,

$$\eta_{vv'}(z) = A_{vv''} \frac{P_{res} + P_{O(^1D)} + P_{chem}}{A_{1\Sigma} + k_{N_2} n_{N_2}(z) k_{O_2} n_{O_2}(z)}, \tag{3.10}$$

where $A_{v'v''}$ is the transition probability between $O_2(b^1\Sigma, v')$ and $O_2(X^3\Sigma, v'')$ states, $A_{1\Sigma}$ is the transition probability of $O_2(b^1\Sigma)$ state, and k_{N_2} and k_{O_2} are the quenching rate coefficients of $O_2(b^1\Sigma)$ by N_2 and O_2, respectively.

Figure 2 shows the volume emission rate profile of the (0,0) band in the daytime and its individual contribution due to each of the three production sources (Bucholtz et al., 1986). Note that the dominant sources of the excited $O_2(b^1\Sigma)$ molecules in the 60 to 130 km range are resonance scattering and reaction of $O(^1D)$ atom with O_2 followed by photodissociation of O_2. In a region above ~90 km where quenching of $O_2(b^1\Sigma)$ molecules is not important, the volume emission rate is therefore related to the number density of ground state O_2. As the quenching becomes important in the region between 60 and 90 km, the production rate and the loss rate of $O_2(b^1\Sigma_g{}^+)$ are both proportional to the molecular oxygen number density. As a result, the total band volume emission rate remains independent with altitude, and provides little information about the number density of O_2. The capability of retrieving atmospheric density in this region lies not on the volume emission rate profile, but on the important characteristics of the (0-0) band, the self absorption processes.
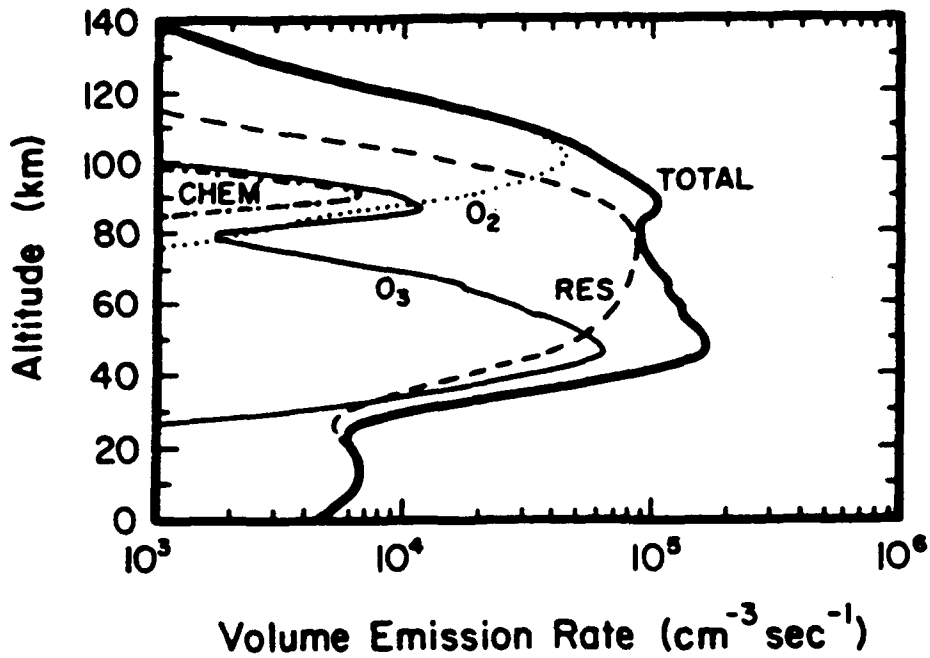
Figure 2

Temperature Effect: The spectral brightness of any given rotational line depends on the atmospheric temperature profile in two different ways. One is the thermal distribution of the rotational levels of both the emitter, the excited $O_2(b^1\Sigma_g^+)$ and the absorber, the ground state $O_2(X^3\Sigma_g^-)$. The former determines the line volume emission rate profile, while the latter determines the line absorption cross-section (McClatchey et al., 1973),

$$f = f_s \frac{T_s}{T} \exp\left\{\frac{1.439 \ E' \ (T - T_s)}{T\,T_s}\right\},$$

(3.11)

$$\sigma = \sigma_s \frac{T_s}{T} \exp\left\{\frac{1.439 \ E'' \ (T - T_s)}{T\,T_s}\right\},$$

(3.12)

where f_s is the emission line strength at standard temperature T_s, σ_s is the self-absorption cross-section at T_s, and E' and E" are the energies in cm^{-1} for the upper and lower states of the rotational line, respectively (Babcock and Herzberg, 1948).

Because collisions with the ambient atmospheric particles are very frequent in the region between 60 and 120 km, both the excited and the ground states of O_2 are in rotational thermal equilibrium and have a rotational temperature equal to the ambient kinetic temperature. Figure 3 presents the rotational line intensity distributions of the O_2 Atmospheric (0-1) band for 150 and 300°K, respectively. The band origin is located near 8645Å with the R-branch lines appearing on the

11

Figure 3

12
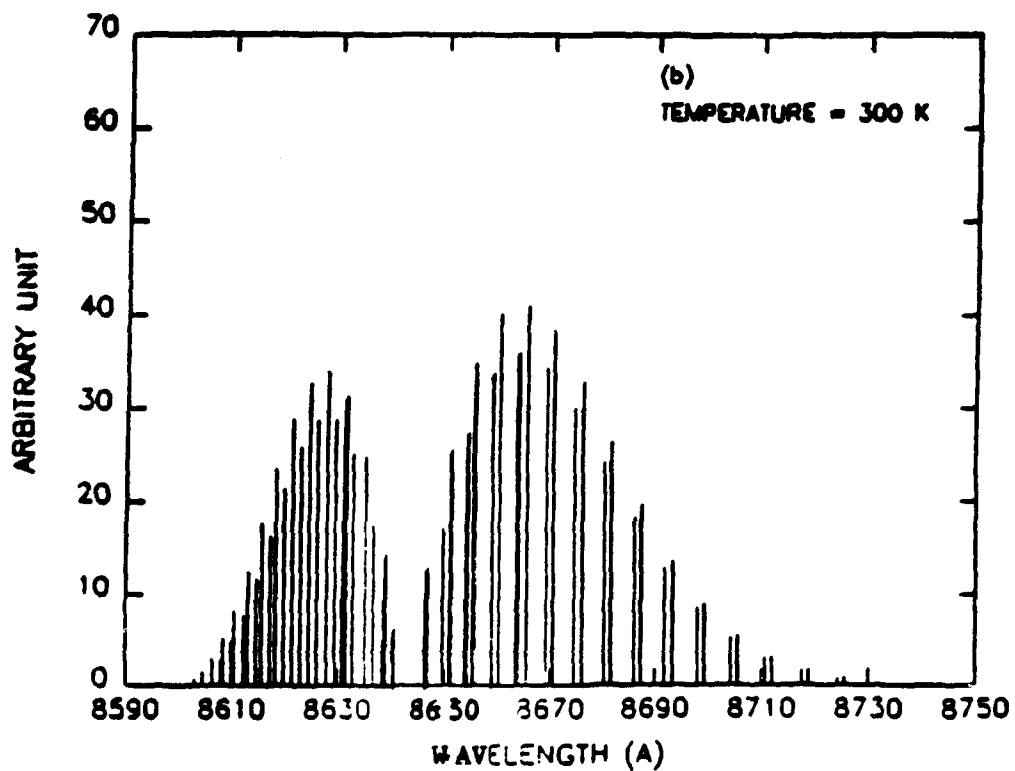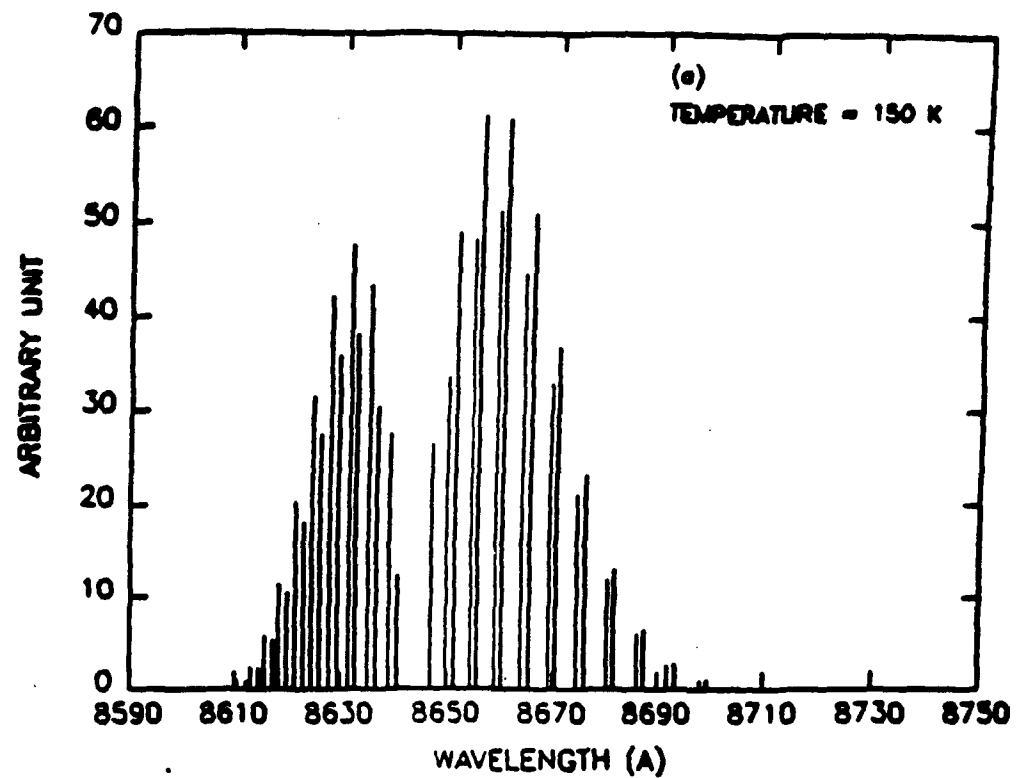
shorter wavelengths side and the P-branch lines appearing on the longer wavelength side. As the temperature increases, the lines near the bandhead and the bandtail, representing the transitions from higher rotational levels, become more pronounced. This apparent change in band structure can provide us with the temperature information of the atmosphere.

If the self-absorption process is important, such as for the O_2 Atmospheric (0-0) band emission, the band structure will be modified due to variations in extinction from line to line. Figure 4(a) shows the computed intensities of all the rotational lines in the O_2 Atmospheric (0-0) band at 60 km tangent height, and Fig. 4(b) shows the case when the self-absorption process is ignored. The effect of the self-absorption process is small for the lines near the bandhead and the bandtail whose line strengths are weak, and is large for lines near the band origin. The temperature deduced from the rotational band structure of the O_2 Atmospheric (0-0) band emission, therefore, is larger than the rotational temperature of the emitters.

The other temperature dependence arises when the spectral line shapes of the emission and the absorption cross-section are considered. In the region above 60 km the pressure broadening effect is not very important. The spectral shapes of the emission line and the self-absorption cross-section are determined by the kinetic temperatures of the excited state $O_2(b^1\Sigma_g^+)$ and the ground state $O_2(X^3\Sigma_g^-)$, respectively,

$$D(v, T) = \frac{1}{\alpha_D} \left(\frac{\ln 2}{\pi} \right)^{\frac{1}{2}} \exp\left(\frac{(v - v_o)^2 \ln 2}{\alpha_D^2} \right),$$

(3.13)

where v_o is the wavenumber at line center, and α_D is the doppler width,

$$\alpha_D = \frac{v_o}{c} \left(\frac{2kT \ln 2}{m} \right)^{\frac{1}{2}}.$$

(3.14)

13
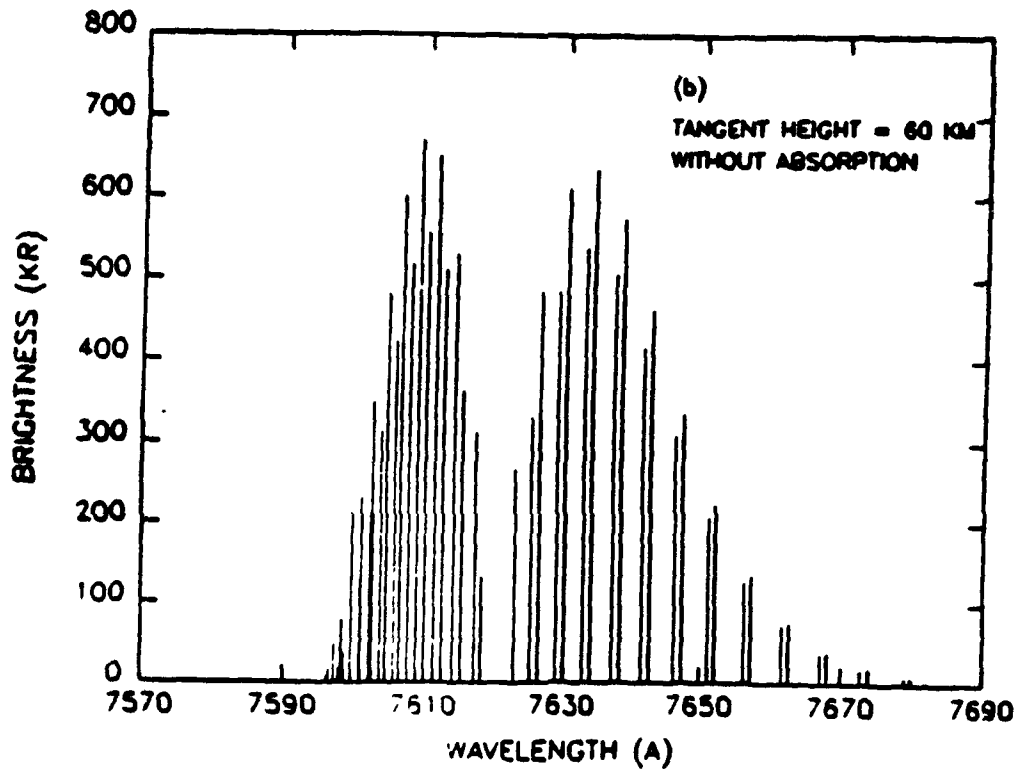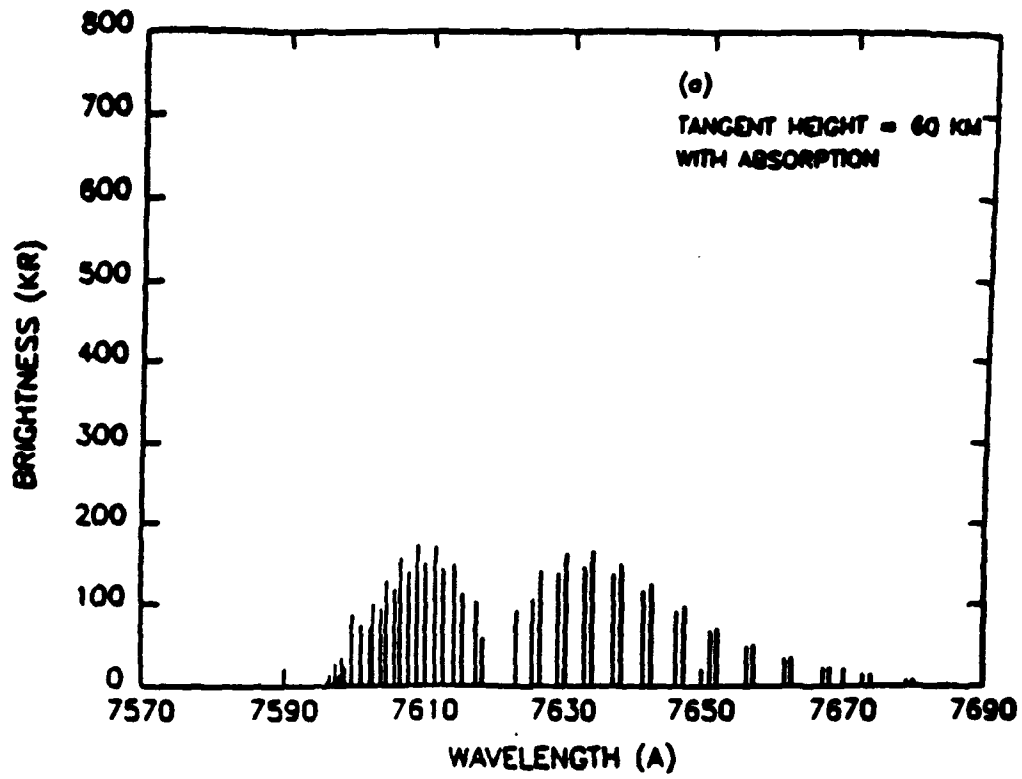
Figure 4

14

Figure 5 shows the emission line shape of line PP31 (13118.0332 cm-1) in the (0-0) band for a measurement at a tangent height of 60 km. The emission line shape for neglecting the self-absorption process is also shown. Since the magnitude of the self-absorption cross-section is the
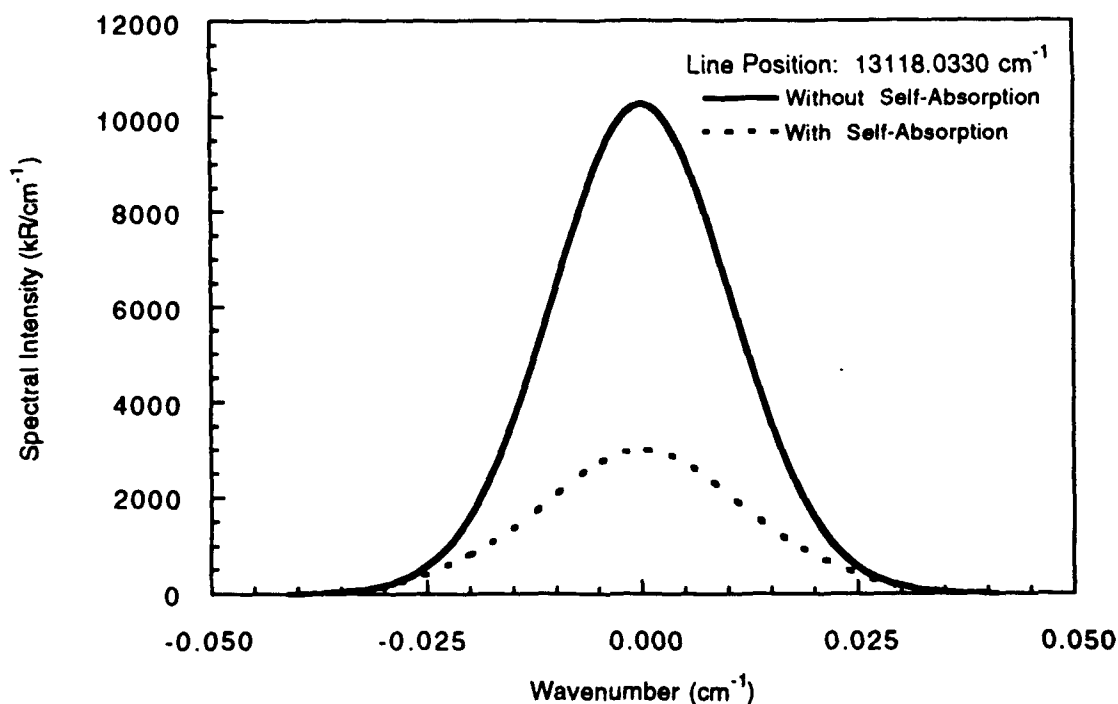
Figure 5

largest at the line center and decreases toward the wings, the effect of the self-absorption process gives rise to a broadened emission line shape and an effective temperature layer than the kinetic temperature of the emitters.

O_2 *Number Density:* One would also expect that emission spectral line shape at lower tangent heights will appear broader than the ones at higher tangent heights due to longer absorption paths and the larger extinctions near the line center. Consequently, the spectral intensity of lines in the (0-0) band not only contains the temperature information of the emitter, but also the column density of the absorber O_2.

Figure 4 clearly shows that for some rotational lines, approximately 60-80% of the intensities are absorbed. Figure 6 presents the intensity as a function of tangent height for the line shown in Fig. 5. The variation of the amount of self-absorption with tangent height reflects the variation of the O_2 column density. Hence, by measuring the extinction of the $O_2(0-0)$ band emission intensity as a function of tangent height, one can, in principle, determine the number density profile of O_2.

15
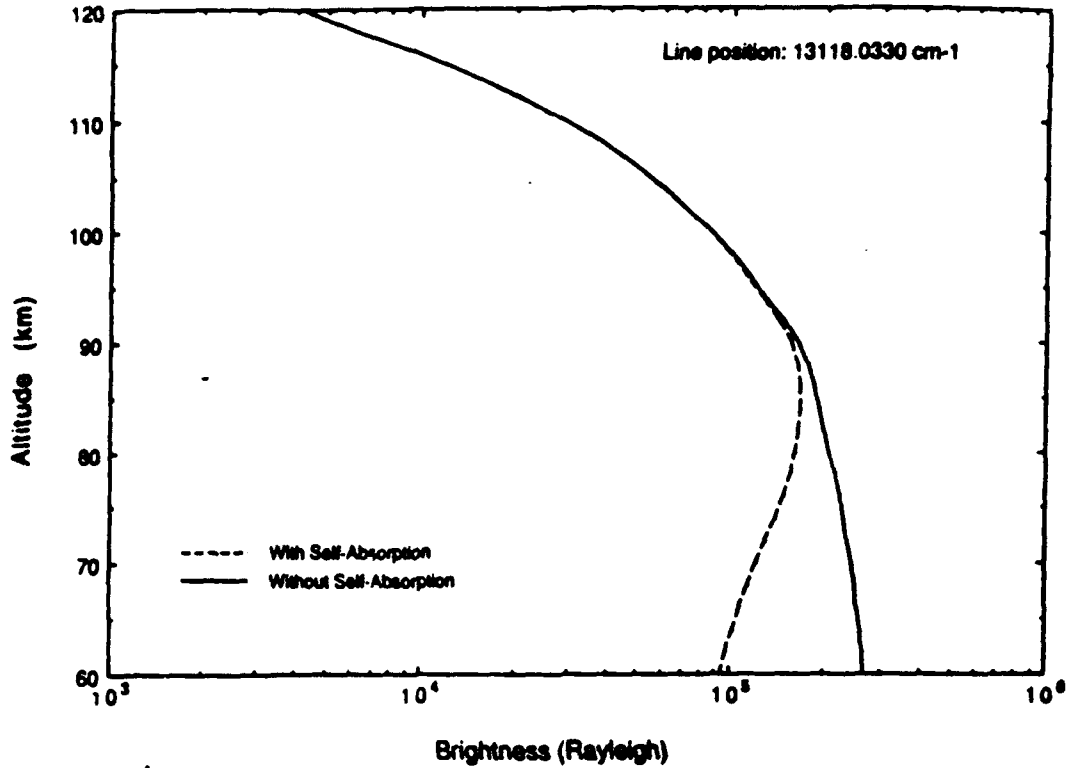
Figure 6

3.1.3 Recovery of Density and Temperature Profiles

3.1.3.1 Mathematical Formulation

As Eq. (3.8) indicates, the observed limb brightness $B(v, z_t)$ of an emission line in the O_2 Atmospheric (0-0) band is a non-linear function of the volume emission rate, temperature, and the O_2 number density profiles. Using linear perturbation theory, we can express actual $n(z)$, $T(z)$, and $\eta(z)$ profiles as sums of guessed profiles, $n_0(z), T_0(z)$ and $\eta_0(z)$ and small perturbations $n'(z), T'(z)$ and $\eta'(z)$, as follows:

$$n(z) = n_0(z) + n'(z), \qquad (3.15)$$

$$T(z) = T_0(z) + T'(z), \qquad (3.16)$$

and

$$\eta(z) = \eta_0(z) + \eta'(z). \qquad (3.17)$$

We shall see below that Eq. (3.8) can be simplified, expressing any observed limb brightness in terms of a linear combination of the volume emission rate, temperature and the O_2 number density profiles. The linear representation of the limb brightness can help us understand the relative importance or the contribution of the three parameters to the observed brightness.

16

Substituting Eqs. (3.15), (3.16) and (3.17) into the expressions for $\Gamma(v,z_t)$ and $\tau(v,z,z_t)$ and neglecting the terms involving the multiplication of two perturbations parameters, one obtains

$$\Gamma(v, z_t) = \Gamma_o(v, z_t) + \Gamma_T{}'(v, z_t) + \Gamma'_n(v, z_t), \tag{3.18}$$

and

$$\tau(v, z, z_t) = \tau_o(v, z, z_t) + \tau'_T(v, z, z_t) + \tau'_n(v, z, z_t), \tag{3.19}$$

where

$$\Gamma'_o(v, z_t, z_t) = \int_{z_t}^{\infty} n_o(z)\, \sigma_o(z)\, D_o(v, z)\, W(z, z_t)\, dz, \tag{3.20}$$

$$\Gamma'(v, z_t) = \int_{z_t}^{\infty} n_o(z)\, \frac{\partial(\sigma_o(z)\, D_o(v,z))}{\partial T}\, T'(z), \tag{3.21}$$

$$\Gamma'_n(v, z_t) = \int_{z_t}^{\infty} n'(z)\, \sigma_o(z)\, D_o(v, z)\, W(z, z_t)\, dz, \tag{3.22}$$

and

$$\tau_o(v, z, z_t) = \int_{z_t}^{z} n_o(z)\, \sigma_o(z)\, D_o(v, z)\, W(z, z_t)\, dz, \tag{3.23}$$

$$\tau'_T(v, z, z_t) = \int_{z_t}^{z} n_o(z)\, \frac{\partial(\sigma_o(z)\, D_o(v, z))}{\partial T}\, T'(z)\, W(z, z_t)\, dz, \tag{3.24}$$

$$\tau'_n(v, z, z_t) = \int_{z_t}^{z} n'(z)\, \sigma_o(z)\, D_o(v, z)\, W(z, z_t)\, dz. \tag{3.25}$$

The terms $e^{-\Gamma}$ and $\cosh(\tau)$ in Eq. (4) can then be expanded as

$$e^{\Gamma} = e^{-\Gamma_o}(1 - \Gamma'_T - \Gamma'_n), \tag{3.26}$$

$$\cosh(\tau) = \cosh(\tau_o) + (\tau'_T + \tau'_n)\, \sinh(\tau_o), \tag{3.27}$$

and Eq. (3.8) becomes

17

$$B(v, z_t) = B_o(v, z_t) + \int_{z_t}^{\infty} [\tau'_T(v, z, z_t) \, \alpha(v, z, z_t) - \Gamma'_T(v, z_t) \, \beta(v, z, z_t)] \, dz$$

$$+ \int_{z_t}^{\infty} [\tau'_n \alpha(v, z, z_t) - \Gamma'_n \beta(v, z, z_t)] \, dz + \int_{z_t}^{\infty} T'(z) \, \gamma(v, z, z_t) \, dz$$

$$+ \int_{z_t}^{\infty} \eta'(z) \, \delta(v, z, z_t) \, dz, \tag{3.28}$$

where

$$B_o(v, z_t) = \int_{z_t}^{\infty} 2\eta_o(z) \, f_o(z) \, D_o(v, z) \, W(z, z_t) \exp \{-\Gamma_o(v, z_t)\} \cosh [\tau_o(v, z, z_t)] \, dz, \tag{3.29}$$

and

$$\alpha(v, z, z_t) = 2\eta_o(z) \, f_o(z) \, D_o(v, z) \, W(z, z_t) \exp \{-\Gamma_o(v, z_t)\} \sinh [\tau_o(v, z, z_t)], \tag{3.30}$$

$$\beta(v, z, z_t) = 2\eta_o(z) \, f_o(z) \, D_o(v, z) \, W(z, z_t) \exp \{-\Gamma_o(v, z_t)\} \cosh [\tau_o(v, z, z_t)], \tag{3.31}$$

$$\gamma(v, z, z_t) = \beta(v, z, z_t) \left[\frac{1}{D_o(v, z)} \frac{\partial D_o}{\partial T} + \frac{1}{f_o(z)} \frac{\partial f_o}{\partial T} \right], \tag{3.32}$$

$$\delta(v, z, z_t) = \beta(v, z, z_t) \, / \, \eta_o(z). \tag{3.33}$$

Here, the derivatives of f(T) and D(v,T) with respect to temperature T can be easily obtained from Eqs. (3.11) and (3.13),

$$\frac{1}{f} \frac{\partial f}{\partial T} = \left\{ -\frac{1}{T} + \frac{1.439 \, E'}{T^2} \right\}, \tag{3.34}$$

$$\frac{1}{D} \frac{\partial D}{\partial T} = \frac{1}{2T} \left\{ \frac{2 \ln 2 \, (v - v_o)^2}{\alpha_D^2} - 1 \right\}. \tag{3.35}$$

Expressing the integration in Eq. (3.28) for a given tangent height measurement i in a form of matrix summation, one obtains

18

$$B_i(v) = B_{io}(v) + \sum_{k=1}^{m} \left(\frac{n_k'}{n_k} \right) X_k + \sum_{k=1}^{m} T_k' Y_k + \sum_{k=1}^{m} \left(\frac{\eta_k'}{\eta_k} \right) Z_{k'} \qquad (3.36)$$

where

$$B_{io} = \sum_{k=1}^{m} \beta_{k'} \qquad (3.37)$$

$$X_k = n_k \sigma_k D_k W_k \left[\sum_{j=k}^{m} \alpha_{ij} - \sum_{j=1}^{m} \beta_{ij} \right], \qquad (3.38)$$

$$Y_j = n_k \sigma_k D_k W_k \left[\sum_{j=k}^{m} \alpha_{ij} - \sum_{j=1}^{m} \beta_{ij} \right] \frac{1}{\sigma_k D_k} \frac{\partial(\sigma_k D_k)}{\partial T} + \gamma_{k'} \qquad (3.39)$$

$$Z_k = \beta_{ij'} \qquad (3.40)$$

and

$$\frac{1}{\sigma D} \frac{\partial(\sigma D)}{\partial T} = -\frac{1}{T} + \frac{1.439\, E''}{T^2} + \frac{1}{2T} \left[\frac{2 \ln 2 (v - v_o)^2}{\alpha_D^2} - 1 \right]. \qquad (3.41)$$

Note that $B_i'(v)$ is wavenumber dependent, and for an instrument with transmission function $I(v-v_o)$ and sensitivity S the perturbed signal in counts/sec at wavenumber v_o can be calculated as

$$\overline{B}_i(v_o) = \overline{B}_{io}(v_o) + \sum_{k=1}^{m} \left(\frac{n_k'}{n_k} \right) \overline{X}_k + \sum_{k=1}^{m} T_k' \overline{Y}_k + \sum_{k=1}^{m} \left(\frac{\eta_k'}{\eta_k} \right) \overline{Z}_{k'} \qquad (3.42)$$

where

$$\overline{B}_{io}(v) = \sum_{k=1}^{m} S \int_0^{\infty} \beta_k\, I(v - v_o)\, dv, \qquad (3.43)$$

and

$$\overline{X}_k(v_o) = S \int_0^{\infty} X_k\, I(v - v_o)\, dv, \qquad (3.44)$$

19

$$\overline{Y}_k(v_o) = S \int_0^\infty Y_k I(v - v_o) \, dv, \qquad (3.45)$$

$$\overline{Z}_k(v_o) = S \int_0^\infty Z_k I(v - v_o) \, dv. \qquad (3.46)$$

3.1.3.2 Data Analysis

Consider $\overline{B}_i(v_o)$ as the measured signal at wavenumber v_o and $\overline{B}_{io}(v_o)$ as the theoretically estimated signal based upon a guessed volume emission rate profile η_o, a temperature profile $T_o(z)$, and an O_2 number density profile $n_o(z)$. Equation (3.42), therefore, determines $\overline{B}_i(v_o)$-$\overline{B}_{io}(v_o)$, the deviation of the observed signal from the estimated signal based upon the three guessed profiles.

The X,Y, and Z in Eq. (3.42), in general, are referred to as the weighting functions. They represent the weightings of each parameters from various altitudes, in this case, the n'/n_o, T', and η'/η_o respectively, to the difference between the observed and the computed signals. If X is the largest among the three, the observed deviation is most sensitive to the guessed $n(z)$ profile, making the O_2 number density the best parameter to be recovered.

There are many techniques that may be used to recover $\eta(z)$, $T(z)$ and $n(z)$ from the measurements of $\overline{B}_i(v)$. One is the least-square fitting technique, in which iteration is performed to find the best $\eta(z)$,$T(z)$ and $n(z)$ profiles that give the minimum deviation $\overline{B}_i(n_o)$- $\overline{B}_{io}(n_o)$ summed over all spectral measurements. Since there are three sets of profiles needed to be recovered, multi-wavelength spectroscopic measurements (at least three spectral region) of the O_2 Atmospheric (0-0) band are required. The data analysis task involved in this technique is very inefficient and requires inversions of matrices in large dimensions. The large number of parameters involved in the fitting process not only makes the iteration convergence difficult, but also produces large errors in the recovered profiles.

Another alternative is to measure temperature and volume emission rate profiles simultaneously with the O_2 Atmospheric (0-0) band emission. This can be accomplished by carrying out

20

spectroscopic measurements of the (0-1) band emission. The volume emission rate of the O_2 Atmospheric (0-1) band is linearly related to that of the (0-0) band with a proportional constant determined by the Franck-Condon factor. Because the (0-1) band emission is optical thin, the measured line-of-sight brightness is a simple Abel integral and its volume emission rate profile can be retrieved efficiently (Hays et al., 1973). In addition, the temperature can also be obtained from the spectroscopic measurements of the rotational structure of the (0-1) emission band.

(0-1) Band: Temperature and Volume Emission Rate Measurements: If the (0-1) band emission is measured by a low resolution spectrometer whose instrument width is much wider than the doppler width of the emission line, the observed signal at wavenumber v_o is

$$\overline{B}(v_o, z_t) = \sum_{j=1} S \int_{z_t}^{\infty} \eta(z) \, f_j(z) \, W(z, z_t) \, I(v_j - v_o) \, dz, \tag{3.47}$$

where v_j is the wavenumber of the rotational line j, and $I(v_j-v_o)$ and S are the instrument transmission function and the sensitivity, respectively.

Figure 7 shows the computed signals of the O_2 (0-1) band emission using a 12-channel Image Plane Detector Spectrophotometer (IPDS) (Luo et al., 1988) for two tangent height measurements: 60 and 80 km. A volume emission rate profile derived from the one for the (0-0) band (Bucholtz et al., 1986) and a continuum scattering background which decreases exponentially with altitude have been assumed. The instrument parameters of the IPD Spectrophotometer listed in Table 1 and a field-of-view corresponding to an image of 2km in the vertical and 300 km in the horizontal directions of the Earth's limb are used in the simulation.

Table 1

IPD Spectrophotometer Instrument Parameters
Used in O_2 Resonance Fluorescence Simulation

|		
A_0	:	45.603 cm^2 (3 inch diameter)
W	:	1.5 x 10^{-4} ster (~ 2.0 km x 300 km at the limb)
Tr	:	0.3
Qe	:	4% at 7620 Å, and 2% at 8650 Å
I.P.	:	1 second

Figure 7

22
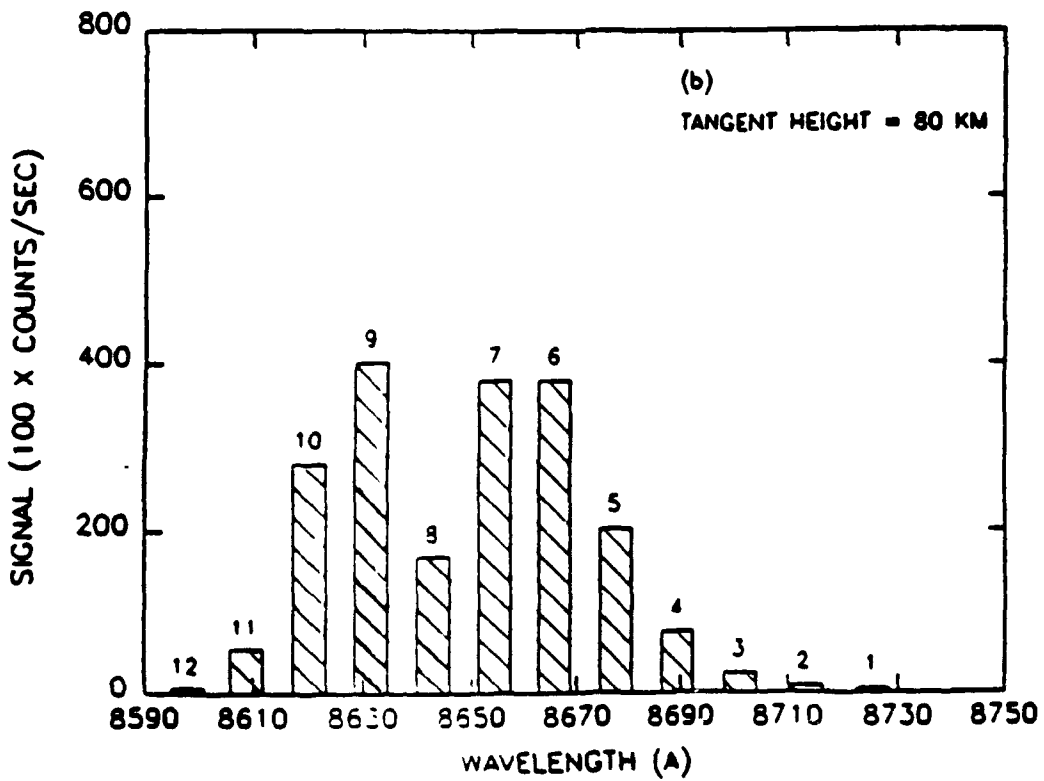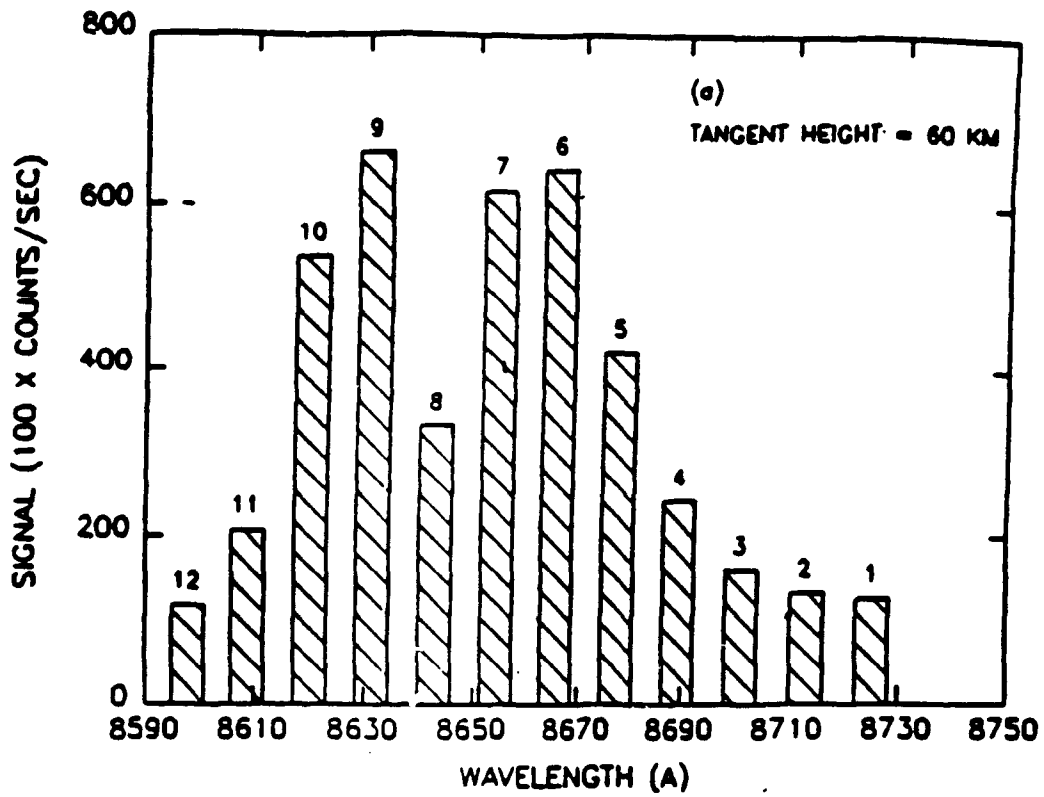
The volume emission rate at wavenumber v_0 and altitude z, $\eta(v_0,z)$, defined as

$$\bar{\eta}(v_{o}, z) = S \sum_{j=1} \eta(z) \, f_j(z) \, I(v_j - v_o),$$

(3.48)

can then be obtained by using the Abel inversion algorithm (Hays et al., 1973). After measurements at all the wavenumbers have been inverted, we can get the spectral information or the rotational band structure of the (0-1) band emission rate.

Figure 8 gives the volume emission rates recovered at the 12 spectral regions of the IPDS at 60 and 80 km altitudes, revealing clearly the rotational emission band structures. By using a nonlinear least-square fitting method (Killeen and Hays, 1984; Luo et al. 1988), one can then obtain the total band volume emission rate and the rotational temperature of the $O_2(b^1\Sigma_g^+)$ molecules. In order to conserve computation, we first linearize the problem by expanding Eq. (3.48) about a set of approximations or initial guesses (η, T, η_c) and keep only the first-order terms in the expansions:

$$\bar{\eta}_{kn}(\eta_k, T_k, \eta_{ck}) \cong \bar{\eta}_{kn}(\eta'_{ko}, T'_{ko}, \eta'_{ck}) + \frac{\partial \bar{\eta}_{kn}}{\partial \eta_k}(\eta_k - \eta'_{ko}) + \frac{\partial \bar{\eta}_{kn}}{\partial T_k}(T_k - T'_{ko}) + \frac{\partial \bar{\eta}_{kn}}{\partial \eta_{ck}}(\eta_{ck} - \eta'_{ck})$$

(3.49)

where η_k is the (0-1) band volume emission rate, and η_{ck} is the continuum scattering rate at altitude k and wavenumber channel n, respectively.

If the measured volume emission rate at the n-th channel obtained from Eq. (3.49) is expressed by C_{kn}, the sum of the square of the residuals between the theoretically computed signal and the measured signal C_{kn} is calculated by

$$<\delta_k^2> = \sum_{n=1}^{12} (C_{kn} - \bar{\eta}_{kn})^2$$

(3.50)

By minimizing $<\delta_k^2>$, one can obtain a set of better estimated η_k, T_k and η_{ck}, or P_k^l (l=1,2,3 for η, T, η_c, respectively), a general representation of the newly determined parameters from a single matrix multiplication operation:

$$P_k^l = \sum_{m=1}^{3} M_{km}^l \, N_{km},$$

(3.51)

where M_{kc}^l is an inverse matrix of L_{km}^l,

Figure 8

24

$$L^1_{km} = \sum_{n=1}^{12} \frac{\partial \overline{\eta}_{kn}}{\partial P^1_k} \frac{\partial \overline{\eta}_{kn}}{\partial P^m_k}, \tag{3.52}$$

and
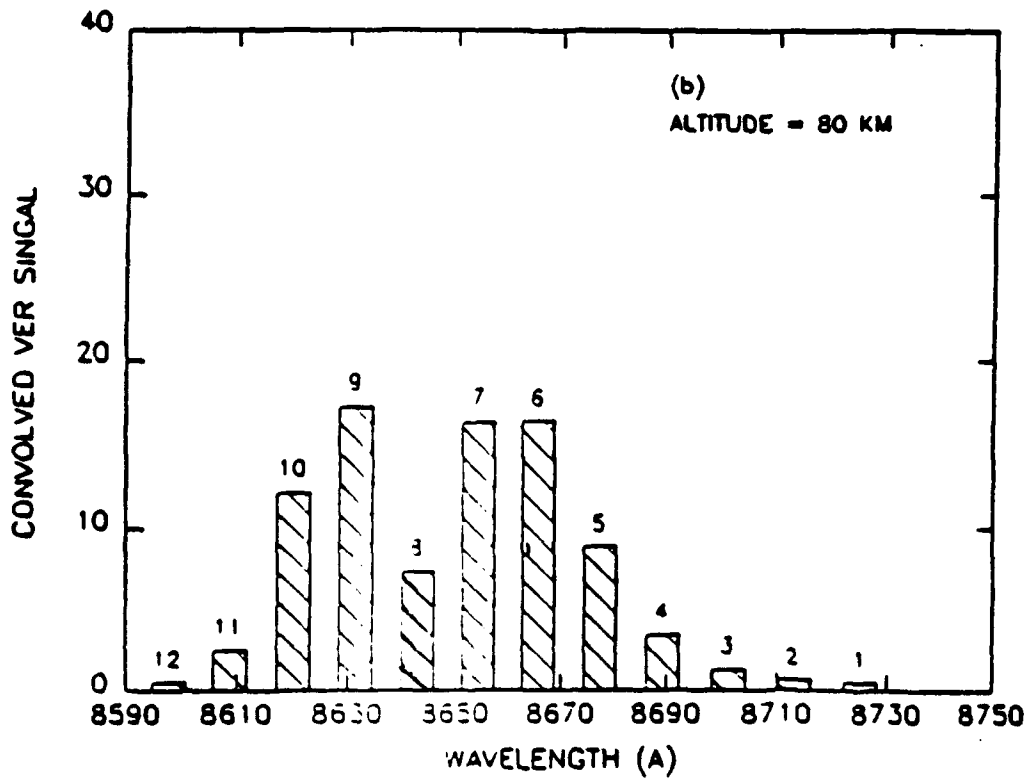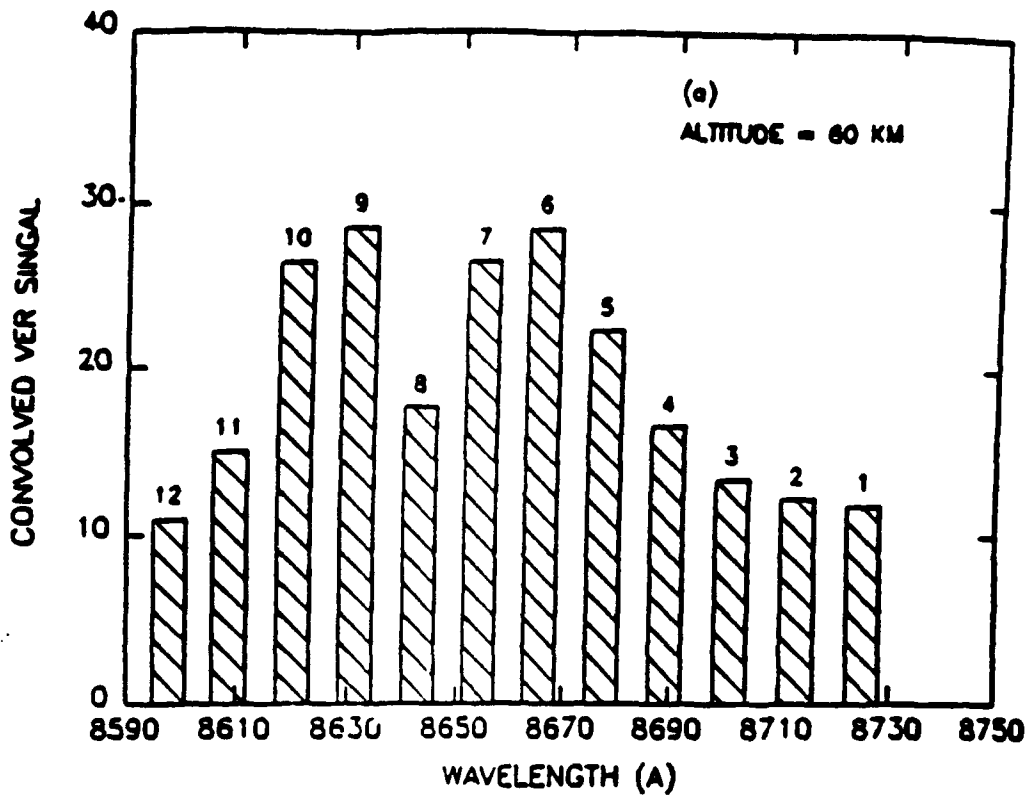
$$N_{km} = \sum_{n=1}^{12} \left(\overline{\eta}_{kn} - C_{kn} - \sum_{l=1}^{3} \frac{\partial \overline{\eta}_{kn}}{\partial P^1_k} P'^1_k \right) \frac{\partial \overline{\eta}_{kn}}{\partial P^1_k}. \tag{3.53}$$

Iterations are performed in order to obtain convergence of the results. The speed of convergence depends upon the proximity of the initial guessed values to the actual values.

(0-0) Atmospheric Band: Density Measurement: After the (0-1) band volume emission rate and the atmospheric temperature profiles are determined, we can calculate from Eq. (3.42), $\overline{B}_i(v_o)$-$\overline{B}_{io}(v_o)$, the deviation of the observed signal at tangent height i and wavenumber v_o for the (0-0) band emission from the estimated signal based upon a guessed O_2 number density profile $n_o(z)$,

$$\overline{B}'_i(v_o) = \overline{B}_i(v_o) - \overline{B}_{io}(v_o) = \sum_{k=1}^{m} \left(\frac{n'_k}{n_k} \right) \overline{X}_{ik}. \tag{3.54}$$

We can solve the above linear equation for n'(z) to get a better estimate of n(z), n(z) = $n_o(z)$ + n'(z) by minimizing the square of the deviation of $\overline{B}_i(v_o)$- $\overline{B}_{io}(v_o)$ summing over all spectral and tangent heights. The n(z) profile is then used as a new guess to Eq. (3.54), and the process is repeated until n'(z) becomes very small compared to $n_o(z)$. This technique is identical to the one used for the (0-1) band data analysis and gives one best O_2 number density profile based upon the measurements at all of the tangent heights and the spectral regions.

Because the O_2 number density information can only be recovered if there is significant degree of extinction in the measured intensity of the O_2 Atmospheric (0-0) band emission, the capability of this technique is therefore limited by the magnitude of the absorption cross-section. In other words, the O_2 number density profile can only be directly measured up to an altitude of approximately 90 km. Since the temperature profile is obtained in the whole region between 60 and 120 km, the O_2 density from 90 km to 100 km at the turbopause can be derived from the barostatic equation (Banks and Kockarts, 1973),

$$n(z) = n_o(z) \left[\frac{T(z_o)}{T(z)} \right] \exp \left\{ - \int_{z_o}^{z} \frac{mg}{kT} dz \right\} \tag{3.55}$$

25

Figure 9

26
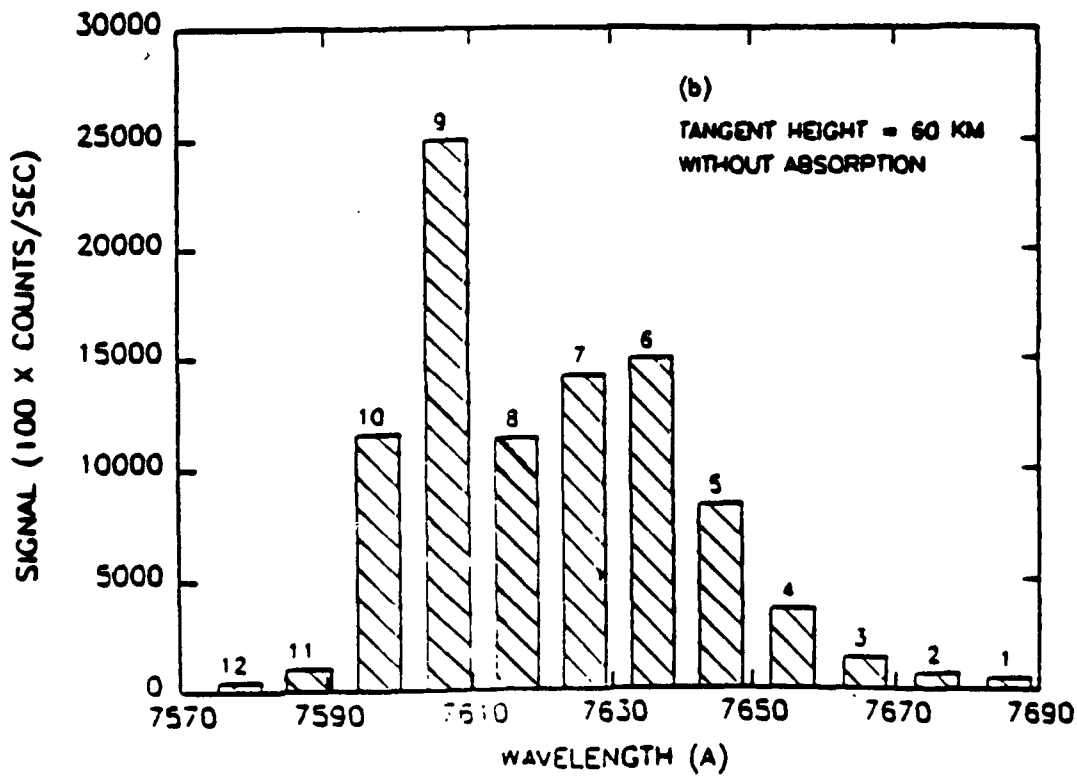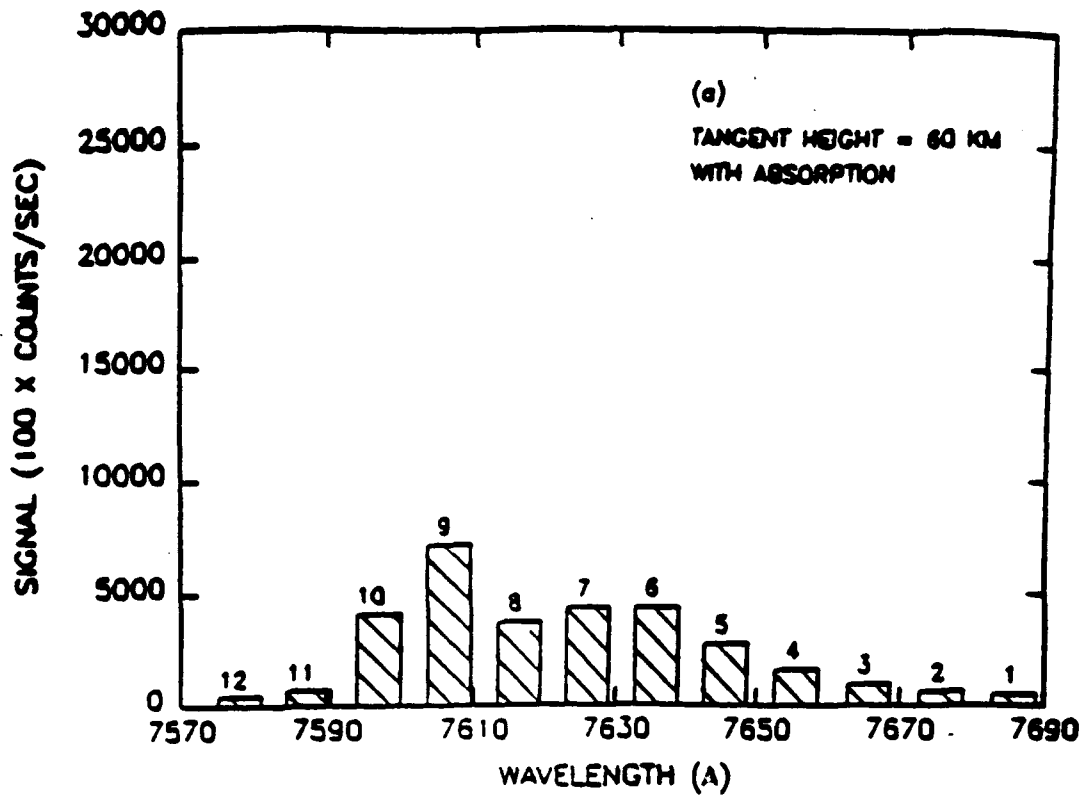
under perfect mixing condition, and above 100 km,

$$n(z) = n_o(z) \left[\frac{T(z_o)}{T(z)} \right] \exp \left\{ -\int_{z_o}^{z} \frac{m_{O2} g}{kT} \, dz \right\}$$

(3.56)

under diffusive equilibrium condition, where m and m_{O2} are the mean molecular weights of the atmosphere and O_2, respectively.

Figure 9 shows the simulated signals that the IPDS measures for a one second integration time at a tangent height of 60 km. The unattenuated signals, derived from the (0-1) volume emission rate profile, are also shown. Although it is not a practical approach, we can still, in principle, recover the $n(z)$ profile directly from Eq. (3.54) using measurements from a single channel. However, because the optical depth differs for each channel, the accuracy in the recovered density profile is different.

3.1.3.3   Statistical Accuracy Analysis

As indicated in Fig. 9, the difference in the observed and computed signal, $\bar{B}_i - \bar{B}_{io}$, depends upon not only the O_2 number density profile n/n_o, but also the temperature T and the volume emission rate profiles η'/η_o. The uncertainties in the temperature and the volume emission rate determined from the (0-1) band emission would give rise to error in the recovered O_2 number density.

Statistical Errors in Temperature and Volume Emission Rate: The statistical errors ΔP_k^l in the temperature (P_k^2) and volume emission rate (P_k^1) obtained from the (0-1) band measurements can be estimated from Eq. (3.51) using theory of error propagation,

$$(\Delta P_k^l)^2 = \sum_{n=1}^{12} \left\{ \sum_{m=1}^{3} M_{km}^l \left(\frac{\partial \bar{\eta}_{km}}{\partial P_k^n} \right)^2 \right\} (\Delta C_{kn})^2.$$

(3.57)

where $\Delta C_{kn} = C_{kn}^{1/2}$, assuming that measured signal C_{kn} has a Poisson random noise. Figure 10 presents the statistical accuracies in the temperature and total (0-1) band volume emission rate profiles obtained based upon the simulated measurements given in Fig. 8.
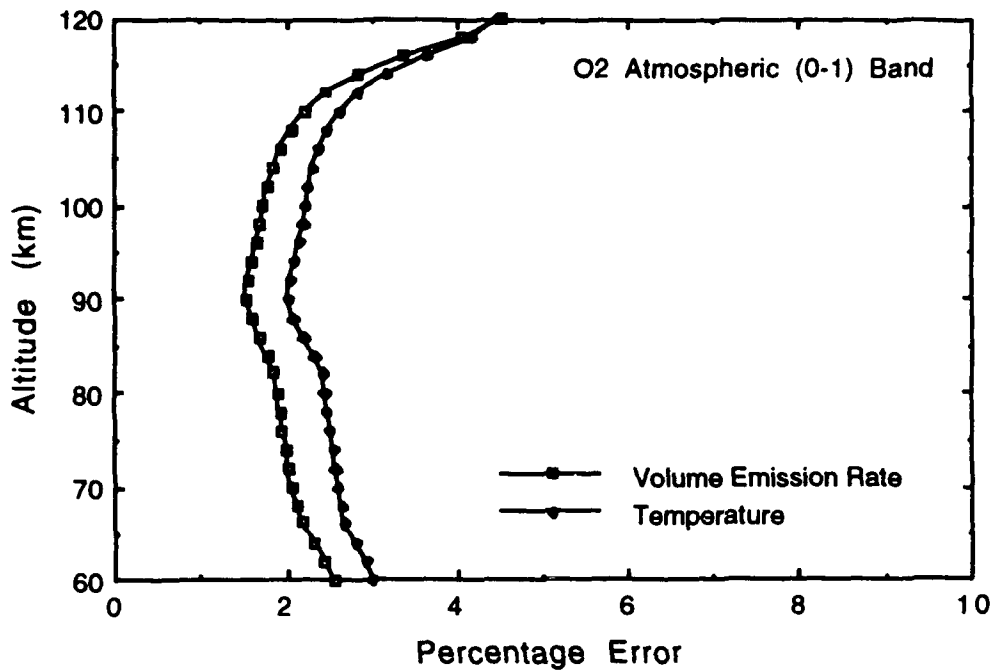
Figure 10

Statistical Errors in O_2 Number Density: The capability of recovering O_2 number density profile from the (0-0) band emission depends upon the relative magnitude of its weighting function (X) in Eq. (3.42) compared to the ones of temperature (y) and the volume emission rate (z). For example, consider a case when the weighting function for the volume emission rate η'/η_0 is the largest among the three. A small error in the profile of $\eta(z)$ would produce a large error in the computed signal $\bar{B}_{io}$, which in turn is propagated to the recovered O_2 number density profile.

Figure 11 shows the weighting functions X, Y, and Z as a function of altitude for measurements at 60 km tangent height for both a weak (channel 3) and a strong (channel 9) absorption case, respectively. The maximum weighting functions, especially for the weak absorption case, are found at the tangent altitude, resulting directly from the geometric enhancement effect. For the stronger absorption case, most of the emission originating from the lower altitude region is absorbed and cannot be observed. As a result, the weighting functions near the tangent altitude are reduced and the altitude at which the O_2 number density can be recovered becomes higher.

Figure 11

29
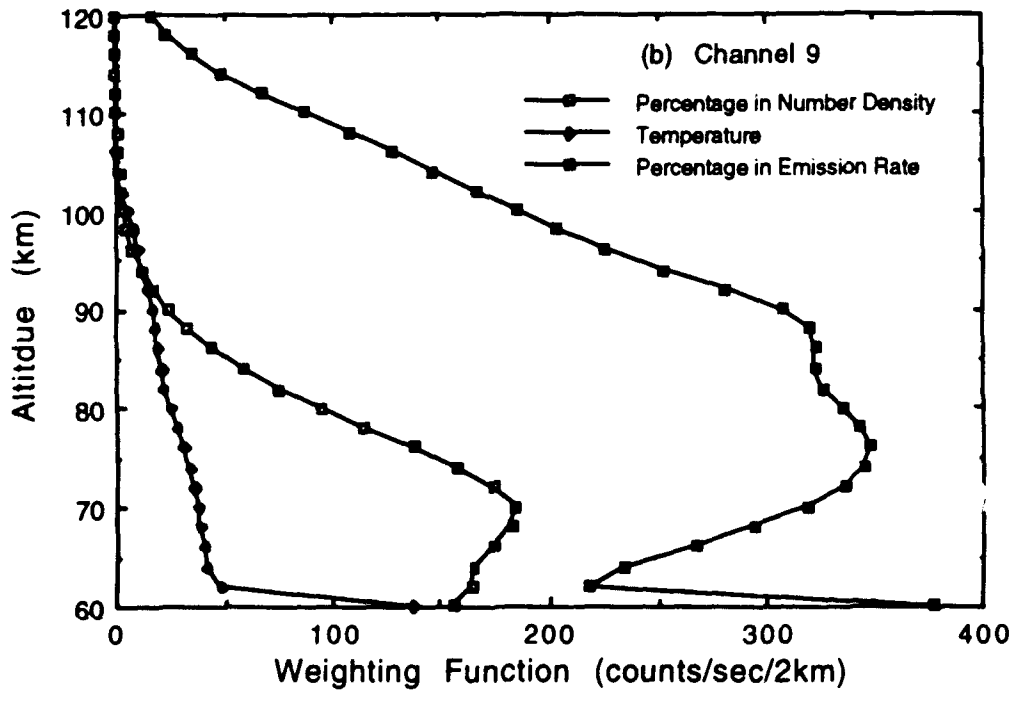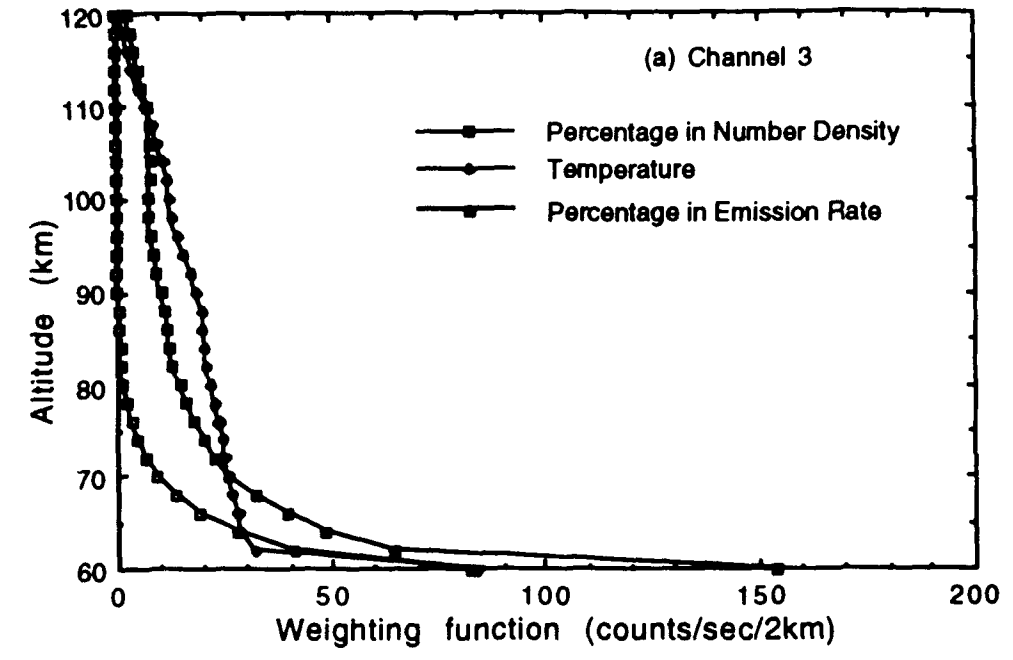
Expressing n'/n_0 in terms of B', T', and η'/η_0,

$$\frac{n_k'}{n_k} = \sum_{i=1}^{m} \overline{X}_k^{-1} \overline{B}_i - \sum_{k=1}^{m} \left(\sum_{i=1}^{m} \overline{X}_k^{-1} \overline{Y}_k\right) T_k' - \sum_{k-1}^{m} \left(\sum_{k=1}^{m} \overline{X}_k^{-1} \overline{Z}_k\right) \left(\frac{\eta_k'}{\eta_k}\right), \qquad (3.58)$$

we can estimate the error in the recovered n'/n_0 using theory of error propagation,

$$\Delta \left(\frac{n_k'}{n_k}\right)^2 = \sum_{i=1}^{m} (\overline{X}_k^{-1})^2 (\Delta B_i)^2 + \sum_{k=1}^{m} \left(\sum_{i=1}^{m} \overline{X}_k^{-1} \overline{Y}_k\right)^2 (\Delta T_k')^2 + \sum_{k=1}^{m} \left(\sum_{i=1}^{m} \overline{X}_k^{-1} \overline{Z}_k\right)^2 \Delta \left(\frac{\eta_k}{\eta_k}\right)^2 \qquad (3.59)$$

where ΔB_i is the error in the measured signal, $\Delta(n_k'/n_k)$ and $\Delta(\eta_k'/\eta_k)$ are the relative error in the O_2 number density and the (0-0) band volume emission rate, and $\Delta T_k'$ is the error in the temperature, respectively.

Figure 12 shows the accuracies of the retrieved O_2 number density profile based on the (0-0) band 12-channel IPDS intensity signals shown in Fig. 9(a). The accuracies of the temperature and volume emission rate profiles recovered from the (0-1) band measurements have been included. The measured signals at channel 12 ($\sim 7570\text{Å}$) have been used as the contribution of the scattering continuum background. Among the other eleven spectral regions measured, four are able to provide the O_2 number density profile with an accuracy less than 10% below 90 km. Because both the emission signals and the self-absorption cross-sections are small in the spectral regions near the bandhead (channel 11) and the bandtail (channel 1), the accuracies in the recovered O_2 number density are very poor. As the altitude increases above 90 km, the self-absorption process becomes less important, resulting in a rapid deterioration in the quality of the recovered O_2 number density profile.

Figure 13 presents the accuracy of the recovered O_2 number density profile when the measurements from all the eleven channels are combined. It demonstrates that using a spectrometer, such as the IPDS used here, one can retrieve a O_2 number density profile below 90 km with an accuracy of less than 5% for one second integration time at each tangent height. If we use the barostatic equation to constrain the density profile to follow the temperature profile, the accuracy is improved, especially in the region above 90 km where the accuracy from the direct measurements is poor.
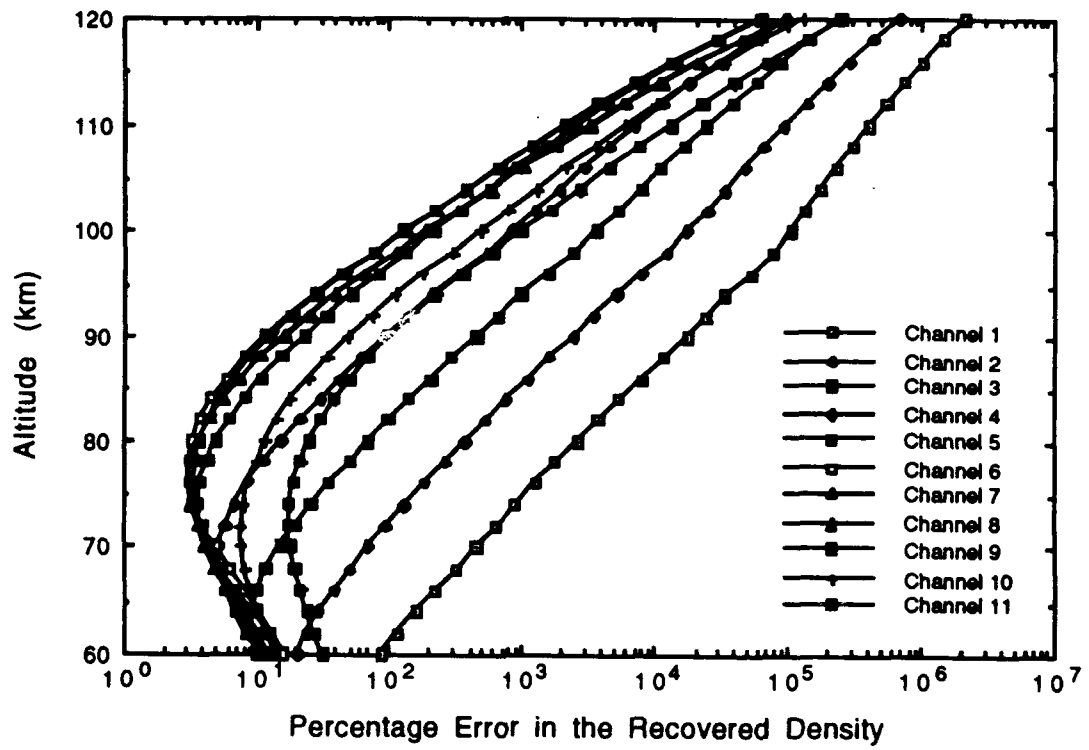
Figure 12
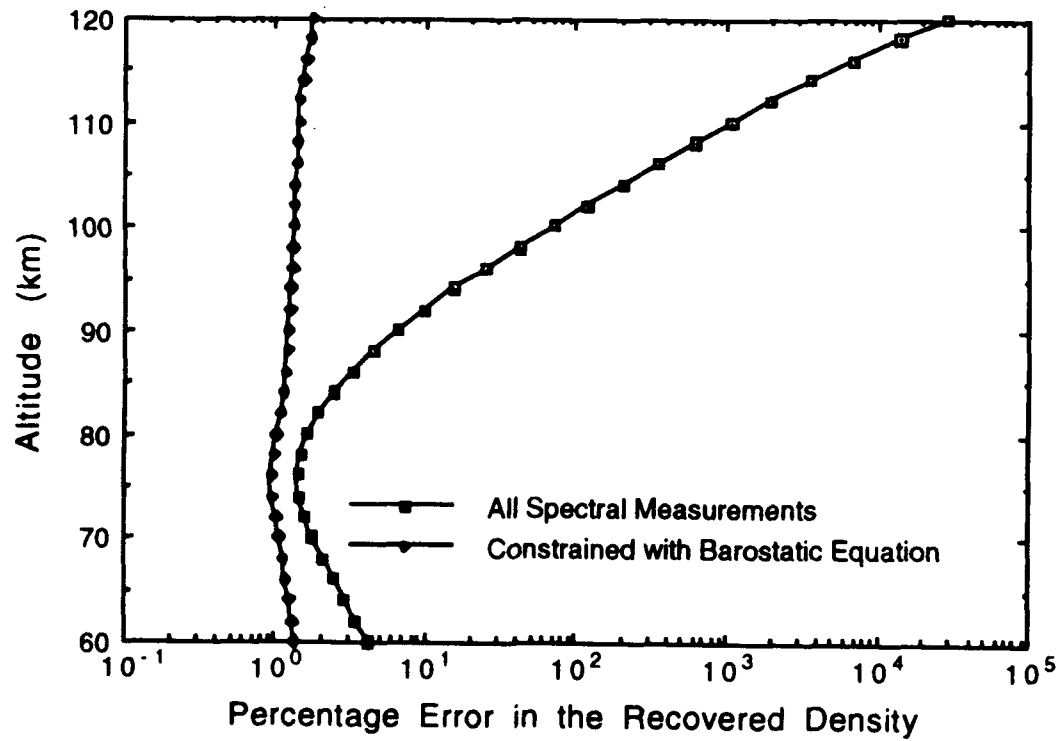
Figure 13

3.2 A Rocket Experiment

The conceptual design of an instrument for the remote measurement of upper atmospheric density includes three basic components, i.e., a scanning telescope, a light dispersion unit, and a detector. Two instrument types have been examined during the trade-off study phase (see previous report Hays et al., 1988): the Image Plane Detector (IPD) Spectrophotometer and the grating spectrometer (GS). The grating spectrometer was selected as the prototype instrument developed for the MAP rocket experiment because it is compact and its rectangular field-of-view matches with the limb of the atmosphere.

In this section we will give a detailed description of the prototype spectrometer used in the rocket experiment and spectral observations of both the O_2 (0-0) and (0-1) Atmospheric bands in the dayglow. In addition, we will present the recovered density and temperature profiles with evaluations of all the possible sources of error, both statistical and systematic.

3.2.1 Instrument: Density and Temperature Spectrometer (DATES-1)

The optical characteristics of the DATES instrument are determined by the desire to view the Earth limb with 2 km vertical resolution and to perform the measurements in a reasonable time period (long enough to achieve desired measurement accuracy and short enough to avoid spatial smearing). These desires are achieved within the constraints imposed by the need to baffle the instrument against a brighter signals coming from lower tangent heights. The basic component of DATES-1, as illustrated in Fig. 14, consists of a baffled telescope, a 1/4 meter Ebert-Fastie spectrometer, and a Charge-Couple-Device (CCD) detector system. Here we will describe the instrument by first discussing the general background of the spectrometer and then briefly the individual instrument components themselves.

The Charge-Couple-Device (CCD) is becoming popular as a detector because of its high quantum efficiency, linear response, and large dynamic range. The sensitivity of a CCD is more than one order of magnitude greater than that of the Image Plane Detector (IPD) used in the Dynamic Explorer Satellite. For example, at 7600 Å where the Atmospheric (0-0) band is measured the detector quantum efficiency for CCD varies from 25% for a front illuminated device to more than 60% for a back-thinned and AR coated detector (Janesick et al., 1987). In contrast, the quantum efficiency for IPD and conventional red-sensitive photomultiplier is only a few percent at its best. For the Thompson TH7882 CCD chip which is used in DATES-1, the quantum efficiency is ~30%, which is almost a factor of 10 increase in sensitivity.

The other advantage of a CCD is its capability of being electronically blocked on chip so that the spectral resolution can be easily adjusted. This has the advantage that in situations where there is a large signal, the detector noise is not significant, we can have higher spectral resolution and study the spectrum in detail. On the other hand, when the signal is low and the noise is significant, the

CCD can be programmed so that a low resolution spectrum is produced.

3.2.1.1 Instrument Description

Optics: DATES-1 has a field of view of 0.0717 x 2.52 degrees defined by an objective lens with focal length of 150 mm and an input slit of 0.1877 x 6.62 mm. The optical design was fully raytraced and carefully optimized to minimize the off-axis blurring due to optical aberration.

Telescope and Baffle: DATES-1 observes the atmosphere on its limb through a two-stage baffled f-5 telescope. The telescope provides the light collection and pointing, and directly feeds the light collected to the spectrometer. The baffle is similar in design to the ones used in the Visible Airglow Experiment (VAE) photometers on the Atmosphere Explorer Satellites and the Fabry-Perot Interferometer (FPI) on the Dynamic Explorer Satellite. The purpose of the baffle system is to eliminate stray light which enters the optics from the bright limb of the Earth from lower tangent height. Internal baffles are also installed within the spectrometer to further minimize the scattering light.

Ebert-Fastie Spectrometer: DATES-1 uses a 1/4 meter Ebert mirror and a 1200 lines/mm holographic grating. It operates on the first interference order for the measurements of (0-0) 7620Å and (0-1) 8600Å spectral regions. A blocking filter which eliminates the photons with wavelength shorter than 6000Å is installed to prevent the photons of higher order dispersion from reaching the detector. The spectrometer is preset at two grating angles controlled by a solenoid switch so that two spectral regions can be measured alternatively. Spectral coverages of ~234Å and ~222Å are observed in the (0-0) and (0-1) spectral regions, respectively.
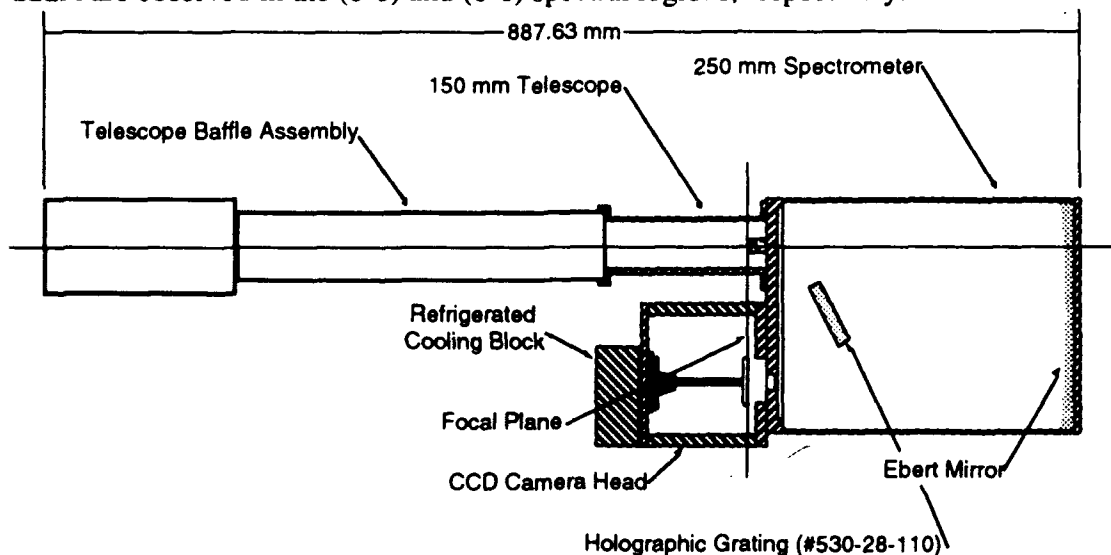
University of Michigan NIRS Spectrometer System

Figure 14

CCD DARK COUNT CALIBRATION
(MAY 15, 1989)
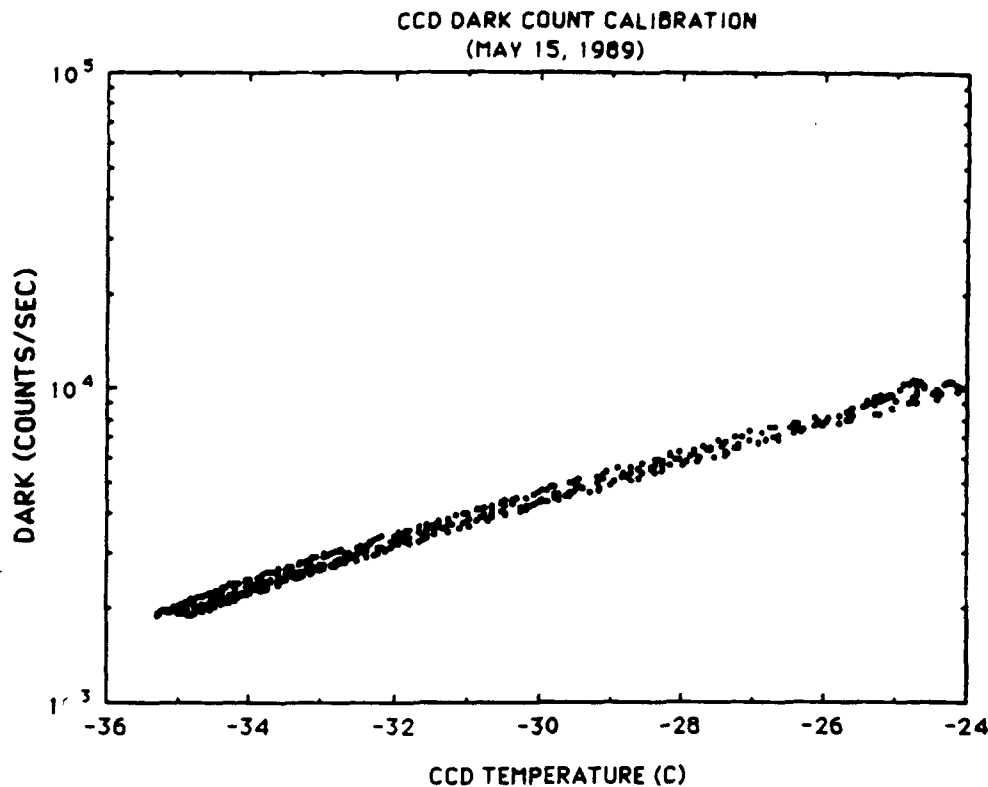


Figure 15

CCD Detector: The grating-dispersed spectrum is imaged onto a frame transfer linear CCD detector and detection of the spectra is accomplished by using a CCD with on-chip binning to determine the spectrum of interest. A CCD detector is a MOS (metal-oxide-semiconductor) optical detector that is composed of up to several million independent sites (pixels) where photon-induced charge is stored. The amount of charge induced is proportional to the light intensity and it can accumulate over an extended period of time with its exposure length (integration time) controlled by the frequency of the transfer between the storage frame and image frame. The DATES-1 CCD detector system is a modified Photometric CCD camera head with a Thompson TH7882 frame transfer CCD chip installed within it.

The CCD chip is cooled using a three-stage thermal-electric cooler with flowing liquid coolant in order to decrease the thermal noise. Figure 15 shows the DATES-1 CCD dark noise (1 digital count = 15.6 electrons) per pixel as a function of CCD temperature. The coolant temperature is maintained by a pump, a pre-frozen ice bucket, and a thermal radiator. During operation of the rocket flight, the sink temperature was maintained at 0 degree C, giving the CCD temperature of approximately -36.5 degree C. The dark current at this temperature was measured to be ~14 electrons per pixel per second.

DATES-1 Control Electronics: Figure 16 shows the overall control diagram of the DATES-1 operation. The DATES-1 electronic package consists of three main sections: CCD electronic card stack, control computer stack, and power supply modules. All phases of instrument operation are under the direct control and supervision of the DATES-1 control computer.

34
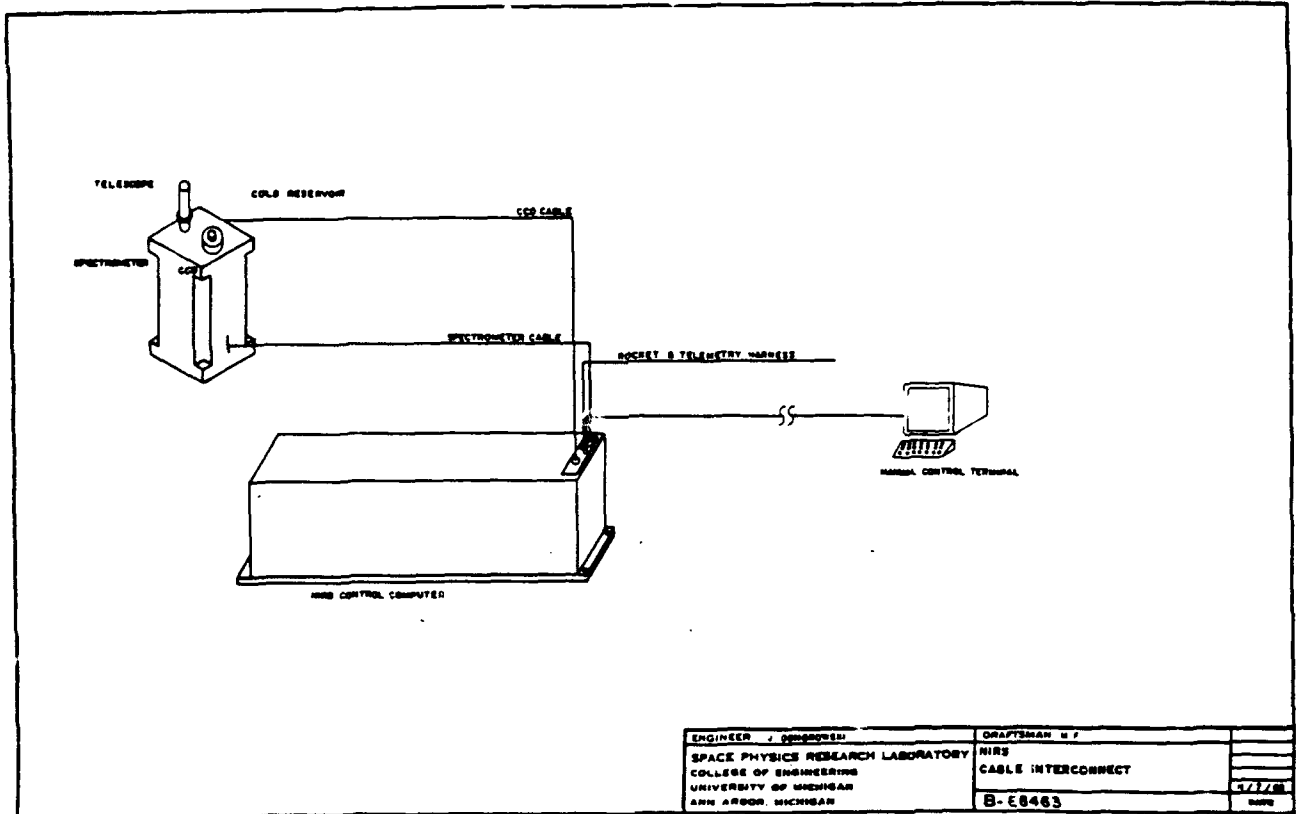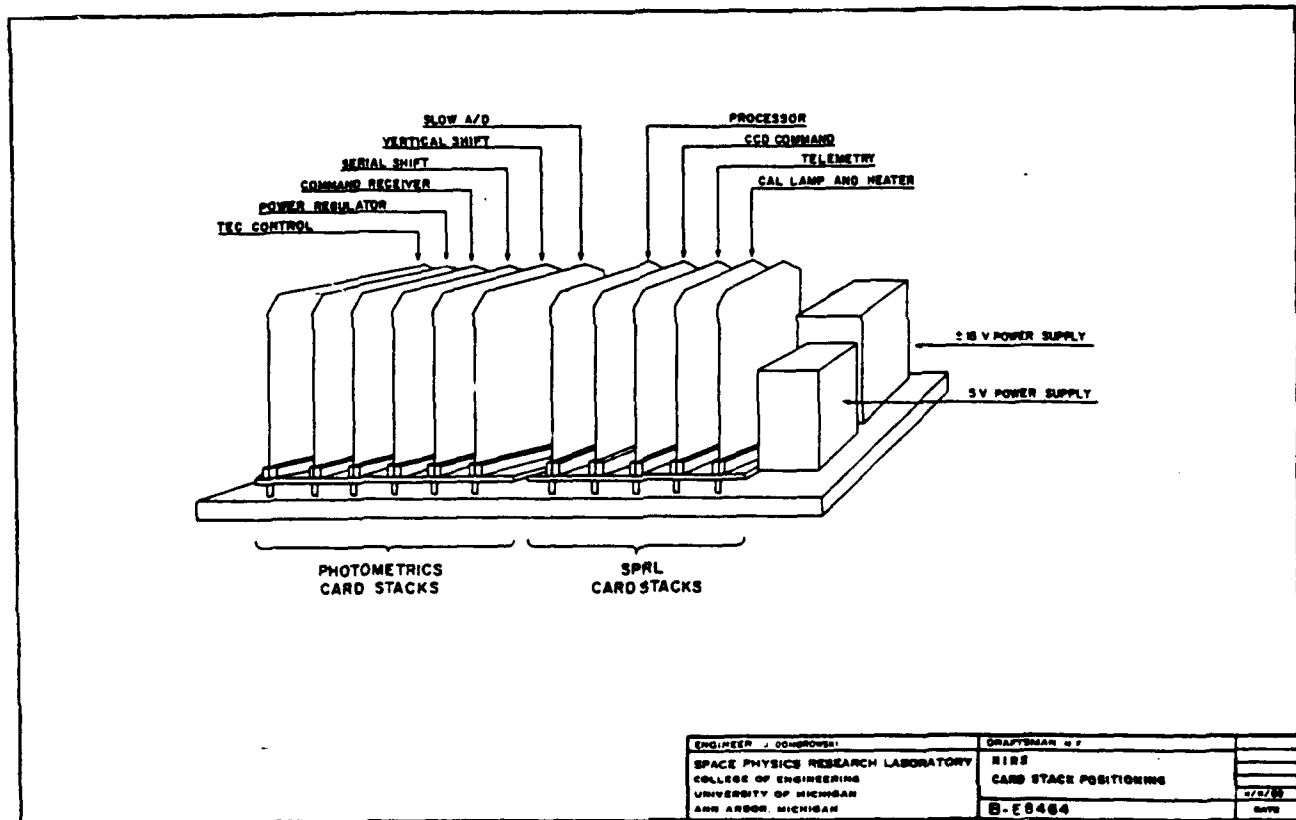
Figure 16

Figure 17

As shown in Figure 17, the CCD card stack contains all the electronics required to control the vertical and horizontal shifting (binning) of the CCD pixel registers, power control of the CCD thermal electric cooler and regulating heater, a low noise double correlation A/D conversion of the CCD data (~15.6 electrons per digital count), and a command receiver which puts all functions under the control of an external controller.

The DATES-1 control computer stack consists of a processor board based upon an Intel 16 bit 8096 microcontroller, a command board that sends commands to the CCD card stack, a telemetry board which interfaces with the rocket telemetry system, and a calibration lamp and thermal electric cooler (TEC) controller for closed loop control of the TEC.

The power supply modules consist of two Dale DC-DC converters that provide the +5 V and the +/- 15 V required by the system.

Telemetry Board: The DATES-1 onboard control computer used a free floating telemetry format that was not tied in any way to the rocket major frame rate, telemetry clock, or in any other way synchronized to the rocket. Whenever there was data contained in the computer output buffer and a telemetry enable command was triggered, the data residing in the buffer would be read from the buffer and encoded.

The computer uses full nine bit telemetry (bits 0-8). The ninth data bit (bit 8) is used to determine the difference between valid data (contained in bits 0-7) and "filler", i.e. when there is nothing being read from the telemetry buffer, the ninth bit (and all other bits) are set to zero.

3.2.1.2   Instrument Characteristics

Spectral Calibration: Figures 18(a) and (b) show the spectral calibration of the two spectral regions using a monochrometer. A linear relationship was obtained as expected between spectral wavelength and the pixel number (between 1 and 384), with slopes of 0.60974 Å and 0.57894 Å per pixel for (0-0) and (0-1) bands, respectively, giving rise to total spectral coverages of 234.14 Å and 222.3 Å.

The more accurate spectral wavelength determination was obtained using spectral lamps of argon (for 7600 Å spectral region) and neon (for 8600 Å spectral region). The results are shown in Figs. 19(a) and 19(b), respectively. The correct expressions which relate pixel number to wavelength are then determined to be:

$$\lambda = 7772.5 - 0.60974 \times N \qquad \text{(for 7600Å spectral region)}$$
$$= 8778.75 - 0.57894 \times N \qquad \text{(for 8600Å spectral region)}$$

where N is the pixel number of the detector.

SPECTROMETER WAVELENGTH CALIBRATION
(MAY 16, 1989)

$y = 7769.5 - 0.60974x \quad R^2 = 1.000$

$y = 8769.4 - 0.59319x \quad R^2 = 0.999$

Figure 18

37
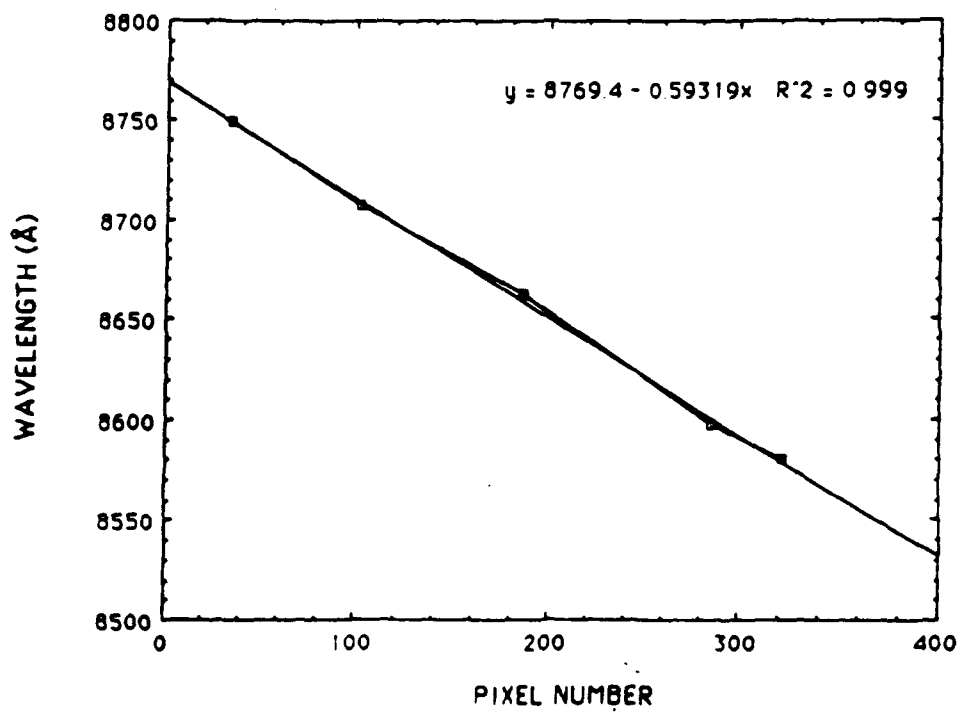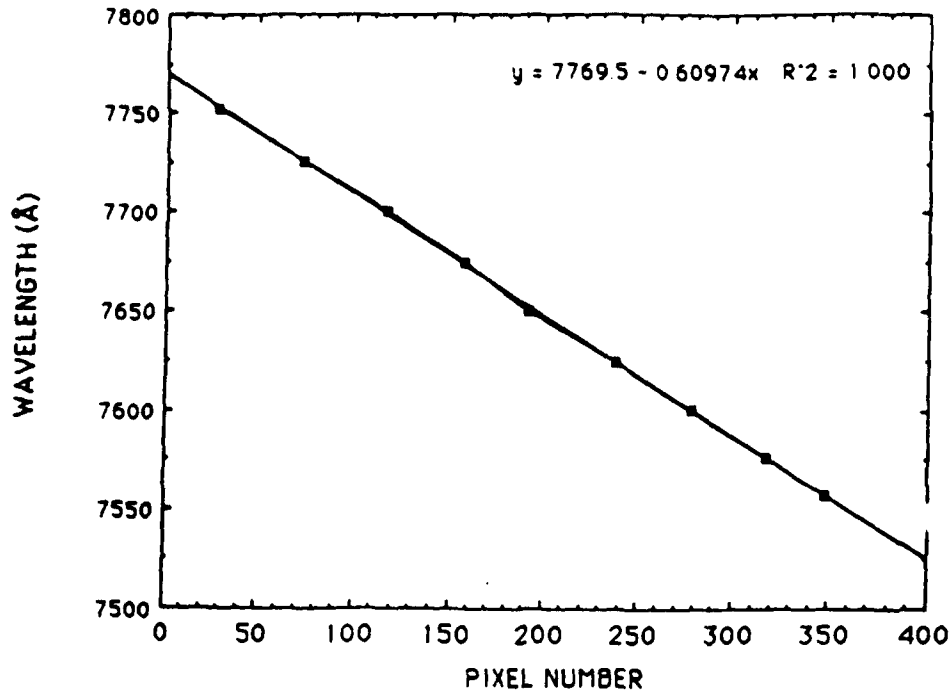
NIRS SPECTRAL CALIBRATION (ARGON)
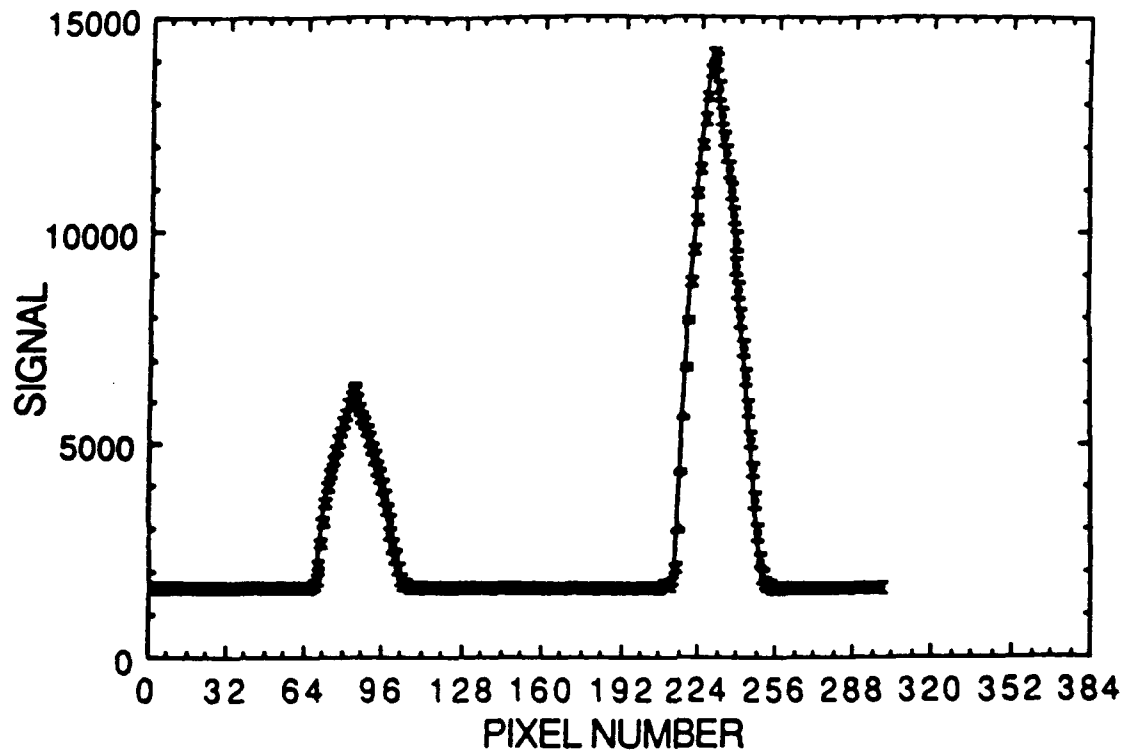

NIRS SPECTRAL CALIBRATION (NEON LAMP)
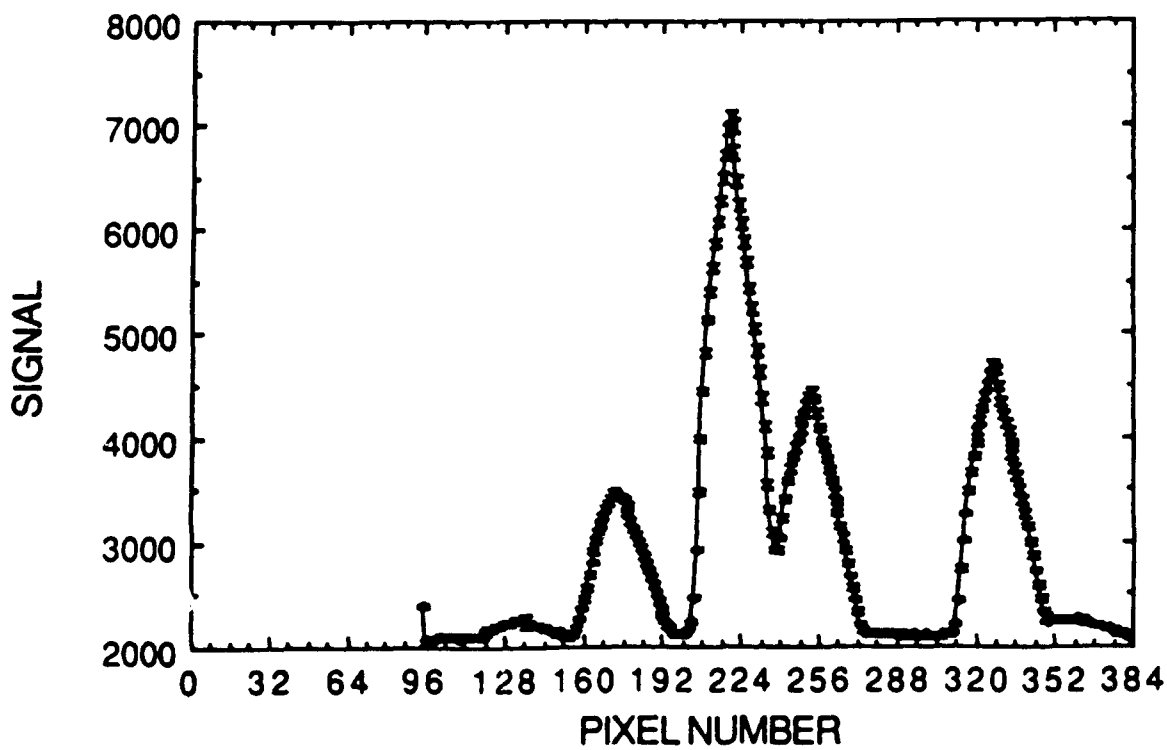
Figure 19

Instrument Function: Figure 20(a) gives the instrument functions obtained from two argon lines in the (0-0) 7600 Å spectral region with their peak transmissions normalized to 1.0. Although the two spectral lines are separated by approximately 100 Å [as seen in Figure 19(a)], the instrument functions are almost identical. The full width at half maximum (FWHM) is found to be 22 pixels or an instrument resolution of ~13.4 Å. Figure 20(b) gives the instrument transmission function near the (0-1) 8600 Å spectral region and a similar instrument resolution to the one at 7600 Å is obtained. Since the CCD chip was located inside the Photometric camera head, we were not able to accurately position it at the focal point of the Ebert mirror. As a result, being slightly out of focus, we obtain the triangle-shaped instrument function instead of the rectangular-shaped instrument function expected for a perfect instrument with no aberration. In fact, after we recovered the DATES-1 from the rocket payload, we were able to obtain an instrument function close to the theoretical one by simply slightly adjusting the position of the CCD detector along the optical axis.

Sensitivity: The DATES-1 absolute sensitivity is obtained by using an NBS (National Bureau of Standards) lamp of known spectral shape and brightness. Figures 21(a) and (b) give the results of our calibration. Approximately 1.2 Counts/sec/R/Å is obtained in the spectral region near 7600 Å, while ~0.8 Count/sec/R/Å is obtained in the spectral region near 8600 Å. An apparent variation of instrument sensitivity with wavelength is found most likely due to the variation of the detector quantum efficiency and the grating efficiency. It should be noted that the CCD detector output is binned every 12 by 288 pixels so that 32 spectral channels (388 divided by 12) are measured. This binning pattern gives intensity measurements every 7.3 Å and 6.95 Å for measurements in the (0-0) and (0-1) bands spectral regions, respectively. The absolute sensitivity may vary if the binning pattern is different.

Sources of Measurement Uncertainty: The accuracy of any measurement is governed by the accuracy of the instrument calibration and the counting statistics. In addition to the photon statistics (which usually follows the Poisson distribution), there exist many sources of error concerning the output CCD digital counts. The DATES-1 TH7882 CCD chip, in general, is well-behaved, and the preamplifier output has a very low noise (less than ten electrons at 30 kHz). However, a threshold still exists for the transfer of charge when the readout electrons drop below 50 electrons. The use of a very small bias charge eliminates this problem and allows operation down to very low charge levels. The use of a bias charge increases the background noise by a small amount. The combined preamplifier noise and the bias noise for the DATES-1 CCD detector system are found to be ~30 electrons or 2 counts per read. This is negligibly small compared to the dark current, which runs at appproximately 775 counts (~12,096 electrons) per 0.25 second after the pixel binning (12 by 288 pixels) at -36.5° C. In other words, under DATES-1 operating temperature, the dark current is supplying sufficient bias charge necessary to overcome the charge transfer problem.

NIRS (0-0) band Instrument Function

NIRS (0-1) band Instrument Function
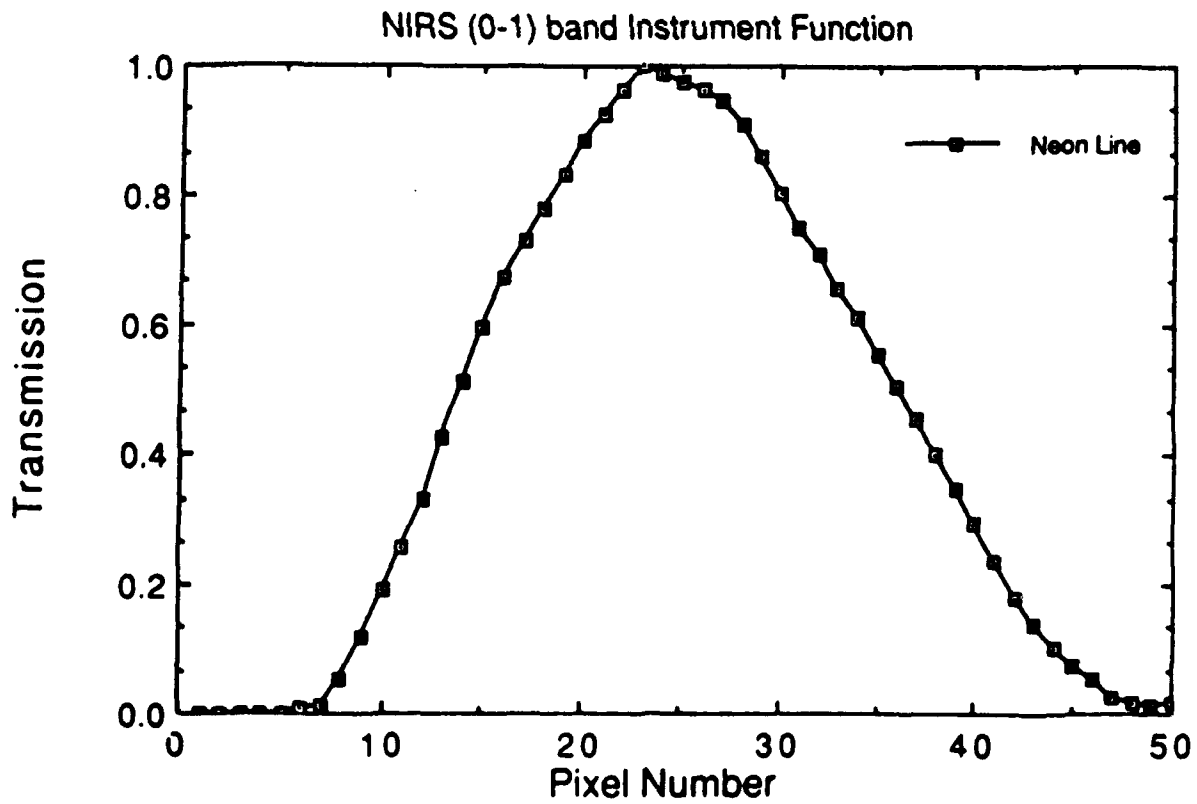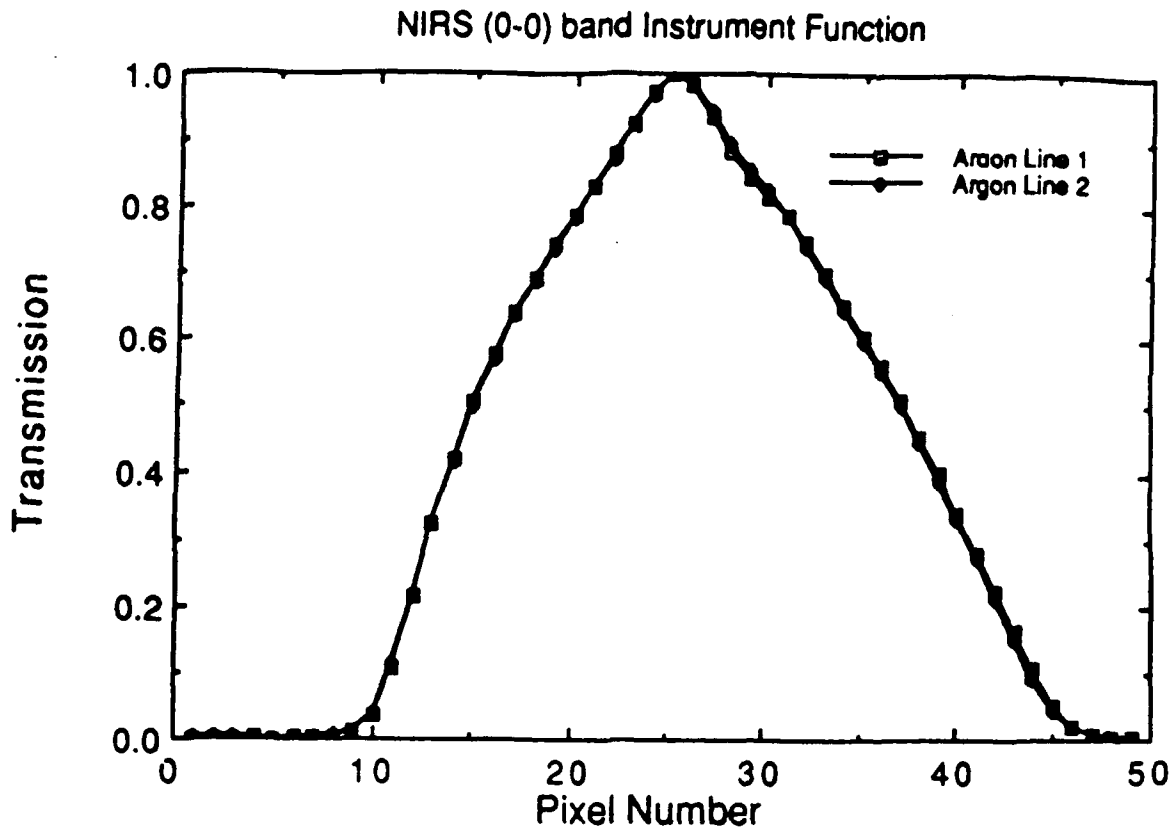
Figure 20

DATES Absolute Sensitivity Calibration
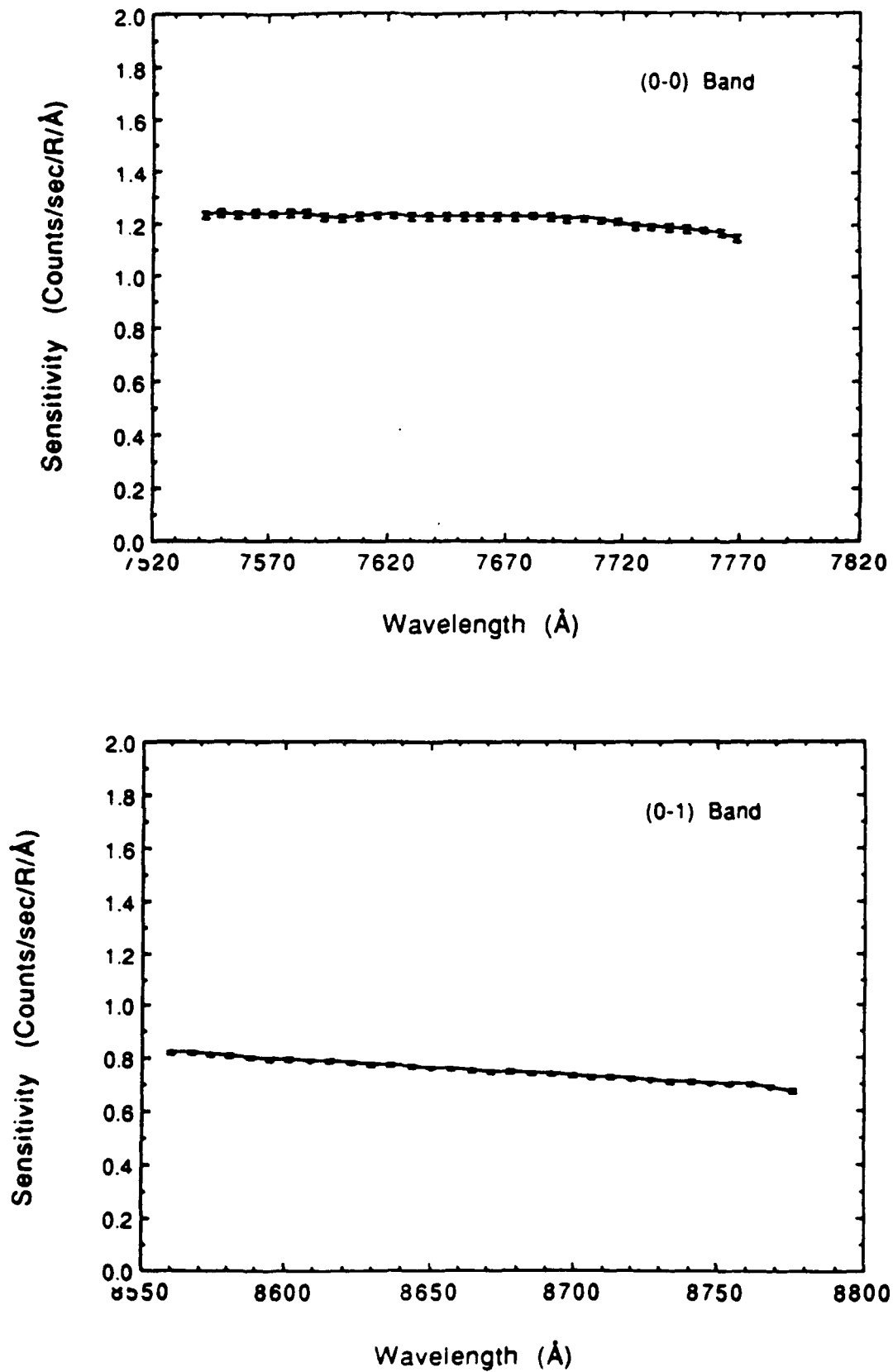
Figure 21

The dark current of the CCD detector, like the photon statistics, is found to follow the Poisson distribution. In other words, for a single measurement of dark signal of 775 counts (or 12,096 electrons), the uncertainty is ~$(12,096)^{1/2}$ electrons or 7.05 counts, a mere <1% uncertainty. For the magnitude of signals (~1000 digital counts per 0.25 second) that DATES-1 observed (shown in the next section), the statistical uncertainty is less than a fraction of one percent.

Consequently, by adopting CCD solid state technology, we have obtained a second-generation remote sensing optical instrument which allows us to either measure atmospheric emissions more accurately or detect the emission features previously unavailable (especially at spectral regions beyond 8000 Å). A summary of DATES-1 instrumental parameters is shown in Table 2.

Table 2. Summary of DATES-1 Instrument Parameters

Main Instrument	1/4 meter Ebert Fastie Spectrometer
Telescope F-number	f/5
Objective Lens Focal Length	150 mm
Field of View	0.0717° x 1.26°
Input Slit Size	0.38 x 6.62 mm
Grating Density	1200 lines/mm
Interference Order	1
Detector Array size	384 x 288 pixels @ 23 x 23 μm/pixel
Detector Temperature	-36.5 C
Detector Dark Current	14 electrons/pixel/sec
Wavelength (Å)	7620 Å (0-0) , 8650 Å (0-1)
Spectral Coverage	234 Å (0-0), 222 Å (0-1)
Wavelength per pixel	0.61 Å @7600 Å, 0.58 Å @8600 Å
Spectral Resolution	13.4 Å
Spectral Channels	32
Wavelength per channel	7.3 Å @7600 Å, 6.95 Å @8600 Å
Sensitivity (c/sec/R/Å)	1.2 @7600 Å, 0.8 @8600 Å
Integration Time	0.25 second
Mass	1.5 kg
Dimension	86 cm x 25 cm
Power	42 watts average, 75 watts peak
Data Rate	315 bytes per second

3.2.2   DATES-1 Operational Mode

All phases of instrument operation were under the direct control and supervision of the DATES-1 control computer. The control computer was designed to function as a spacecraft instrument package and it contained nonvolatile memory which held up to 8 different operating modes, 7 of which could be programmed to change such things as CCD readout binning pattern, integration time, etc. The control computer was also capable of switching from one program mode to another basing upon a time mark from its own internal clock. DATES-1 was programmed to be operated during the MAP rocket in three different modes, as described in Table 3.

Table 3. DATES-1 Operational Mode

	Mode 0	Mode 1	Mode 2
Function	Calibration	Airglow	Airglow
Calibration Lamp	on	off	off
Spectral Region	(0-1) @8600Å	(0-0) @7600Å	(0-1) @8600Å
Integration Time	2 seconds	0.25 second	0.25 second
CCD Binning	1 by 288	12 by 36	12 by 288
Spectral Channel	384	32	32
CCD Temperature	-36.5 C	-36.5 C	-36.5 C
Duration (second)	60 seconds	2 seconds	2 seconds
Next Mode	Mode 1	Mode 2	Mode 1

The DATES-1 operational mode was programmed to follow the attitude and pointing of the MAP rocket launched in July 1989. It started with ~60 seconds of instrument calibration so that the behavior of DATES-1 spectrometer, such as sensitivity and instrument drift, could be monitored. At 60 seconds after launch, DATES-1 was switched to science mode 1, which measured the O_2 Atmospheric (0-0) band emission at 32 spectral wavelength bins with an integration period of 0.25 seconds. After taking the (0-0) band emission measurements for 2 seconds (8 frames), DATES-1 was switched to mode 2 and measured the (0-1) emission with the same integration time and duration. Note that this operational mode can easily be modified to satisfy the particular requirements. The CCD binning patterns were determined so that the signal levels would not be saturated according to theoretical simulation and could be easily modified. Since the (0-0) band emissions were ~20 times stronger than those of the (0-1) band, a binning pattern of 12 x 36 (1/8 of the frame) was selected to avoid CCD pixel full-well saturation and 14-bit digital readout maximum (16383).

43

3.2.3 Experiment

3.2.3.1 Experimental Description

The experiment was carried out in conjuction with the NASA Michigan Airglow Package (MAP) rocket experiment and launched by a Nike Black sounding rocket (NASA 27.122) from White Sands, New Mexico (32.5° North Latitude) on July 27, 1989 at 0100 UT. The solar zenith angle was ~10 degree at the time of the launch, and the payload reached an apogee of 223 km (Fig. 22). An inertial attitude control system (ACS) oriented the spectrometer for viewing the north-eastern horizon. The tangent height for the observation sequence ranged from 50 to 223 km. The limb observation commenced at a rocket altitude of ~190 km (~160 seconds into the flight) when the spectrometer line of sight had been positioned at 10.9° below the local horizon at a solar azimuthal angle of 87.7°. A solar azimuth angle of close to 90° during local noon made the scattering angle near 90°, consequently minimizing the continuum scattered light. This orientation was maintained until the rocket reached at an altitude of 210 km (~190 seconds) where the rocket spin axis (spectrometer optical axis) was pitched up at a rate of 0.184°/second to view the lower thermosphere at ~3.5 km/second. At the apogee (~240 seconds), the spectrometer was pitched back down at the same rate during the descent until ~300 seconds or the rocket descended down to ~205 km to repeat the observations of the lower thermosphere. After 300 seconds the rocket


Figure 22

44
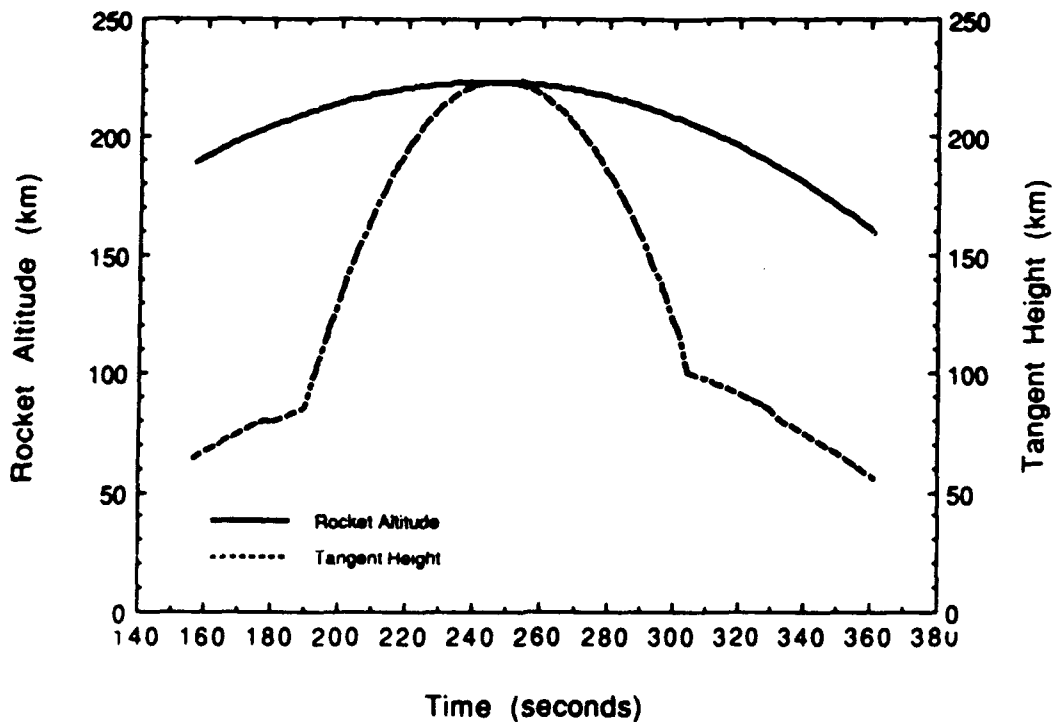
rocket orientation was maintained again at 10.9° below the horizontal which let the descent of the rocket do the tangent height scan which rans at ~1 km/second. While the rocket orientation was maintained at 10.9° below the horizontal during both the ascend and descent legs of the flights (~40 to 50 seconds), the spectrometer was able to measure the spectral brightnesses of the (0-0) and (0-1) emission bands between tangent altitudes of 60 and 105 km. The rocket altitude and tangent altitude as a function of flight time for the entire flight are shown in Fig. 22. The portions of the measurements with tangent heights between 50 and 120 km provided us with the necessary data to examine the remote sensing technique described in the previous section for the recovery of density and temperature in the region.

3.2.3.2 Experiment Results

The DATES-1 operational mode was designed to measure the (0-0) and (0-1) band spectral intensity every 2 seconds. For an integration time of 0.25 second, each set of measurements should contain eight frames of spectra before each 2-second spectral change. Because of the movement of the grating position, the first frame of each set was contaminated, and consequently it was discarded. In addition, except for the second frame, unexpected CCD readout command buffer overflows due to fast readout (0.25 second) also gave rise to incomplete spectral intensity signals in the (0-1) band spectra for the rest of the six frames. Only the first 18 spectral channels (out of the total 32) were read out successfully. We have attempted to predict the signals for the missing spectral channels by linearly interpolating the spectral signals obtained on the second frame. Figure 23(a) presents the measured (0-1) band emission spectra as a function of flight-time after including the predicted signals for those frames with incomplete data. During the two-second gap between each group of seven spectra as seen in the figure, the spectrometer was dedicated to measure the (0-0) band emission. The rocket attitude data suggests that a tangent height of 70 km is observed at ~160 seconds after launch during the upleg and a tangent height of 60km at ~360 seconds after launch during the downleg. The time range shown in the figure, from T+160 to T+195, and T+300 to T+360, gives an upleg altitude scan from 70 km to about 110 km, and downleg altitude scan from 110 km down to 60 km, respectively. The spectral signals as a function of tangent height between 60 and 120 km, which we use to determine the band volume emission rate and temperature profiles, are shown in Fig. 23(b). The 32 spectral channels covered ~230 Å as described in the instrument description section. Spectral signals at a higher number of channels represent measurements at shorter wavelengths, and the P and R branches of the O_2 Atmospheric band were clearly revealed near spectral channels of 18 and 23, respectively. It clearly indicates that the observed signals in this spectral region increase with decreasing tangent height due to the increase in continuum scattered emission. Very slight variation of the spectral brightness of the (0-1) band emission with tangent height can be found. This is significantly different from the one observed for the (0-0) band as shown in Figs. 24(a) and (b). Due to self-absorption by the molecular oxygen, the (0-0) band emission brightness becomes weaker as the tangent height decreases, as suggested by the theory. The O_2 number density profile can be

Figure 23

0-0 Spectrum

0-0 Spectrum

Figure 24

47
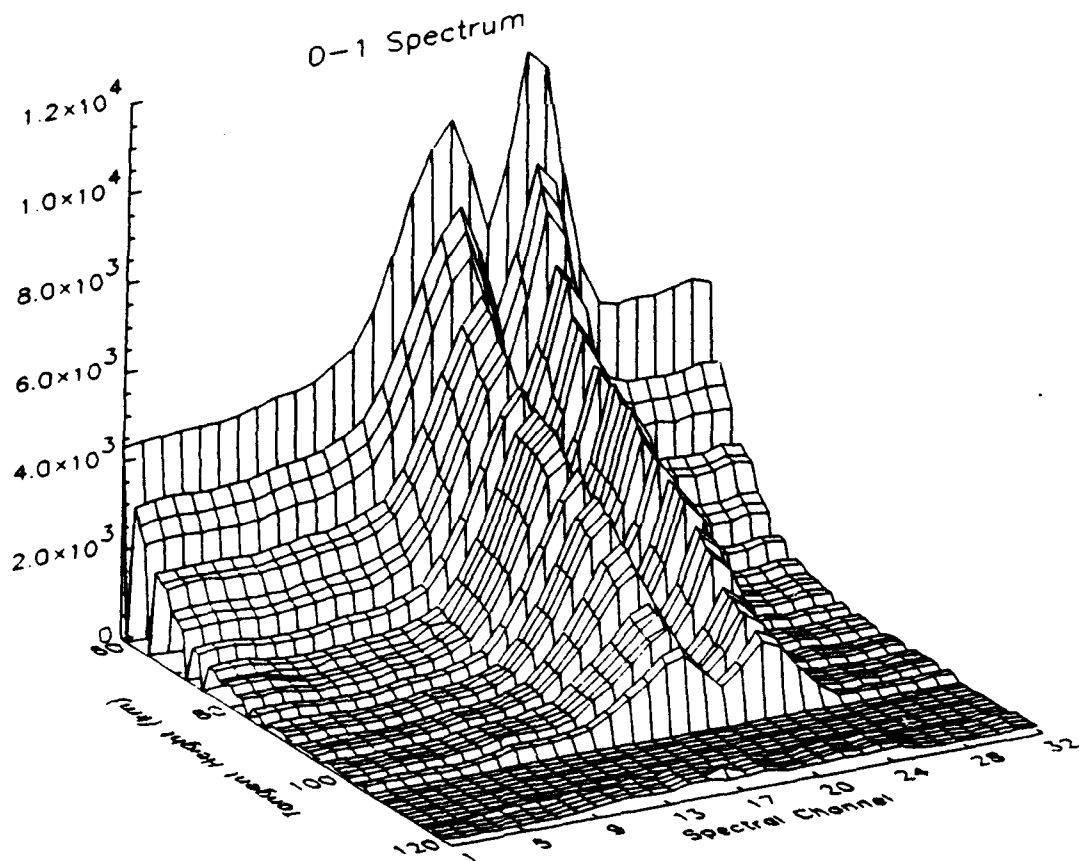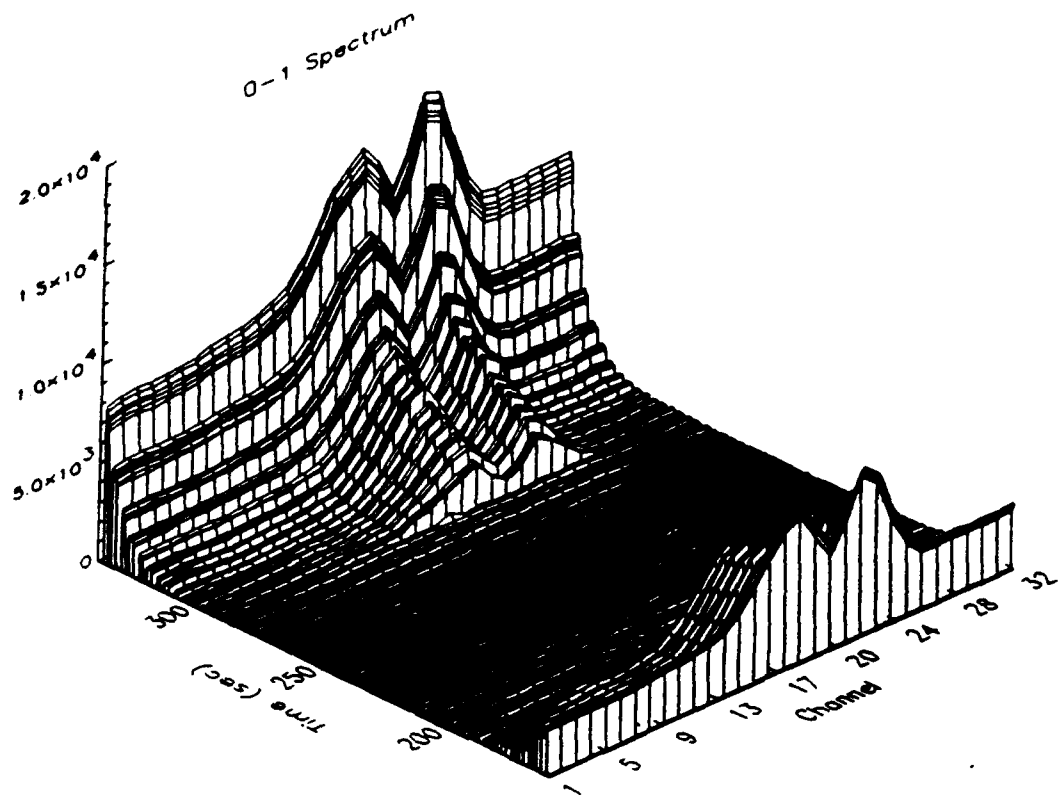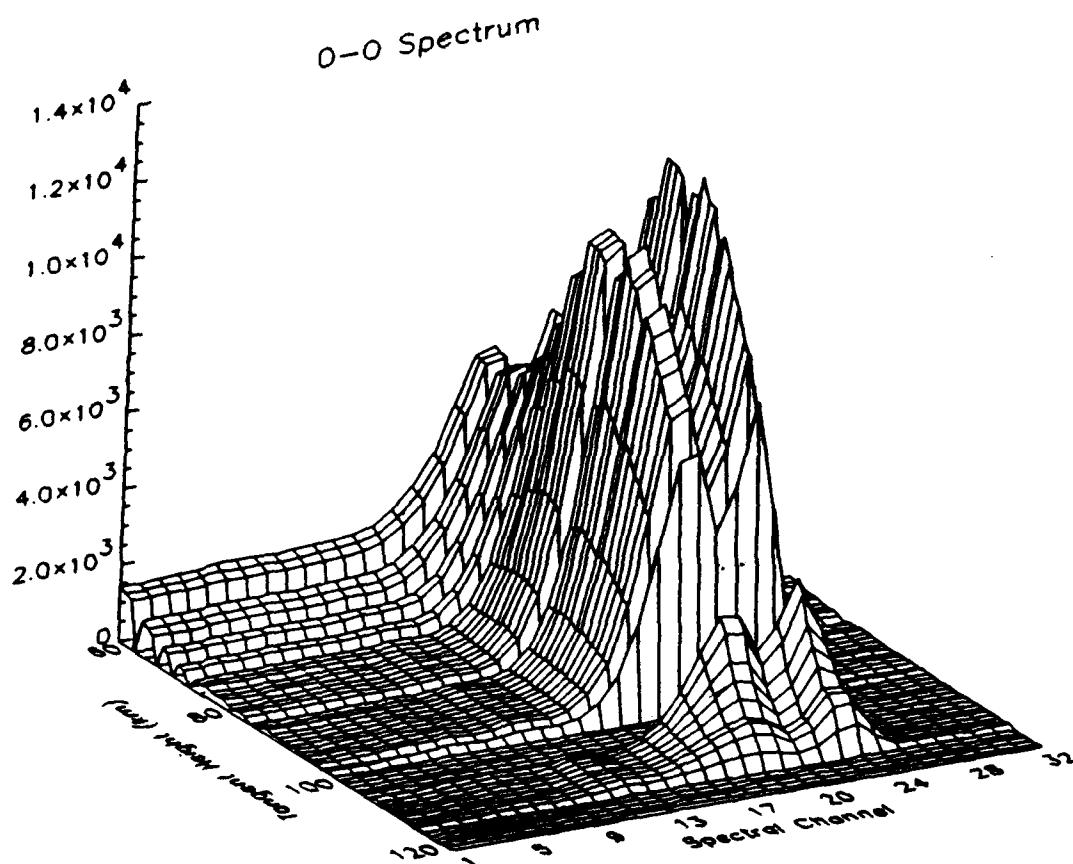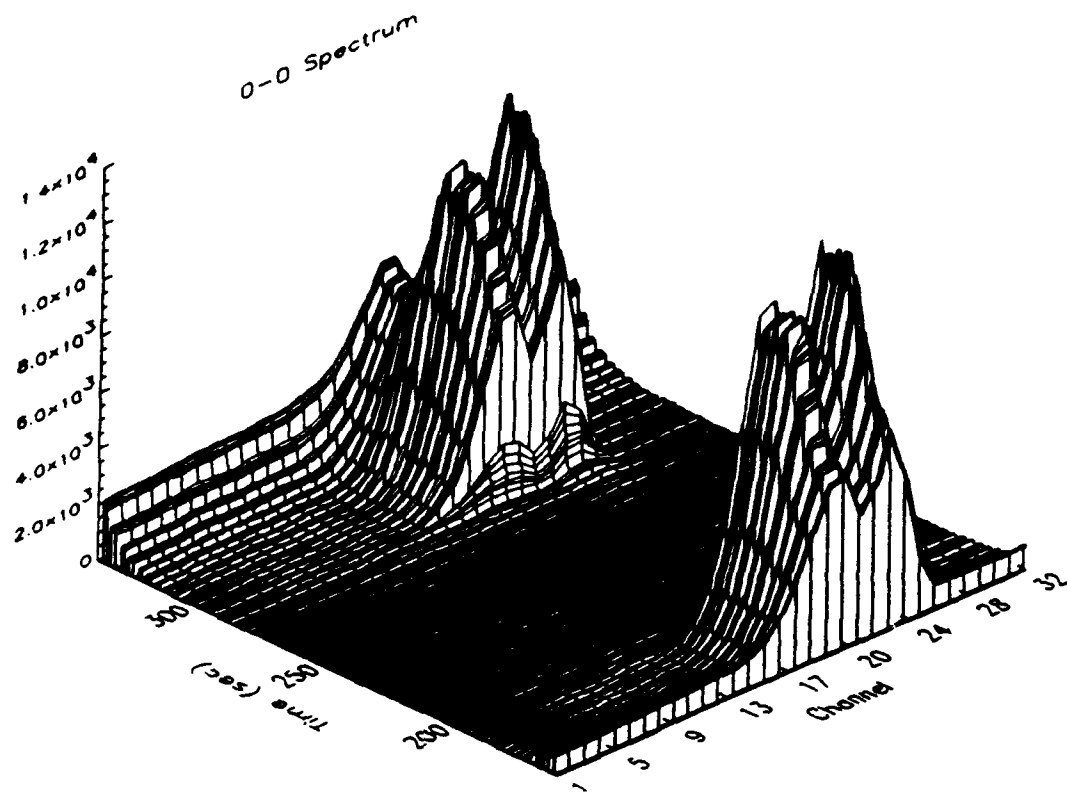
deduced from the amount of self-absorption of this emission and its variation with tangent height. This will become clear later as we present the fitted band brightness for both (0-1) and (0-0) bands as a function of tangent height.

We should also point out here the small enhancements in the signals of both (0-0) and (0-1) band spectra near spectral channels 6 and 11 for higher tangent height measurements (T+200 to T+300). They indicate the increasing importance of the O_2 (1-1) band and (1-2) band emissions respectively as the tangent height increases. In fact, although being very weak, some emissions from the N_2 first positive system (N_2 $B^3\Pi_g \rightarrow A^1\Sigma_g$) also contribute to the observed (0-0) and (0-1) band spectra. Figure 25(a) shows the measured (0-1) band spectra at a tangent height of 90 km. We found that the observed spectra is dominated by the O_2(0-1) band emission with small contributions from the O_2 (1-2) band and N_2 1st Positive (1-0) and (2-1) band emissions. A rotational temperature of 500 K has been assumed for the N_2 1PG system since its emission originates in the lower thermosphere near 150 km. Rotational temperature of ~210 K and 601 K are obtained from the fit for the O_2 (0-1) and (1-2) bands, respectively. A higher rotational temperature for the (1-2) band suggests that its emission is mainly produced at an altitude higher than the (0-1) band. Other fitted parameters, such as band brightness, are also shown. The quality of the fit can be clearly demonstrated by looking at the comparison between the fitted and observed signals at the weaker emission channels, as shown in Fig. 25(b).

Figures 26(a) and (b) present the fitted rotational temperature and band intensity of the (0-1) band emission as a function of tangent heights. A minimum line-of-sight temperature of ~181K is found to be located at ~80 km near the mesopause, and no noticeable difference was found between the results taken during the upleg and downleg of the flights. Clearly, the (0-1) band emission brightness increases with decreasing tangent height and inversion has to be applied in order to recover the band volume emission rate and rotational temperature profiles. We should point out here that all the data analysis and the results given hereafter were obtained by using only the first 18 measured spectral channelsof the (0-1) bands.

Figure 27(a) gives the measured (0-0) band spectra at a tangent height of 119 km. Excellent fit can be obtained, especially near the wings of the O_2(0-0) band emission as it is revealed in Fig. 27(b), if we include contributions from the O_2(1-1) and N_2 1st positive (3-1) and (2-0) band emissions. A rotational temperature of ~405 K is obtained for the (0-0) band emissions. At lower tangent height measurements, one has to consider self-absorption by O_2 in order to obtain a good fit to the observed spectra. As suggested by the theory, the (0-0) band emission brightness, shown in Fig. 28, becomes weaker as the tangent height decreases due to self-absorption. The density measurement can then be accomplished by observing the ratio of the signals between the nonabsorbing (0-1) and the self-absorbing (0-0) bands of emission in the lower mesosphere. For the measurements of O_2 density profile, absolute sensitivity is not critical but relative sensitivity between the two is crucial. If both emissions are optically thin, such as the measurements above

DATES (0-1) Band Measurements
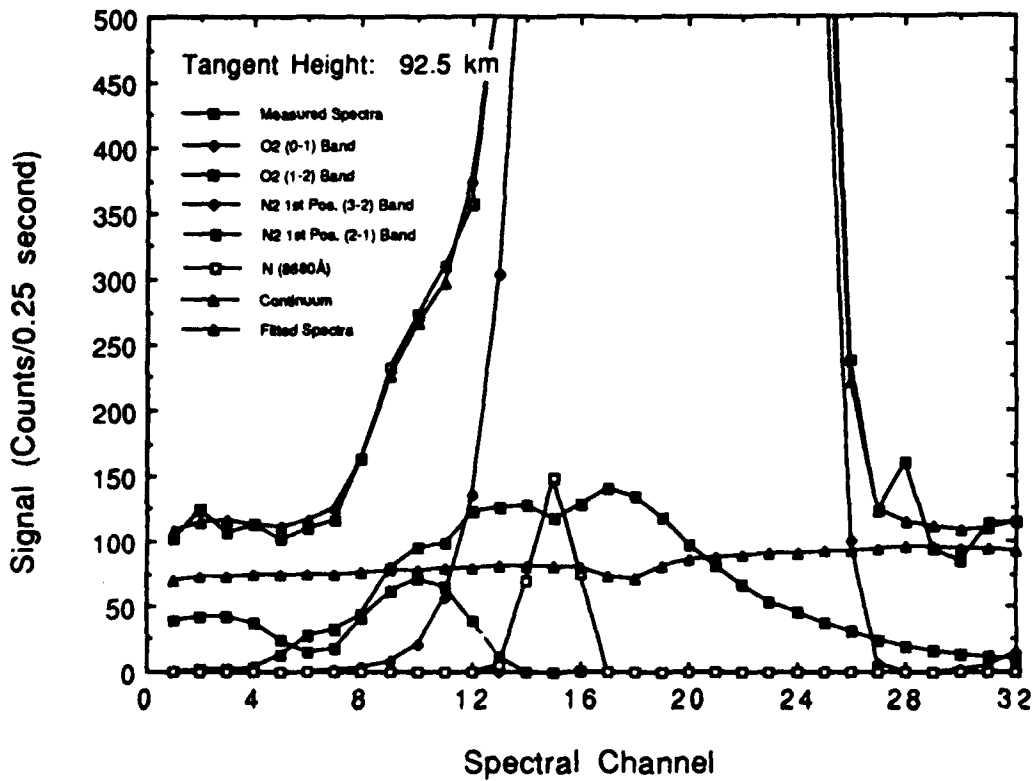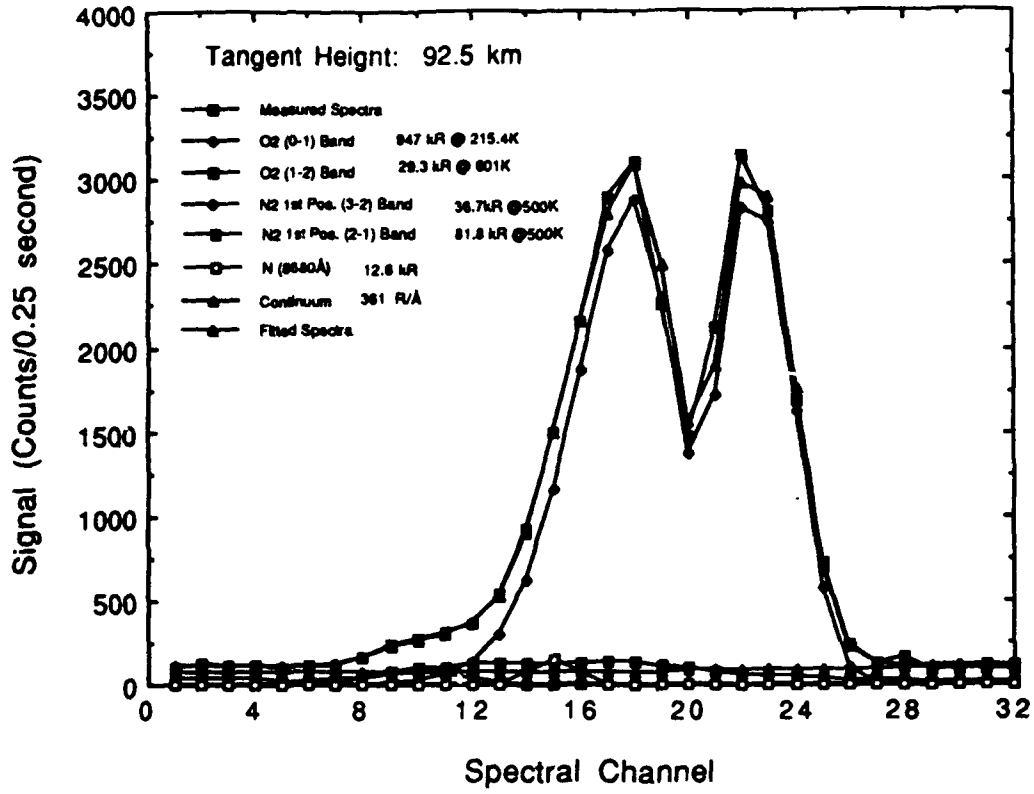
Figure 25
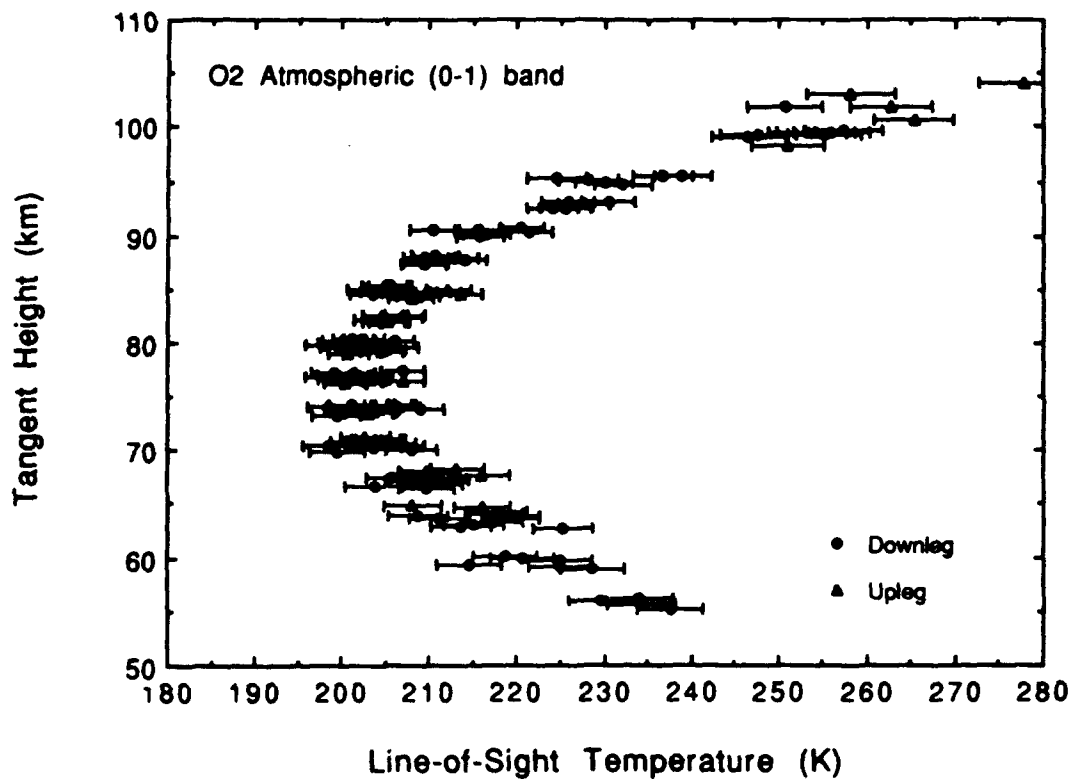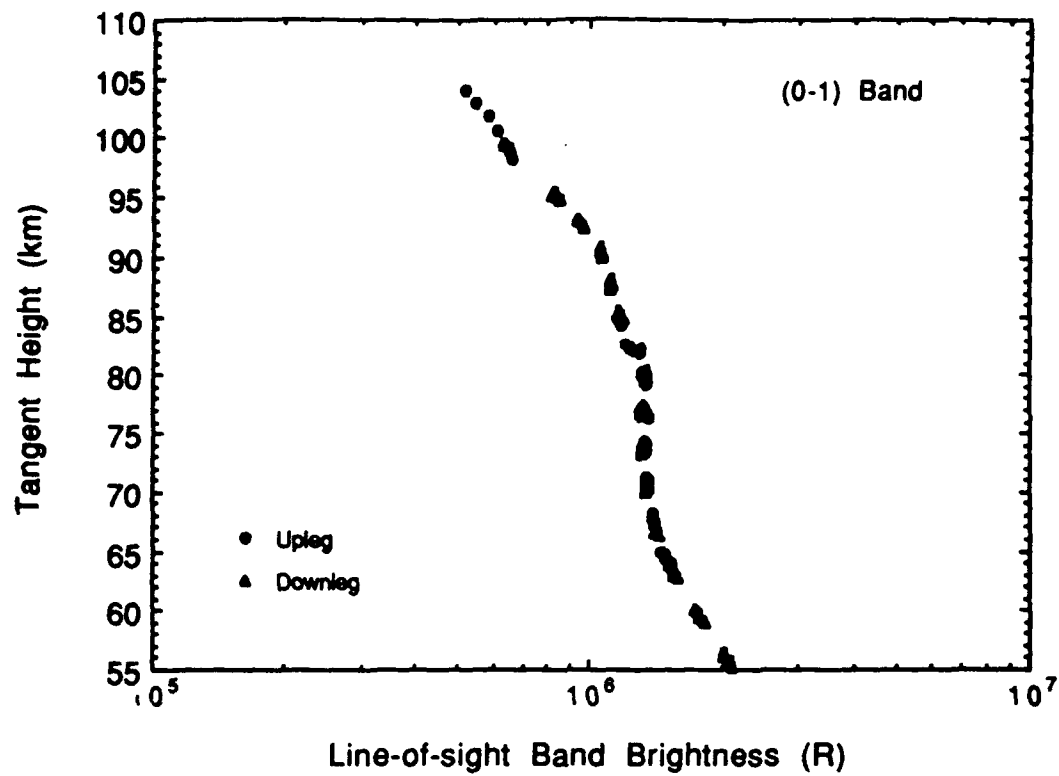
Figure 26

DATES (0-0) Measurements

Tangent Height: 119.4 km

Measured Spectra		
O2 (0-0) Spectra	1670±54 kR	@405±15K
O2 (1-1) Spectra	209±69 kR	@ 532±143K
N2 (3-1) Spectra	112±26 kR	@400K
N2 (2-0) Spectra	63±78 kR	@400K
OI (7774Å)	20±11 kR	
Total Fitted Spectra		

(Reduced X2: 5.85)

DATES (0-0) Measurements

Tangent Height: 119.6 km

- Measured
- O2 (0-0) band
- O2 (1-1) band
- N2 1st Pos. (3-1) band
- N2 1st Pos. (2-0) band
- OI (7774Å)
- Continuum
- Fitted Spectra
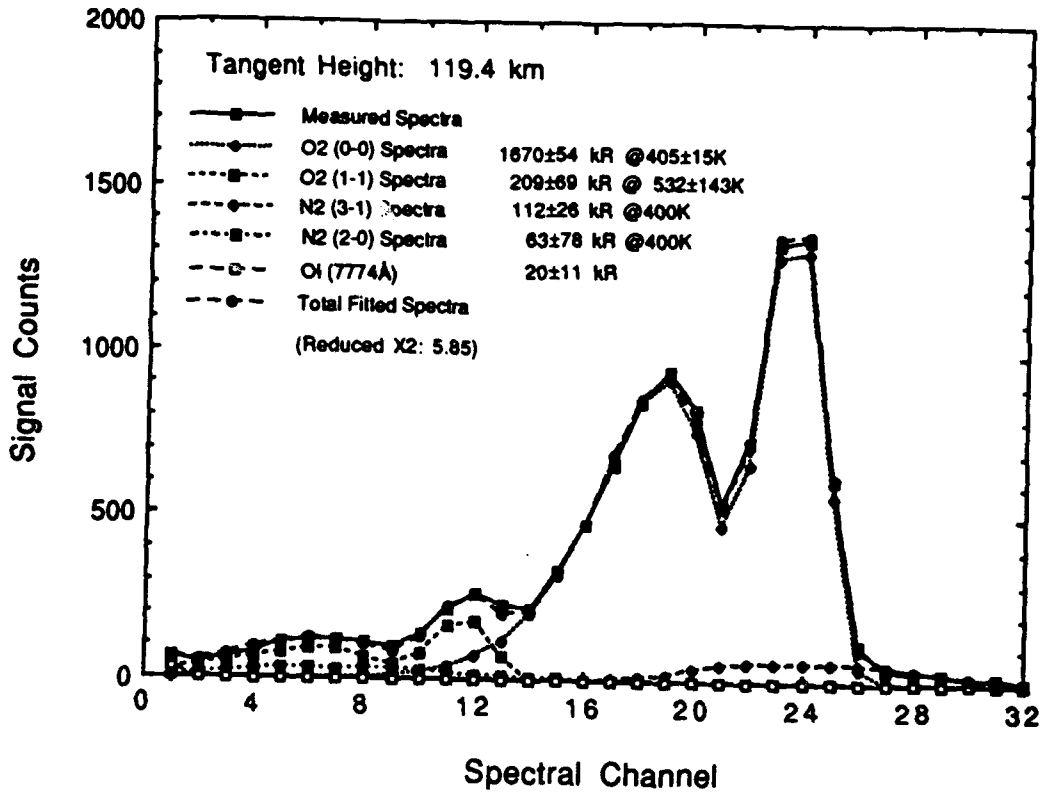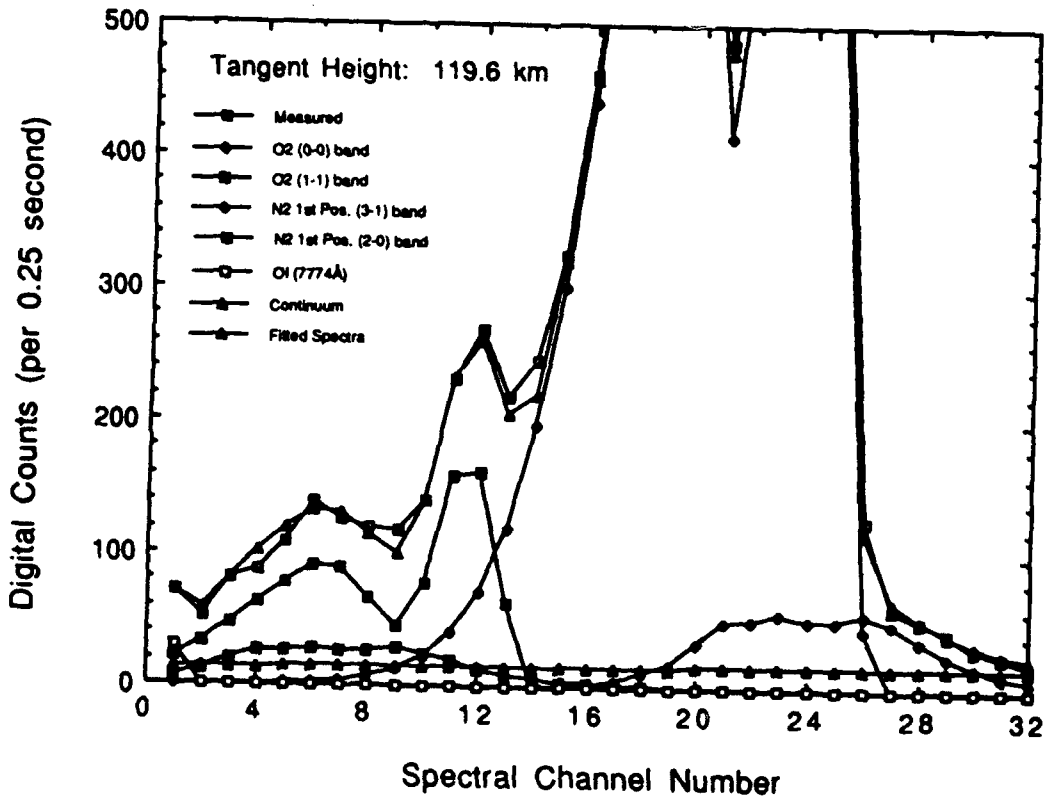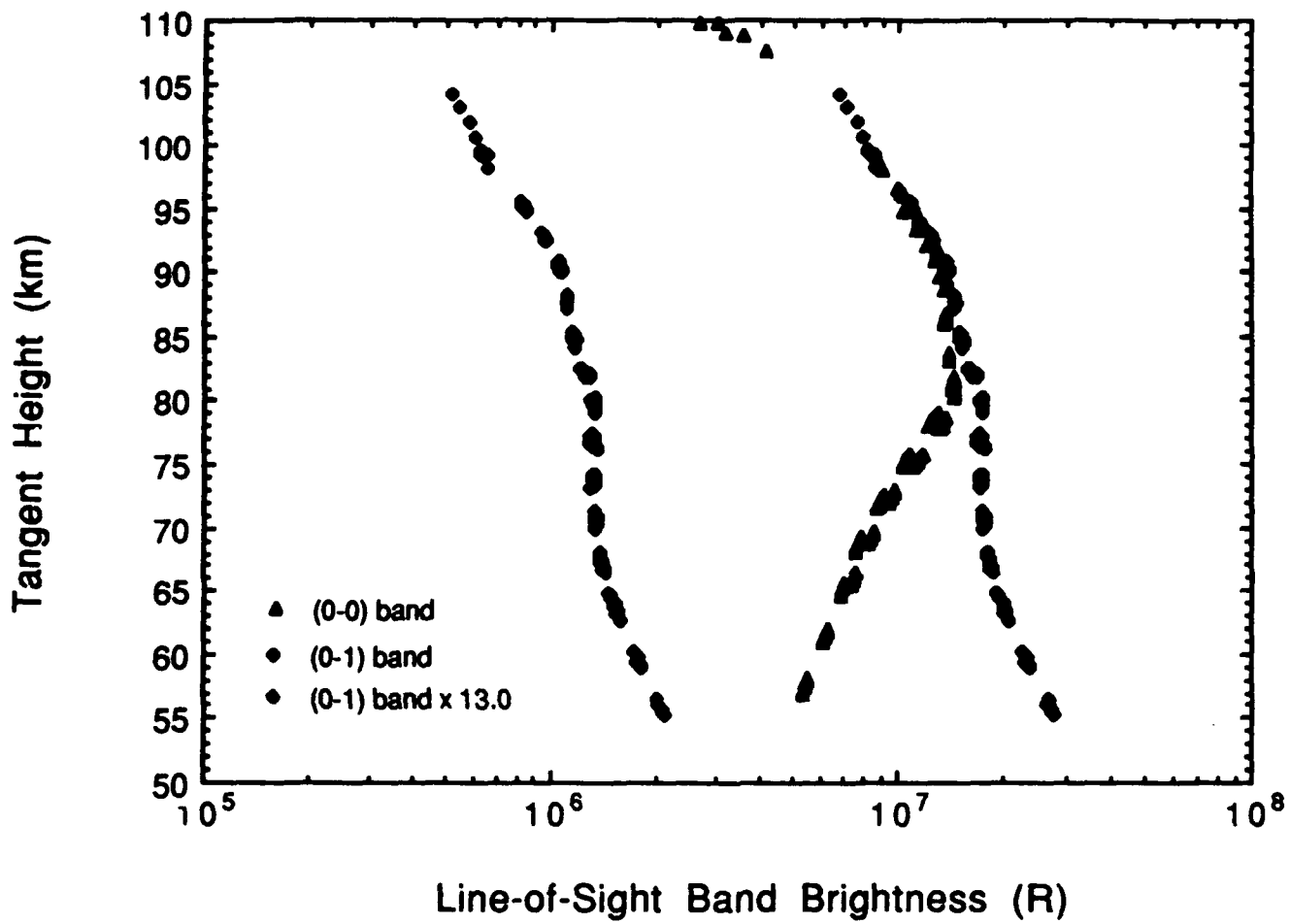
Figure 27

Figure 28

INVERTED VOLUME EMISSION RATE SIGNAL
O2 ATMOSPHERIC (0-1) BAND
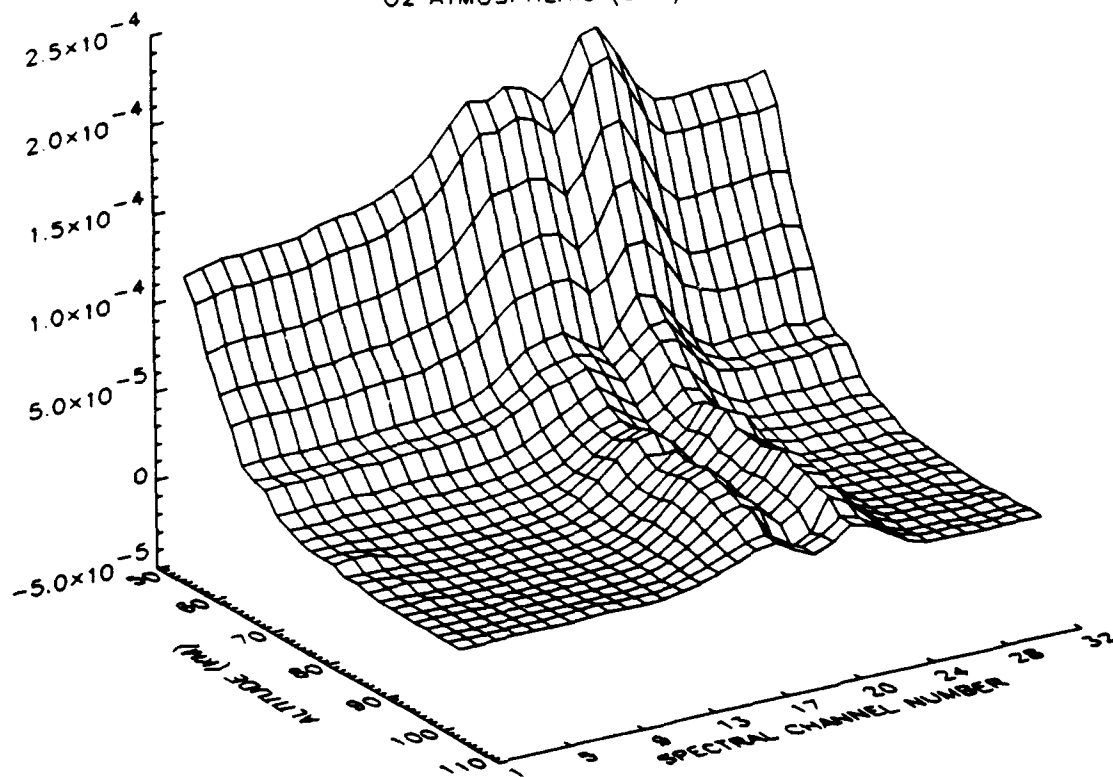
Figure 29

100 km tangent height, this ratio is directly related to the transition probabilities of the two emission bands (or Franck-Condon factors). Here we found the ratio to be 13.0, which is different from the theoretical value of ~20.

In order to obtain the non-absorbing (0-0) band brightness from the (0-1) band volume emission rate profile and the 'true' atmospheric temperature, inversion has to be performed to the measured (0-1) band signals. Here we used a technique similar to the one described in the final report from our feasibility study to perform inversions on all 32 spectral channels. A constrained linear inversion technique using first difference (Twomey, 1977) as the smoothness constraint was used and the inverted (0-1) band volume emission rate spectral signals for all the 32 wavelength channels as a function of altitude were presented in Fig. 29. One can then fit these volume emission rate spectra to obtain the temperature, band volume emission rate and continuum emission rate profiles. Figures 30(a) and (b) show the recovered (0-0) band volume emission rate profile and its estimated statistical error, after taking into account the (0-0) to (0-1) band brightness ratio of a factor of 13.0 obtained previously. It has a volume emission rate of $\sim 10^5$ photons/cm^3/sec at altitude regions between 50 and 100 km, and it agrees very well with the theoretically calculated emission rate of Bucholtz et al. (1986). Based upon the accuracies of our spectral brightness measurements, we estimated that the band volume emission rate profile recovered here has a statistical error of around 1% at all altitudes between 55 and 100 km. It should be pointed out here

(0-0) Band Volume Emission Rate (#/cm3/sec)

Percent Error in Volume Emission Rate
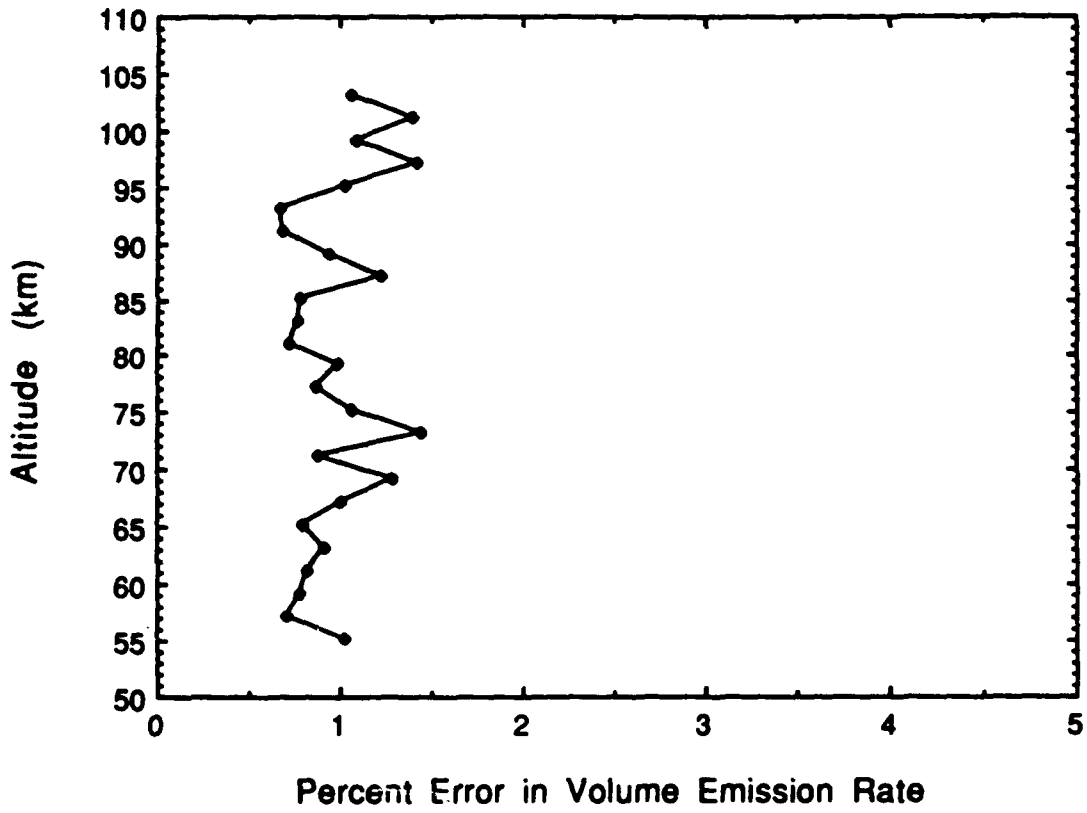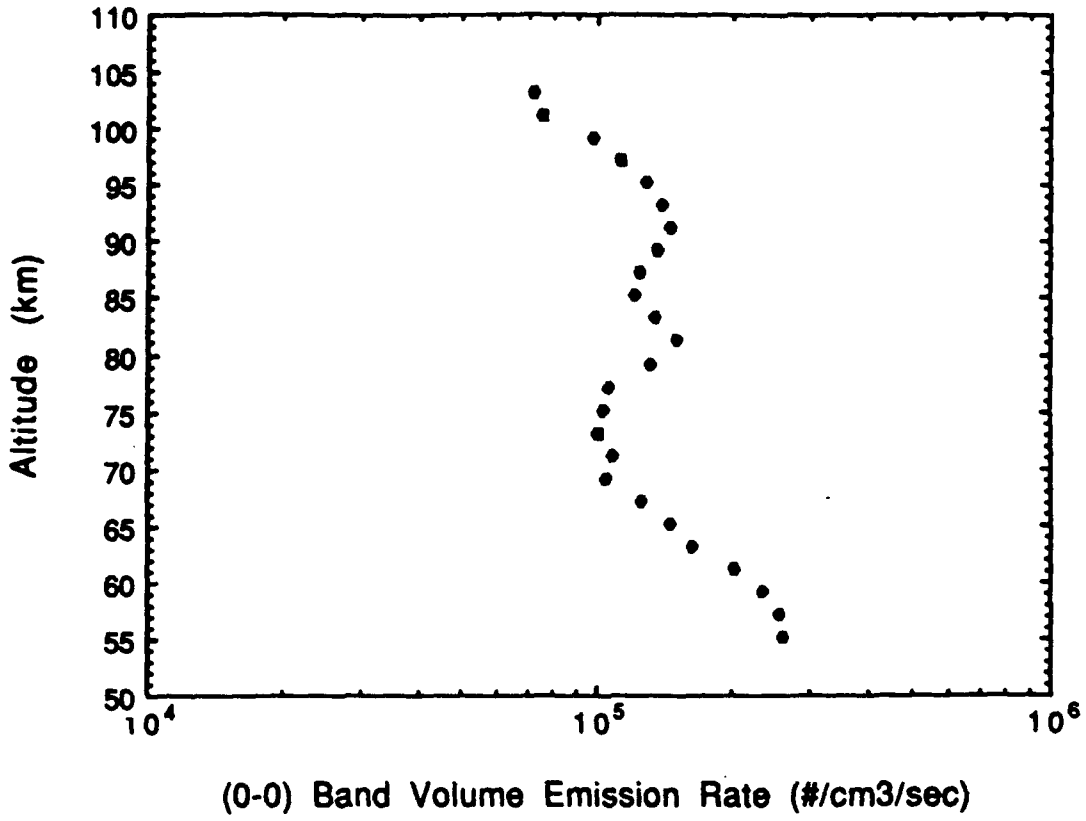
Figure 30

that the estimated error has been improved by constraining our profile with the first difference smoothness.

Figures 31(a) and (b) present the recovered temperature profile and its estimated statistical accuracy. The recovered temperature profile reveals a mesopause temperature of ~185 K near 85 km and is estimated to have a statistical error of ~3 K. Our temperature measurements show variations with amplitude larger than the estimated statistical variation of 3K, especially in the region near the mesopause. We believe that this is due to the uncertainty of the knowledge of rocket pointing in this region while the rocket ACS system is performing pitch angle adjustments, as indicated in Fig. 22. Figure 32 compares the DATES measured temperature profile to the AFGL model atmosphere for July at 30 N and the CIRA mean reference atmosphere. The agreement between the two is very good, except at low altitudes near the stratopause where the DATES measured temperatures are higher. As the tangent height decreases, the continuum background brightness produced by the molecular and aerosol scattering increases. Uncertainty in the knowledge of the spectral shape of the continuum will result in errors in the recovered temperature. We will address this issue and how to improve DATES temperature measurements at lower altitudes in the discussion section.

Figures 33(a) and (b) present the recovered O_2 number density profile and its comparison with the mean CIRA reference atmosphere. The statistical errors in our density measurements were ~2-6 percent (cannot be shown in the log-scale), increasing as the altitude increases. The density profile recovered here has been constrained to the hydrostatic equation according to the temperature profile shown previously. There is a noticeable difference between our measurement and the model at higher altitudes above the mesopause. Since there is little (0-0) band self-absorption at altitudes above 95 km, the density recovered in this region is mainly derived from the measured temperature profile and the density measurements below.
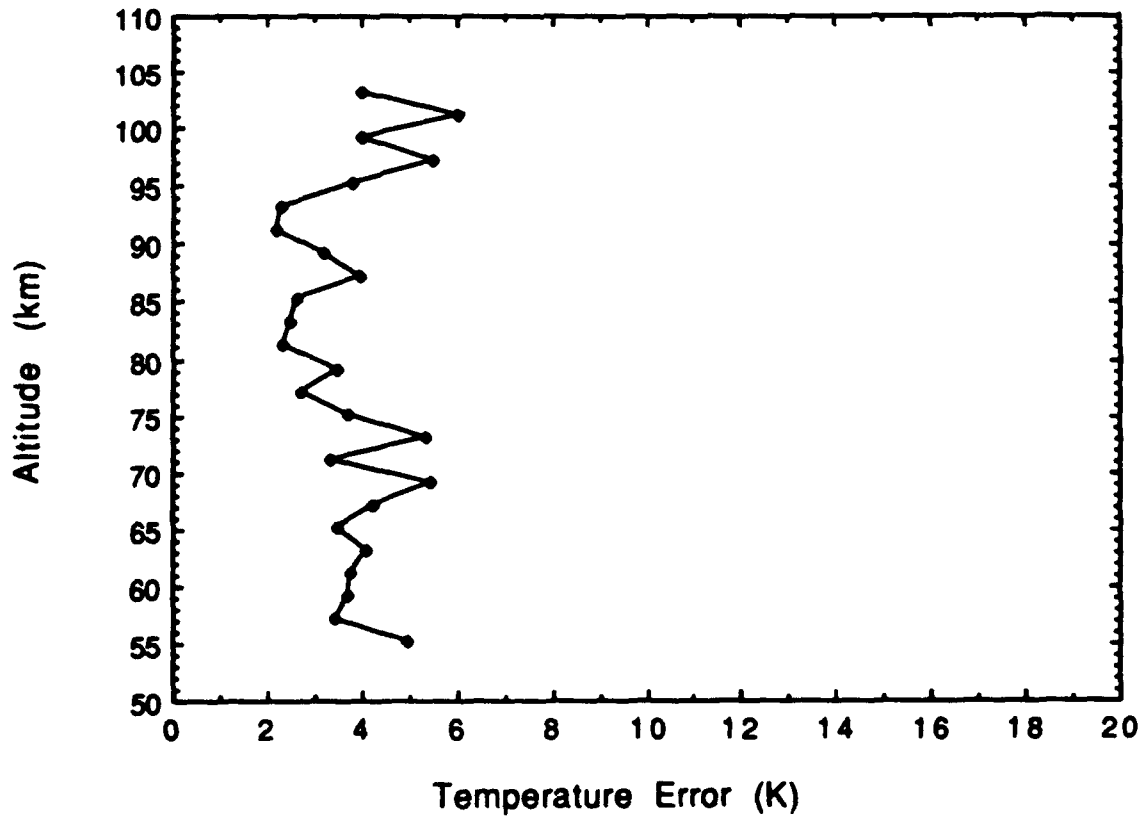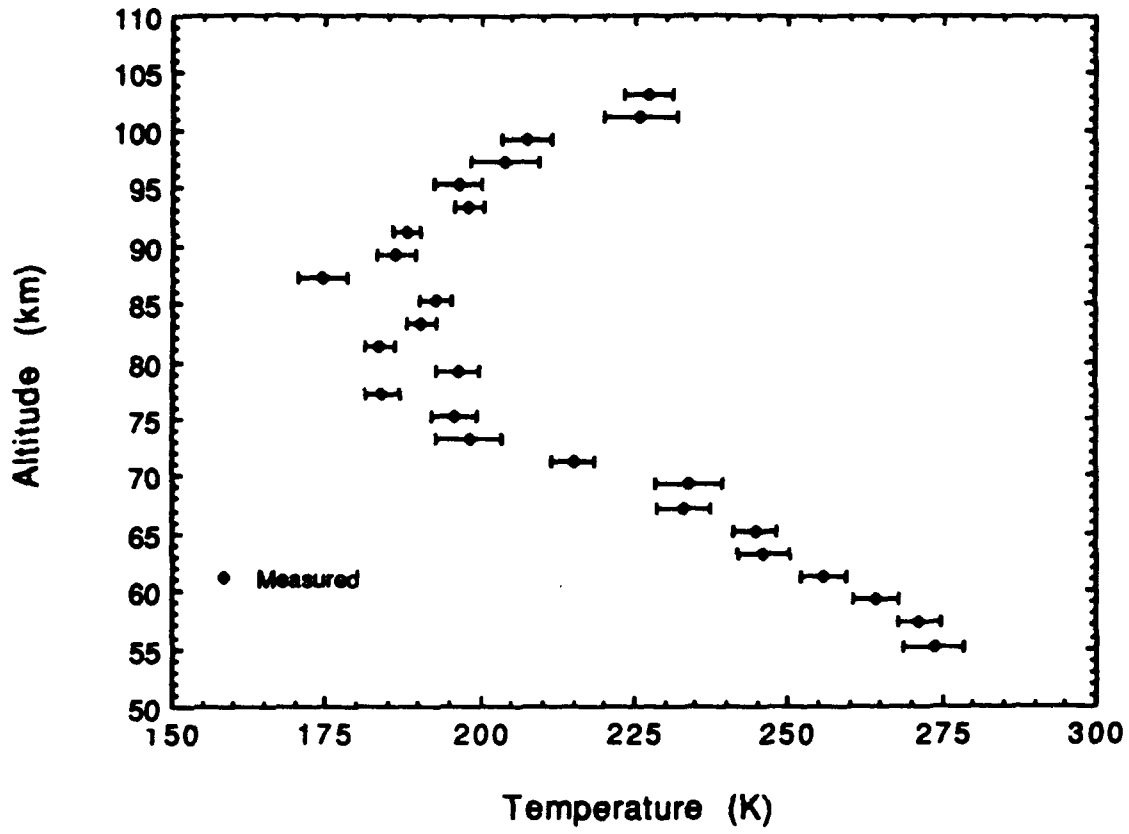
Figure 31
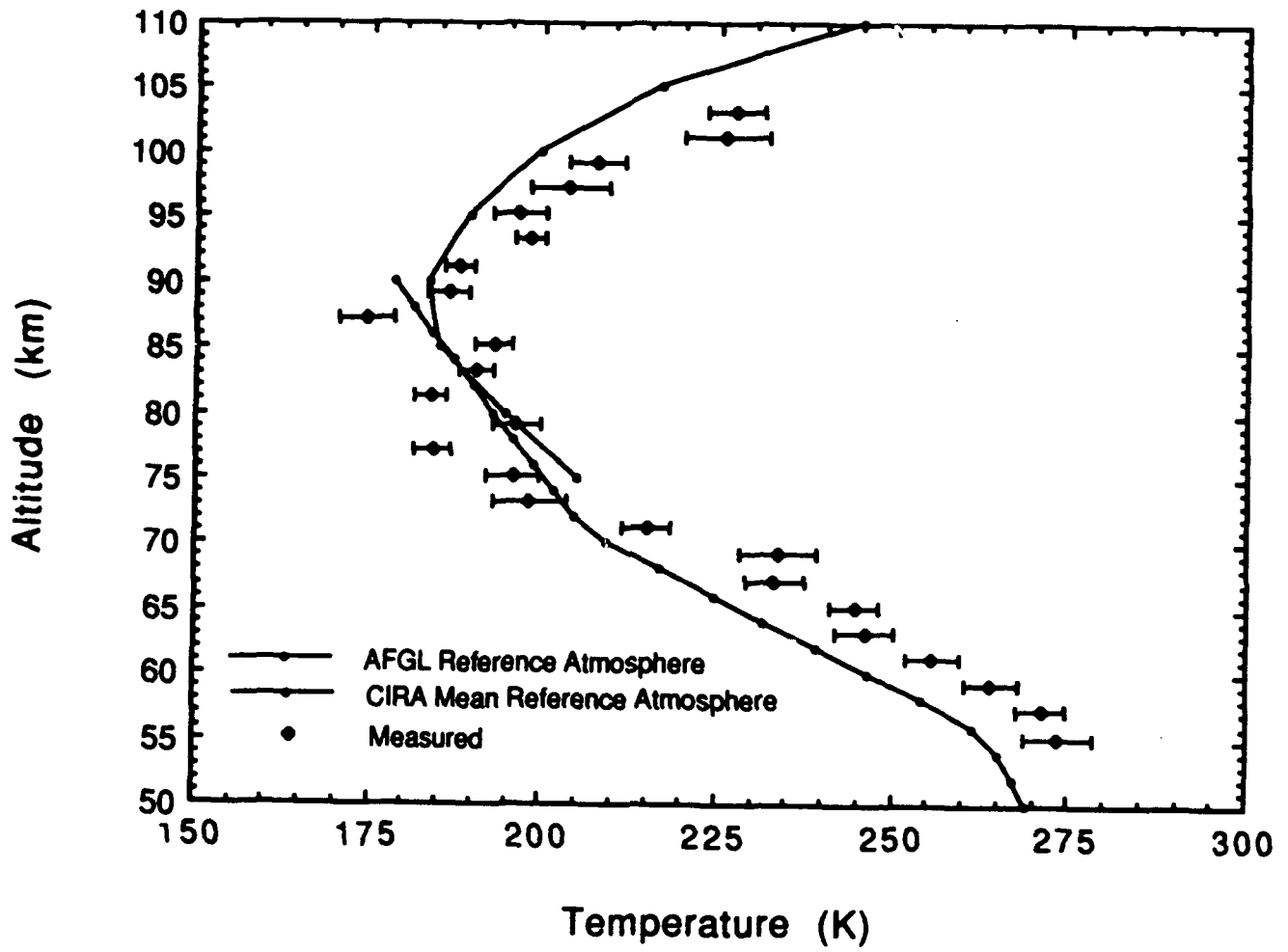
Figure 32
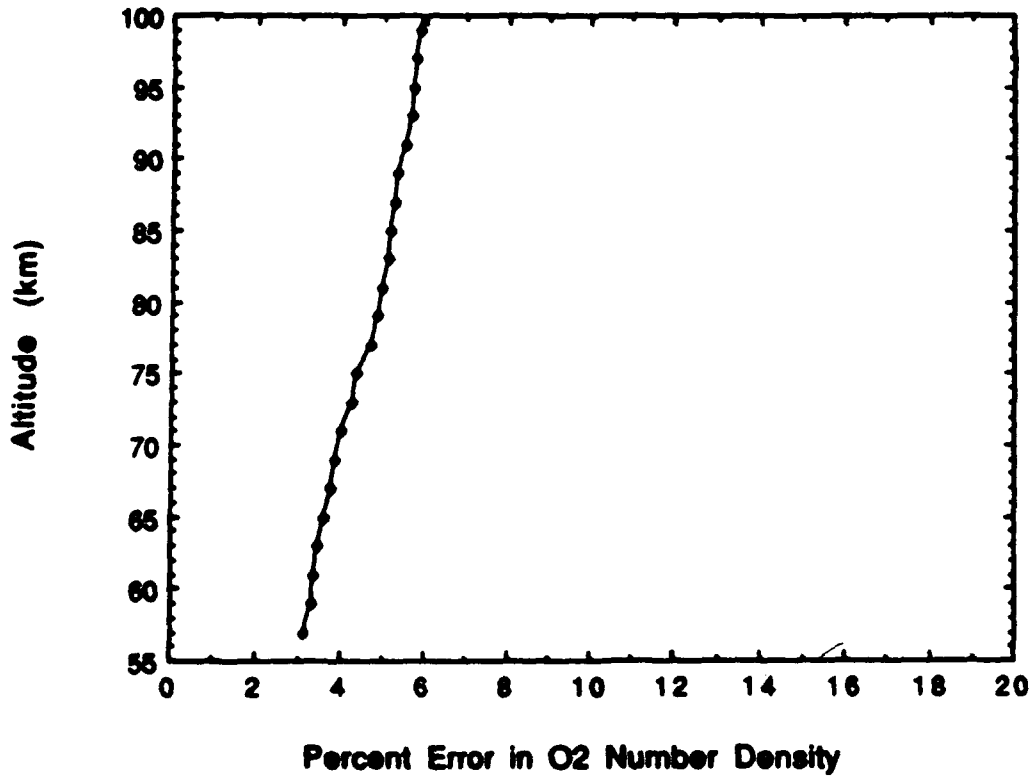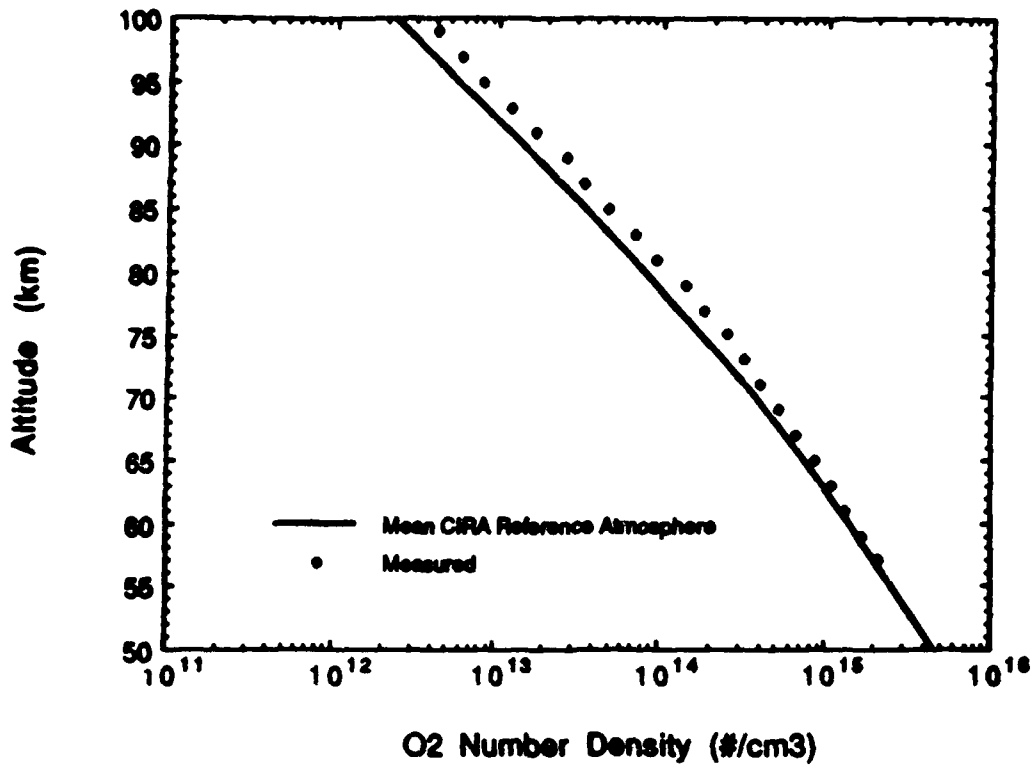
Figure 33

3.2.4   Summary and Discussion

The algorithm used to recover temperature and density profiles can be summarized as follows (profiles obtained from data taken during previous MAP flights were shown for demonstration):

(1) measure emission spectra of the O_2 (0-1) and (0-0) bands at various tangent heights,

(2) determine the brightness ratio between the (0-0) band and the (0-1) band based upon brightnesses measured above 100 km tangent heights; this ratio can be used to confirm our sensitivity calibration and it should be related to the Franck-Condon factor modified by the v^3,

(3) invert the measured O_2(0-1) band spectral brightness to obtain the (0-1) band volume emission rate profile and the rotational temperature profile (= ambient kinetic temperature),

(4) compute the (0-0) band volume emission rate profile from the measured (0-1) volume emission rate profile using the ratio determined in step 2,

(5) calculate the (0-0) band spectral brightness at various tangent heights based upon a guessed O_2 number density profile,

(6) compare with the measured (0-0) band spectral brightness and determine the corrections needed for the O_2 number density profile,

(7) repeat (5) and (6) until the correction terms become very small.

Since the emission rate of $O_2(^1\Sigma)$ measured by DATES is produced partly by $O(^1D)$ reaction with O_2 following photolysis of O_2 and O_3, in principle, one can determine the number densities of $O(^1D)$ and O_3 from our measurements as well. The concentration of ozone in this region of the atmosphere has usually been indirectly inferred from the $O_2(^1\Delta)$ 1.27 μm emission produced by the photolysis of O_3. The concentration of $O(^1D)$ atoms in this region is low, approximately 10^2-10^3 cm^{-3}, and is very difficult to measure through the 6300 Å emission because of the presence of rayleigh scattering. The $O(^1D)$ atoms are very important in the mesosphere and lower thermosphere due to their involvement in the HO_X chemistry, i.e. $O(^1D) + H_2O \rightarrow 2OH$ and $O(^1D) + H_2 \rightarrow H + OH$. DATES will provide, for the first time, a viable technique to infer the concentrations of these two important O_x species along with the concentration of the major species, O_2 and atmospheric temperature. We will describe the algorithms used to recover density profiles of $O(^1D)$ and O_3 and assess the accuracies of the inferred densities through DATES measurements in the next section.

Here we would like to address an issue which might have some significant impact on future DATES measurements. According to our DATES-1 measurements, the ratio of (0-0) band intensity to (0-1) band intensity was found to be ~13.0. This is smaller than the theoretical value of 20.0, calculated based upon the the Franck-Condon factor ratio of 13.8 and the v^3 dependence of 1.45. The smaller ratio obtained here could result from errors in our absolute sensitivity calibration. Errors in the absolute sensitivities in the two spectral regions where measurements were conducted will give rise to inaccurate emission brightnesses. Error in the relative sensitivities

Tangent Height (km)

110
105
100
95
90
85
80
75
70
65
60
55
50

- 6570Å @ (0-1) band
- 7570Å @ (0-0) band
- (0-1) band x 1.8

10²   10³   10⁴   10⁵

Continuum Brightness (R/Å)
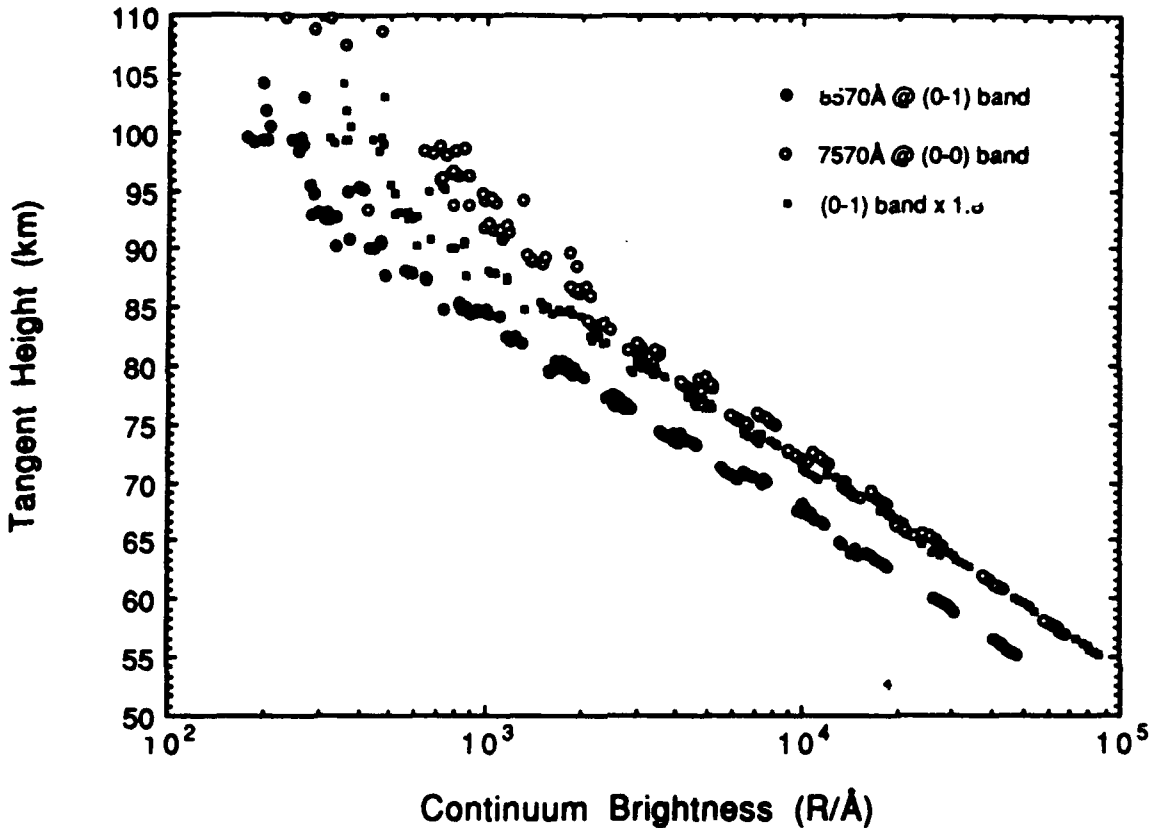
Figure 34

clearly will give an erroneous determination of the band intensity ratio. However, this possible relative error can be examined from the measured continuum emission (Rayleigh scattered) brightnesses between the two spectral bands. Figure 34 presents the fitted continuum brightnesses for the (0-1) and (0-0) band spectral region as a function of tangent height. Solar spectra given by Labs and Neckles (1981) normalized at 7570 Å and 8570 Å are used as the solar spectral shape in our fitting of the line-of-sight spectral brightness and rotational temperature. A λ^{-4} variation in Rayleigh scattering cross-section is also considered in the fitting. Continuum brightnesses of $\sim 5.0 \times 10^4$ R/Å and $\sim 2.5 \times 10^4$ R/Å at a tangent height of 60 km are obtained at 7570 Å and 8570 Å, respectively. In fact, the brightness ratio is found to be ~ 1.8 and increases slightly as the tangent height increases. The solar incident fluxes at the top of the atmosphere are 4.75×10^{13} photons/cm²/sec/R/Å and 4.31×10^{13} photons/cm²/sec/R/Å at these two wavelengths, respectively. The Rayleigh scattering cross-section at 7570 Å is about a factor of 1.64 larger than at 8570 Å, giving rise to a ratio of approximately 1.8 for the Rayleigh scattering brightness. This agrees very well with the ratio we observed, indicating that our absolute sensitivity calibration is likely to be correct (at least the relative sensitivity between the two spectral regions). If this is true, it would imply that the ratio of (0-0) band intensity to (0-1) band intensity is indeed ~ 14.0 instead of the theoretical value of 20.0. This discrepancy is currently being re-investigated using the measurements taken from the second MAP rocket flight. We would like to point out, however, that the simple analysis conducted here assumes that the molecular scattering (ν^4 dependence) is solely responsible for the observed continuum emission and the DATES spectral response is

60

independent of the polarization of the incoming light. Depending upon the orientation of DATES with respect to the incoming sunlight, the Rayleigh scattered light should be polarized. If the spectral response of DATES varies with the polarizability of the scattered light, this could give rise to the discrepancy we found here. In addition, it would also affect our temperature analysis if one does not accurately know the spectral shape of the continuum emissions. This issue will be addressed as the data taken from the second MAP flight become available.

In addition, as revealed in Fig.34, the observed continuum brightness at 7570 Å is $\sim 5 \times 10^4$ R/Å, which is approximately a factor of 2 brighter than the one predicted by the theory based on the our measured atmospheric density, the unattenuated solar flux, and the solar azimuth angle ($90°$) when the measurements were made. Although this could also result from either an error in our absolute sensitivity calibration or the lack of sensitivity calibration for polarized light, it is highly unlikely that we made a 100% error in our sensitivity calibration. We believe that this is a result of the optical component we used in DATES on the first MAP flight. The brightness of the Earth's limb increases exponentially as the tangent height decreases. Observing from space at ~ 200 km, the observation line-of-sight decreases 2 km every $\sim 0.05°$. For example, the Earth's surface, which is $\sim 10^7$ R/Å in brightness, is only about $1.5°$ below the line-of-sight for a measurement at 60 km tangent height. In order to accurately measure the line-of-sight spectral brightness, one needs to have a telescope system which minimizes the bright Earth as much as possible. As described previously, we have carefully designed the telescope baffle to reject off-axis scattered light using a two stage baffle system. This would only minimize the large angle scattering angle such as the bright Earth. For small angle scattering off the primary optical component used in DATES-1, it is also important that the brighter signal coming from the brighter limb should also be rejected as much as possible. This requirement becomes more stringent as the altitude of the observation platform becomes higher. The primary optics used in DATES-1 is a refractive lens, which is not good enough for small angle scattering rejection. The reflective mirrors are usually used for stringent small angle scattering requirements. Consequently, we have redesigned the telescope system for the DATES instrument to be flown on the next MAP flight. Instead of using a refractive lens as our primary optics, a sun-shade, using two identical parabolic mirrors, is added to collect the light and feed it to the imaging lens used in DATES-1. The new design of the telescope system will be described in the next section where the conceptual satellite instrument is given.

3.3 A Proposed Satellite Experiment

3.3.1 Orbit Selection

The nature of satellite orbits determines the coverage of DATES measurements. Near-polar orbits will permit measurements to be conducted over the entire latitude region. These orbits, however, do not precess rapidly enough to provide adequate local time coverage to study the tidal effect. Conversely, lower inclination orbits can precess rapidly enough to cover a full diurnal cycle before

61

the season changes. But these orbits provide limited latitudinal coverage. Therefore, there is no ideal orbit which can both provide latitudinal coverage and can precess rapidly enough to allow the seasonal variation of tides to be studied.

Here we will not discuss what type of orbit one should select. This would depend upon the overall scientific objectives of the mission. However, in order to simplify the DATES operation, we would prefer to conduct the experiment in a circular orbit with altitude less than 800 km. In addition, no matter what type of orbit, high inclination versus low inclination and sun synchronous or nonsynchronous, the nature of the DATES inversion gives rise to different degrees of measurement accuracy and can be evaluated.

As described in the previous sections, one-dimensional (altitude) inversion of the density and temperature from DATES spectral measurements assumes horizontal homogeneity (horizontally stratified). That is,

$$\eta_1(z) = \eta_2(z) \tag{3.60}$$

where η_1 and η_2 are the band volume emission rates at altitude z for the two points on either side of the tangent point. As indicated by the theoretical calculation of Bucholtz et al. (1986), the O_2 Atmospheric band volume emission rate is a strong function of the solar zenith angle. Consequently, in order to minimize the systematic error introduced by the breakdown of the above assumption, one needs to select an orbit such that the line-of-sight variation in solar zenith angle is small. The advantage and disadvantage of various orbit types (different sun β angles) will be discussed. For a line-of-sight viewing direction parallel to the satellite velocity vector and

(1) an orbit with sun β angle of 90°,

Advantage:
Very little systematic error is introduced by the horizontal homogeneity assumption. The assumption is satisfied since the solar zenith angles at the tangent point remain nearly constant at 90°.

Disadvantage:
Larger statistical error in the recovered density and temperature profiles is present because the band volume emission rate is weaker and the measured DATES signal-to-noise ratio is small.

(2) an orbit with sun β angle of $0°$,

Advantage:

Smallest statistical error in the recovered density and temperature profiles is present because that band volume emission rate is the largest and the best DATES signal-to-noise ratio can be obtained.

Disadvantage:

Along the line of sight, η_1 and η_2 can be noticeably different due to the difference in solar zenith angles. Consequently, the largest systematic error is introduced by the possible breakdown in the homogeneity assumption.

(3) an orbit with sun β angle of $50°$:

This is an ideal orbit to provide measurements with reasonable statistical errors (increase the error probably by ~20%) and still satisfies the homogeneity assumption.

3.3.2 Conceptual Instrument: DATES-2

The conceptual picture of DATES-2 is illustrated in Fig. 35. It consists of a low scattered, baffled telescope, a 1/8 meter Ebert-Fastie spectrometer, and a Charge-Couple Device (CCD) detector system.

The optical characteristics of the DATES-2 instrument are determined by the desire to view the Earth limb from a space platform at 600 to 800 km with a 2 km vertical resolution and to perform the measurements in a reasonable time period (long enough to achieve desired measurement accuracy and short enough to avoid spatial smearing). These desires are achieved within the constraints imposed by the need to baffle the instrument against a brighter signal coming from lower tangent heights and the bright surface, especially for observations made from a space platform above 600 km. Consequently, a telescope system different from the one used in DATES-1 will be used. Our previous DATES-1 measurements have demonstrated the need to cool the CCD detector to decrease the dark current generation. DATES-1 uses a thermal-electric cooler in conjunction with an ice-bucket heat sink to cool the CCD and maintain it at approximately -37 C during the short rocket flight (order of minutes). DATES-2 will replace it by using in-flight cooling to deep space with a thermal radiator. A summary of DATES-2 instrumental parameters is shown in Table 4.

SCAN MIRROR

35 CM

20 CM

3.5 Kg TELESCOPE

Fibre Optic

TELESCOPE MIRROR

NOT TO SCALE

8 cm. Wide (includes some Detector Electronics)

Entrance Slit

Flat Grating

Dispersion

CCD and Cooler
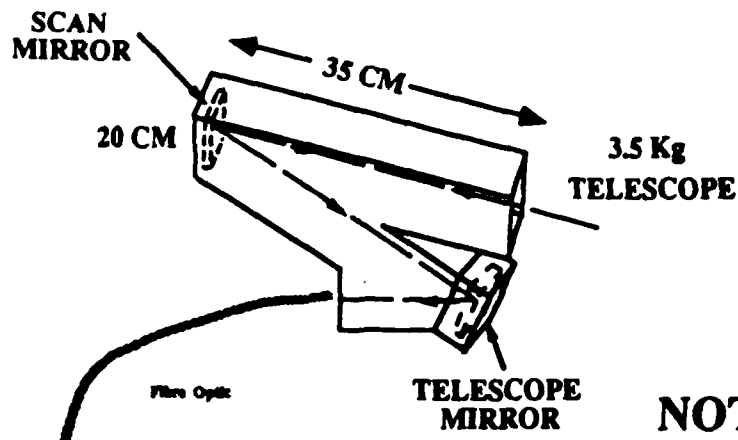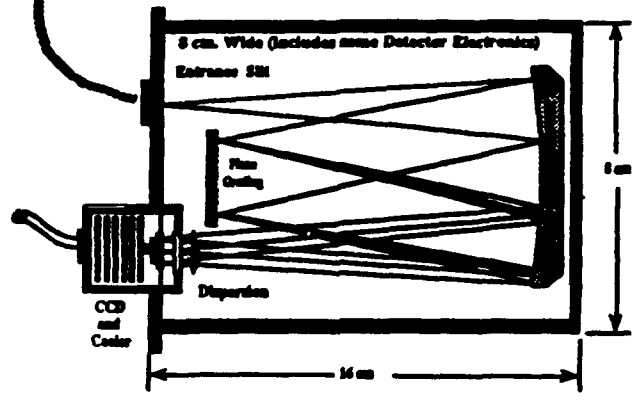
DENSITY AND TEMPERATURE SOUNDER DATES

1.4 Kg

TOTAL WEIGHT 9.4 Kg

POWER
  AVERAGE 14.6 Watts
  PEAK   25   Watts

17.5 CM

20 CM

INTERFACE

LOGIC DECK

CCD DECK

MOTOR DRIVE

POWER SUPPLY

14 CM
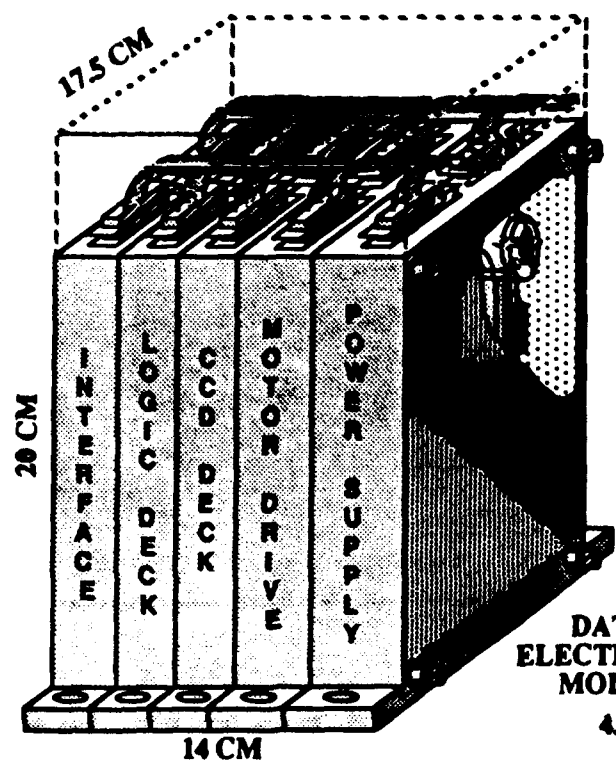
DATES ELECTRONICS MODULE

4.5 Kg

Figure 35

Table 4. Instrumental Parameters of Satellite Instrument DATES-2

PARAMETER	VALUE
Orbit Shape	Circular
Orbit Altitude	~ 600-800 km
Look Direction	+ or - Velocity Vector, 80 km nominal
Instantaneous FOV	2 x 110 km, 0.045° x 2.4°
Integration Time	2 seconds
Vertical Scan Time	60 seconds
Along Track Resolution	960 km, Integration Time 500 km, Geometry
Spectral Bands	O_2, 0-0, 0-1, 7650 Å, 8620 Å
Spectral BandWidth	~270 Å
Spectral Resolution	~5Å
Wavelength Elements	32
Horizontal Resolution Elements	25x4 km
Data Rate	1350 bps x 60% = 810 bps
Size	See Figure
Mass	9.4 kg
Power	14.6 W, average 25 W, peak

3.3.2.1   Instrument Description

Telescope and Baffle: The primary functions of the DATES-2 telescope are to define an atmospheric region with an instantaneous field of view of 2 km vertical by 160 km horizontal, to view in the forward (or reverse) velocity vector direction, to provide vertical scanning from 60 to 120 km, and to provide low off-axis both large- and small-angle scattering to eliminate scattering from the lower atmosphere and bright surface.   To accomplish these functions, an off-axis Gregorian configuration is baselined utilizing a high polish, low scatter, off-axis parabolic section primary mirror. A relay optic configuration is employed to pass the primary image through a simple scan mirror to the image field stop.   For a satellite position at 600 km above the earth, a height resolution of 2 km gives rise to a vertical field-of-view of 0.0425° and 0.04498° at 60 km and 120 km tangent height, respectively.   The physical dimension of the slit width is then 0.185 mm for a 250 mm telescope. Since the scan range required for a tangent height scan between 60 and 120 km is less than 2°, a scan mirror can be used to eliminate the need to move the entire telescope.   A simple baffle is used to preclude direct sun from striking the primary optic, and an ejectable cover is employed to maintain cleanliness within the telescope and to preserve the low scatter properties.   Image integrity is maintained and as will be described later, this approach permits the CCD detector to provide horizontal structure information if necessary.   The output of the telescope is either directly imaged onto the 1/8 meter Ebert-Fastie grating spectrometer, or, if

65

spacecraft accommodation dictates, a coherent fiber optic cable can be used to couple the telescope with the spectrometer in order to provide flexibility in the spectrometer location.

Ebert-Fastie Spectrometer : A conventional 1/8 meter Ebert-Fastie grating spectrometer is used to provide spectral separation of the two O_2 Atmospheric bands at 7620 Å (0-0 band) and 8650 Å (0-1 band), respectively. A holographic grating with 1/1800 lines/mm rules lines will be used. It gives a dispersion at the exit position in the focal plane of 27.34 Å/mm, or a spectral resolution ~5.1 Å (0.185 mm slit width) and a spectral coverage of ~ 270 Å over the entire face of the CCD detector (512x512 pixels at 20x20 μm per pixel). The spectrometer grating will be operated on the first interference order for the measurements of (0-0) and (0-1) bands spectral regions. A blocking filter which eliminates the photons with wavelengths shorter than 6000 Å will be installed to prevent the photons of higher order dispersion from reaching the detector. A simple stepper motor and gearhead combination with a position detector is used for band selection. An f/5 optical system is selected to provide good image quality with a simple spherical optic. The baseline design assumes a 0 to 30°C operational temperature range. The CCD detector is cooled separately, and it eliminates the need for active thermal control of the grating spectrometer.

CCD Detector: A charge coupled device (CCD) similar to that employed successfully on the sounding rocket has been selected as the detector. It provides high quantum efficiency, horizontal imaging, and simultaneous measurements across the spectral band. A typical CCD will provide >30% quantum efficiency in the two spectral regions of interest. There are newly developed CCDs with a physical dimension larger than the one we used on DATES-1 and significantly low thermal noise. Choosing a CCD of 512 x 512 pixels at 20 x 20mm per pixel size and imaging the input slit onto the surface of the CCD, we can obtain a horizontal resolution of ~110 km or effective field-of-view of 0.04° x 2.4°.

In order to reduce CCD thermal background to acceptable levels and to permit operation in the radiation environment of space, the CCD needs to be cooled to approximately -100°C. This can be accomplished with a direct thermal radiator to deep space or a thermoelectric cooler coupled to a thermal radiator. The method employed is dependent on the spacecraft configuration. The baseline approach here assumes a direct couple to deep space.

Electronics : As shown in Fig. 35, the electronics are comprised of a low voltage power supply, (LVPS), a motor drive deck (MD), a CCD data deck (CD), a logic deck (LD), and a spacecraft interface deck (SI). The lower voltage power supply is based on a Space Physics Research Laboratory (SPRL) "Universal" design which can accommodate virtually any nominal spacecraft interface. Input power from ±22 to 50 VDC, primary isolation, current limiting, EMI/EMC performance are all provided. The motor drive is also based on a simple generic SPRL design to operate stepper motors and to read mechanism position. The baseline stepper drive design employs a simple "slow step" approach which will step the telescope scan mirror and/or the grating in less than 50 ms. A more complex, 'fast step' design is available which could reduce the step time to

66

less than ~20 ms. The CCD decks (2 required) contain the double correlated sampling electronics to read the output of the CCD and the logic to sum the 1/4 second integration time into the 2 second normal mode integration time.

The logic deck provides the timing signals required to operate the CCD and is under command control from the spacecraft interface deck. The spacecraft interface deck provides data and command logic interfaces to the spacecraft data and command system.

3.3.3   DATES-2 Operational Modes

Spectral Binning: Through electrical shift timing control the two-dimensional dispersed spectra registered by the CCD, 512 x 512 pixels, will be redivided or 'binned' into 32 spectral elements and a number of horizontal elements. Each binned spectrum will represent a line-of-sight spectrum at an Earth's limb of 2x25 km. This binning pattern allows us to obtain two-dimensional measurements of the density and temperature profiles. If the horizontal element is set to 1, a measurement scheme similar to the one used in the MAP rocket flight will be obtained.

Measurement Sequence and Spatial Resolution: An integration time of 2 seconds at one tangent height is required for the normal operating mode. Since two wavelength bands are used at each altitude increment, 4 seconds are needed for each altitude step. In order to complete a scan from 60 to 120 km at an altitude step of 2 km, a total of 30 steps or 60 seconds are needed. For a nominal spacecraft velocity of ~8 km/sec, this gives rise to an along-the-track horizontal resolution of 960 km. Since the Earth is not a perfect sphere, the oblateness of the Earth (smaller radius near the poles) will make the lowest tangent height higher as the satellite approaches the poles if a set of preset telescope elevation angles are used. Two options can be adopted to solve this oblateness problem. First, one can correct the elevation angle (or telescope stepping motor position) by one step every time the limb altitude changes by 2 km. This, however, requires the spacecraft to issue oblateness commands to the DATES control computer and it requires additional hardware to accomplish the task. This approach is possible but has never be used and tested. For DATES-2, we intend to take the second option of simply overscanning the altitude profile by ~ 20 km, for example, between 40 and 120 km. This would allow the measurements at 60 km to be made at the high latitude region. The trade-off for this is that one has to spend an additional 40 seconds in one vertical scan and consequently the along-the-track horizontal resolution becomes ~1300 km. In order to improve the horizontal resolution, we would also suggest examining the possibility of having two CCDs measuring both spectra simultaneously without having to change the grating position. This not only reduces the time period used in one vertical scan by half, but also removes the mechanism for controlling the grating position. Preliminary investigation indicates that this is a viable approach and should be further explored.

Telemetry: A basic integration time of 0.25 sec is selected to prevent saturation of the CCD pixels at the low tangent and to provide a high temporal resolution operating mode. The maximum, or its

67

basic data rate, then becomes 32 x 4 data channels at 16 bits/channel, or 8,192 bits/sec (bps). The data will be summed off chip to provide a normal mode integration time of 2 seconds. It gives a nominal science data rate of 1,024 bps or an instantaneous data rate of 1,350 bps if a science and engineering overhead of 30% is considered. Since we expect the instrument to be operated in the daytime only, the average orbital data rate is thus 1,350 x ~60%, or 810 bps, for a sun synchronous orbit.

3.3.4 Accuracy Assessment

Statistical Error: The statistical error is commonly associated with the photon counting statistics (usually follows the Poisson distribution) and is directly related to the instrument sensitivity. The higher the signal level is, the more accurate the recovered quantity will be. In other words, the statistical accuracy can be improved by increasing the integration time of each individual measurement. This, however, alters the total integration time in one vertical scan and results in a different horizontal spatial coverage. Consequently, the accuracy requirement of the measured quantity dictates the design of the instrument and the operational modes.

The current design of DATES-2 has a sensitivity similar to the one flown on the MAP rocket. Our error analysis (based on the analysis described in Appendix I) indicates that a statistical error of 2K will be obtained for the temperature profile and 5% for the density profile.

Systematic Error: The systematic error arises from (1) the sensitivity calibration, (2) the ratio between the transition probabilities of the O_2 Atmospheric (0-0) and (0-1) bands, and (3) the uncertainties in our knowledge of the emission and absorption line strengths and their temperature dependence. Since the temperature measurements are carried out by observing the optically thin, non-absorbing O_2 Atmospheric (0-1) band emission. Accurate temperature measurements require not only the knowledge of the temperature dependence of line strengths but also the sensitivity variation within the (0-1) band spectral region (~250 Å). The temperature dependence of each individual line strength is given by

$$f = f_s \frac{T_s}{T} \exp\left\{\frac{1.439 E'(T - T_s)}{T\,T_s}\right\}, \tag{3.61}$$

$$\sigma = \sigma_s \frac{T_s}{T} \exp\left\{\frac{1.439 E''(T - T_s)}{T\,T_s}\right\}, \tag{3.62}$$

where f_s is the emission line strength at standard temperature T_s, σ_s, is the self-absorption cross-section at T_s, and E' and E'' are the energies in cm^{-1} for the upper and lower states of the rotational line respectively (Babcock and Herzberg, 1948).

The error introduced by the uncertainty of this temperature dependence is negligible, since the energies of the upper rotational states are accurately known (it relates directly to the line position). The sensitivity variation within the spectral region can be well-calibrated before flight and will be carefully monitored in-orbit using incandescent lamps or direct moon measurement to minimize this possible error. The spectral information will also be calibrated in-orbit using Ne spectral lamps to monitor the spectral drift.

The density measurement is accomplished by observing the ratio of the signals between the nonabsorbing (0-1) and the self-absorbing (0-0) bands of emission in the lower mesosphere. Consequently, for the measurements of O_2 density profile, absolute sensitivity is not critical but relative sensitivity between the two is crucial. If both emissions are optically thin, such as the measurements above 100 km tangent height, this ratio is directly related to the transition probabilities of the two emission bands (or Franck-Condon factors). The relative sensitivity thus can be monitored constantly and corrected if necessary by examining the intensity ratios between the two bands from measurements taken above 100 km tangent height. Incandescent lamps will also be used to calibrate this important ratio.

The error introduced by the uncertainty of the temperature dependence of the absorption cross-section is also insignificant since the energies of the lower rotational states are accurately known [Eqs. (3.61) and (3.62)]. The error introduced by the uncertainty of the absolute emission line strength (for temperature measurement) and the absorption cross-section (for density measurement) from line to line will be investigated by possible correlative groundbased Rayleigh lidar measurements. Once the ground truth is established, at least between 50 and 60 km, this source of error will be minimized. By the time the satellite instrument is in orbit, lidar measurements should be able to provide density and temperature profiles up to 100 km. By comparing the results obtained from these two technique, the error introduced by the uncertainty of the absolute line strengths can then be easily minimized.

Pointing and Satellite Position Error: This error arises mostly from the uncertainty of the tangent height determination. An uncertainty of 0.3 km in altitude would give rise to a 5% uncertainty in density in an exponential atmosphere with a scale height of 7 km. Remote measurements of density thus require very accurate *a posteriori* knowledge of the satellite altitude (~ 1 km in 3σ) and the instrument pointing especially in the pitch angle (~ 80 arc seconds in 3σ). Minor sources of error also arise from the uncertainty of the instrument roll and yaw angles. In our case, they are directly related to the horizontal imaging of the Earth's limb and a less stringent 1° 3σ accuracy is thus required. In-orbit pointing calibration, as discussed in the next section, will be provided every four minutes (can easily be changed if necessary) to achieve the required accuracy.

3.3.5   In-orbit Calibration

Spectral Radiometric Calibration: Spectral radiometric calibration will be provided by a neon spectral lamp as is currently done in the sounding rocket instrument, with a second lamp provided for redundancy. A simple tungsten lamp similar to that currently used by the NASA UARS/HRDI instrument will be used to provide routine in-band calibration and band-to-band relative sensitivity calibration. Since tungsten lamps are known to degrade with usage, for redundancy purposes, a second lamp will also be flown. The second lamp will not be used very often, and its only function will be to monitor the performance of the primary lamp. As noted above, the measurements taken above 100 km tangent height can also provide a tool to monitor the relative sensitivity changes between bands. As a further cross check on the above calibrations, a direct observation of the moon may be employed by rotating the spacecraft, if necessary. The specific location of the calibration lamps will be determined during detailed design, but they will likely be position-added to the altitude scan mirror similar to the technique employed on the DE/FPI.

Pointing Calibration: Although outside the baseline design approach, our preliminary analysis suggests that the instrument can provide pointing accuracy calibration by 2-dimensional imaging of the star field. This would be accomplished by operating the spectrometer in the 0th order to achieve maximum signal and direct imaging the field-of-view onto the CCD linear detector. Preliminary sensitivity calculations indicate that stars down to 10th magnitude may be observable, providing more than an adequate number of stars for observation. The CCD binning pattern would be altered, providing 4 reads in the 'spectral' direction (vertical field-of-view) and 32 reads in the 'horizontal' direction (horizontal field-of-view) in every 0.25 second to maintain similar telemetry stream format. A vertical star crossing thus would be observed with a precision better than ~1/5 of a vertical field-of-view or ~0.01°. This is about one half of the required pointing accuracy in pitch angle. Horizontal angular determination would have an accuracy ~ 2.4°/32 = 0.075° which is much better than what is needed for the 1° yaw requirement. Having 0.01° resolution in pitch and a 1.2° half-angle in yaw, one can easily determine the roll angle to 0.15° which is also adequate to meet the 1° roll requirement.

A data rate about four times faster would be required temporarily in this mode of operation. The measurement frequency will be determined by the spacecraft's motion and as part of an iterative design process with the spacecraft attitude control designers. Our previous MELTER Phase A study indicates that this type of measurement could be required as often as every 4 minutes. If it is required, we expect to perform this type of calibration following the highest tangent height measurement (at 120 km) in an upward telescope scan.

# 4. Measurements of O(^{1}D) and O$_3$ Number Densities

As has been clearly described in the scientific objectives of the DATES mission, the mesosphere and lower thermosphere (60-120 km) is a region characterized by complex and coupled radiative, chemical and dynamical processes. The major chemical processes in the mesosphere involve rapid interactions between the odd oxygen (O and O$_3$) and odd hydrogen (OH, H, HO$_2$) species. O$_3$ is important because of its role in the radiation (thermal) budget of the atmosphere. The concentration of ozone in this region of the atmosphere has usually been indirectly inferred from the O$_2$($^1\Delta$) 1.27 μm emission produced by the photolysis of O$_3$. Results from previous studies have shown that the abundance of ozone in the upper stratosphere and lower mesosphere exceeds the value predicted by various theoretical models by 30% in the lower mesosphere to almost a factor of 2 near the mesopause. Thus comprehensive measurements of ozone are vitally important in solving this perplexing problem.

The concentration of O(^{1}D) atoms in the upper stratosphere, mesosphere and lower thermosphere is low, approximately 10^2-10^3 cm^{-3}, and is very difficult to measure through the 6300Å emission because of the presence of Rayleigh scattering. As described before, the O(^{1}D) atoms are very important due to their involvement in the HO$_x$ chemistry, i.e. O(^{1}D) + H$_2$O → 2OH and O(^{1}D) + H$_2$ → H + OH. They are also important because of their role in the heat source from the quenching collisions.

The number densities of both the metastable O(^{1}D) atoms and O$_3$ molecules can be derived from the measured O$_2$($^1\Sigma$) number density profile simultaneously with the atmospheric density and temperature measurements. DATES will provide, for the first time, a viable technique to infer the concentrations of these two important O$_x$ species along with the concentration of the major species, O$_2$ and atmospheric temperature.

Here we will demonstrate how accurate O(^{1}D) and O$_3$ density profiles can be deduced from measured temperature, O$_2$($^1\Sigma$), O$_2$, and N$_2$ density profiles. The validity of our techniques assumes that all O$_2$($^1\Sigma$) in the atmosphere is produced by the following four mechanisms:

1) electronic quenching of O(^{1}D) by O$_2$, via O$_2$ photodissociation:

$$O_2 + h\nu \ (140nm<\lambda<176nm) \rightarrow O(^1D) + O(^3P)$$
$$O(^1D) + O_2 \rightarrow O_2(^1\Sigma) + O(^3P)$$
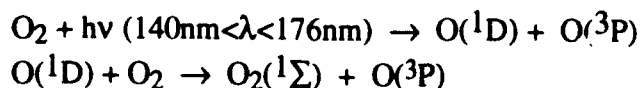
2) electronic quenching of O(^{1}D) by O$_2$, via O$_3$ photolysis:

$$O_3 + h\nu \ (175nm < \lambda < 310nm) \rightarrow O(^1D) + O_2$$
$$O(^1D) + O_2 \rightarrow O_2(^1\Sigma) + O(^3P)$$
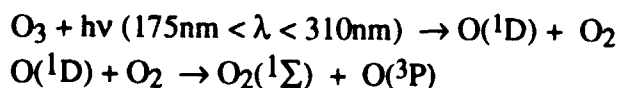
3) O_2 resonance scattering:

$$O_2 \, (^3\Sigma) + h\nu \, (\lambda \approx 762nm) \; \rightarrow \; O_2(^1\Sigma, \upsilon'=0)$$
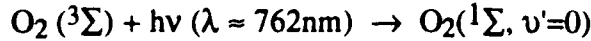
4) chemical process of O recombination (the Barth process):

$$O + O + M \rightarrow O_2^* + M$$
$$O_2^* + O_2 \rightarrow O_2(^1\Sigma) + O_2$$

If we denote the various sources of production of $O_2(b^1\Sigma_g^+)$ by P_{res}, $P_{O(^1D)}$ and P_{chem}, and consider loss processes due to quenching and radiation in a simple photochemical equilibrium situation, we can write the total band volume emission rate as a function of altitude,

$$\eta_{\upsilon\upsilon'}(z) = A_{\upsilon\upsilon'} \frac{P_{res} + P_{O(^1D)} + P_{chem}}{A_{1_\Sigma} + k_{N_2} n_{N_2}(z) \, k_{O_2} n_{O_2}(z)}, \tag{4.1}$$

where $A_{\upsilon'\upsilon''}$ is the transition probability between $O_2(b^1\Sigma,\upsilon')$ and $O_2(X^3\Sigma,\upsilon'')$ states, A_{1_Σ} is the transition probability of the $O_2(b^1\Sigma)$ state, and k_{N_2} and k_{O_2} are the quenching rate coefficients of $O_2(b^1\Sigma)$ by N_2 and O_2, respectively.

The method to measure the $O(^1D)$ density profile relies on accurately accounting for all $O_2(^1\Sigma)$ that is produced by O_2 resonance scattering and O recombination. The contribution from the O_2 resonance scattering can be calculated based on the O_2 density (directly involved in the excitation and solar flux attenuation) and temperature profiles (indirectly involved in the excitation cross-section line shape) measured by DATES. The contribution from the chemical source can be calculated based upon the atomic oxygen density profile from a model (such as the MSIS 86) and atmospheric density (directly involved in the production) and temperature (indirectly involved through the temperature dependence of rate coefficient). By subtracting the calculated O_2 Atmospheric band emission of these two production mechanisms from the total volume emission rate measured simultaneously by DATES, one can find the magnitude of the emission rate produced by the reaction of $O(^1D)$ with O_2 and consequently use it to deduce the $O(^1D)$ density profile. It should be noted that the contribution from the chemical source is very small compared to the rest of the sources and the effect of not knowing the atomic oxygen density accurately is insignificant.

Similarly, the method to calculate the O_3 density profile relies on accurately accounting for all $O_2(^1\Sigma)$ that is produced by O_2 photolysis, O_2 resonance scattering, and O recombination. By calculating the volume emission rate profile of the $O_2(^1\Sigma, \upsilon'=0)$ - $O_2(^3\Sigma, \upsilon''=0)$ transition that

these three mechanisms produce and then subtracting it from the measured total volume emission rate profile, the volume emission rate profile of the $O_2(^1\Sigma, v'=0) - O_2(^3\Sigma, v''=0)$ transition caused by the photolysis of O_3 can be derived. From this value it is then possible to deduce the ozone density profile.

4.1 Measurement of O(^{1}D) Density

4.1.1 Determination of η Resulting from O$_2$ Resonance Scattering

O_2 resonance scattering is the direct excitation of $O_2(^3\Sigma)$ to $O_2(^1\Sigma)$ by solar radiation,

$$O_2\,(^3\Sigma) + h\nu\,(\lambda \approx 762nm) \rightarrow O_2(^1\Sigma, v'=0). \tag{R1}$$
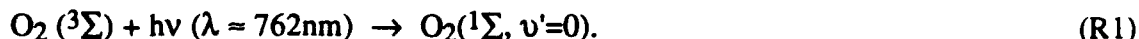
The production rate of $O_2(^1\Sigma)$ as a function of altitude can be calculated as:

$$P_{Res}[O_2(^1\Sigma)] = n_{O_2}(z)g(z) \tag{4.2}$$

where g(z) is the emission rate factor defined by

$$g(z) = \int_\nu \pi F(\nu,z)\sigma_{abs\,O_2}(\nu)\,d\nu \quad . \tag{4.3}$$

Here $\pi F(\nu,z)$ is the attenuated solar flux at frequency ν and altitude z,

$$\pi F(\nu,z) = \pi F(\nu,\infty)e^{[-\tau(\nu,z)]} \tag{4.4}$$

where $\pi F(\nu,\infty)$ is the unattenuated solar flux at the top of the atmosphere, and τ is the optical depth at altitude z,

$$\tau(\nu,z) = \sec\theta \int_z n_{O_2}(z')\sigma_{abs\,O_2}(\nu)\,dz' \quad . \tag{4.5}$$

Here θ is the solar zenith angle and the integration is carried out from the altitude of interest, z, to the top of the atmosphere. The solar flux at the top of the atmosphere, $\pi F(\nu,\infty)$, is 2.91 x 10^{13} photons cm^{-2} sec^{-1} and can be considered to be independent of wavelength in the spectral region (~200Å) of interest.

From $P_{res}[O_2(^1\Sigma)]$, the volume emission rate of $O_2(^1\Sigma)$ due to O_2 resonance can be determined by using the following equation:

$$\eta_{O_2\,Res\,O_2(^1\Sigma)}(z) = \frac{F_c P_{Res}[O_2(^1\Sigma)]A_{^1\Sigma}}{Quen} \tag{4.6}$$

where F_C is the Franck-Condon factor for the 0-0 emission and is equal to 0.9300, $A_{1\Sigma}$ is the Einstein coefficient for $O_2(^1\Sigma)$ and is equal to 0.085 sec^{-1}, and Quen is the sum of losses due to emission and electronic quenching given in the denominator of Eq. (4.1).

4.1.2   Determination of η Resulting from O Recombination

The production of $O_2(^1\Sigma)$ by O recombination can be expressed by the following two equations:

$$O + O + M \rightarrow O_2^* + M \tag{R2}$$

and

$$O_2^* + O_2 \rightarrow O_2(^1\Sigma) + O_2 \tag{R3}$$

$$O_2^* + O \rightarrow O_2 + O \tag{R4}$$

$$O_2^* \rightarrow O_2 + h\nu \tag{R5}$$

where M represents any other atmospheric molecule (such as O_2 and N_2), and O_2^* represents an O_2 molecule in a higher electronic state than $O_2(^1\Sigma)$. The rate coefficients for reactions R2 and R3, k_2 and k_3, have been reported to be 4.7×10^{-33} $(300/T)^2$ cm^6 s^{-1} and 5.0×10^{-13} cm^3 s^{-1}, respectively. Only a fraction, α, of the O_2 produced in the reaction R2 gives rise to the particular electronic excited state which can produce $O_2(^1\Sigma)$ through reaction R3. Similarly only a fraction, β, of the O_2^* produced in reaction R2 can turn into $O_2(^1\Sigma)$ in the quenching reaction of R3. In addition, the O_2^* produced in reaction R2 can also be quenched by atomic oxygen with a rate coefficient of $k_4 = 3 \times 10^{-11}$ cm^3 s^{-1} and radiate. Based upon the results of ETON rocket experiments obtained from the nightglow emissions (McDade et al., 1986), the combined efficiency factor $\alpha*\beta$, was measured to be ~0.80 and the effective $A_{O_2^*}$ is ~ 0.002 s^{-1}.

Hence, the production rate of $O_2(^1\Sigma)$ due to atomic oxygen recombination can be written as:

$$P_{Rec}\left[O_2\left(^1\Sigma\right)\right] = \alpha\beta\left[\frac{k_3 n_{O_2}(z) k_4 n_O(z)^2 n_M(z)}{A_{O_2^*} + k_3 n_{O_2}(z) + k_4 n_O(z)}\right]. \tag{4.7}$$

From this the volume emission rate of $O_2(^1\Sigma)$ can be determined by,

$$\eta_{O_2\,Rec\,O_2(^1\Sigma)}(z) = \frac{F_c P_{Rec}\left[O_2\left(^1\Sigma\right)\right] A_{1\Sigma}}{Quen} \tag{4.8}$$

where F_c, $P_{Rec}[O_2(^1\Sigma)]$, $A_{1\Sigma}$, and Quen have been defined previously.

4.1.3 Determination of O(^{1}D) Density

The O(^{1}D) atoms are mainly quenched in the lower thermosphere by N_2 and O_2,

$$O(^1D) + N_2 \; \longrightarrow \; N_2 + O(^3P), \tag{R6}$$

$$O(^1D) + O_2 \; \longrightarrow \; O_2^* + O(^3P). \tag{R7}$$

The total O(^{1}D) quenching rate by N_2 and O_2, k_5 and k_6, have been measured to be 2.3×10^{-11} and $2.9 \times 10^{-11} \, e^{67/T}$ cm^3 sec^{-1}, respectively. Following the electronic quenching of O(^{1}D) by O_2, some of the O(^{1}D) excitation energy (~1.96 eV) can transfer to the O_2 molecules and excite them to the $^1\Sigma$ state. The probability was found to be ~75% in the laboratory by Slanger (1981). Hence one can express the production rate of $O_2(^1\Sigma)$ from the O(^{1}D) quenching as

$$P_{O_2 Phot \, and \, O_2 Phot}\left[O_2(^1\Sigma)\right] = k_7 n_{O_2}(z)(0.75)n_{O(^1D)}(z). \tag{4.9}$$

By subtracting the contributions made by O_2 resonance and O recombination from the measured total volume emission rate, the volume emission rate produced by O(^{1}D) (via O_2 and O_3 photolysis) can be determined,

$$\eta_{O(^1D) \, O_2(^1\Sigma)}(z) = \eta_{Total \, O_2(^1\Sigma)}(z) - \eta_{O_2 Res \, O_2(^1\Sigma)}(z) - \eta_{O_2 Rec \, O_2(^1\Sigma)}(z). \tag{4.10}$$

Using the volume emission rate $\eta_{O(^1D)}$ determined above, one can derive the production rate of $O_2(^1\Sigma)$ due to O(^{1}D) atoms as:

$$P_{O_2 Phot \, and \, O_3 Phot \, O(^1D)} = \frac{\eta_{O(^1D)O_2(^1\Sigma)}(z)Quen}{F_c A_{^1\Sigma}}, \tag{4.11}$$

and solve the number density of O(^{1}D) atoms,

$$n_{O(^1D)}(z) = \frac{\eta_{O(^1D)O_2(^1\Sigma)}Quen}{F_c A_{^1\Sigma} k_7 n_{O_2}(z)(0.75)}. \tag{4.12}$$

4.2 Measurement of O_3 Number Density

4.2.1 Determination of η Resulting from O_2 Photodissociation

The production of $O_2(^1\Sigma)$ attributed to O_2 photodissociation is a two step process. The first step is the production of O(^{1}D) from the photodissociation of O_2. The amount of O(^{1}D) produced at a

given altitude depends on the magnitude of the solar flux between 140 nm and 175 nm reaching that altitude and is given by:

$$P_{O_2Phot}[O(^1D)] = n_{O_2}(z) \int_v \pi F(v,z)\sigma_{ds\,O_2}(v)\,dv \qquad (4.13)$$

where $\pi F(v, z)$ is the solar flux at altitude z after attenuation by O_2 and O_3 along the ray path,

$$\pi F(v,z) = \pi F(v,\infty)e^{[-\tau(v,z)]} . \qquad (4.14)$$

Here $\pi F(v,\infty)$ is the solar flux at wavenumber v at the top of the atmosphere, and τ is the optical depth at z given by:

$$\tau(v,z) = \sec\theta \int_z n_{O_2}(z')\sigma_{ds\,O_2}(v)\,dz' + \sec\theta \int_z n_{O_3}(z')\sigma_{ds\,O_3}(v)\,dz' \qquad (4.15)$$

where θ is the solar zenith angle and the integration is carried out from the altitude of interest, z, to the top of the atmosphere.

There is an apparent difficulty in calculating τ in Eq. (4.15) if the O_3 density is unknown and needs also to be solved. This situation can be resolved by the following iterative method. First, the O_3 density is assumed to be zero at each altitude interval. One can then solve the contribution of O_2 emission from O_2 photodissociation and consequently the new ozone density profile from our measured total emission rate profile using a method described later. This new O_3 density profile, which should now be more accurate, can in turn be used to determine more accurately the contribution of O_2 emission from O_2 photodissociation resulting in an even better O_3 density profile. This process is continued until the O_3 density profile converges.

The density of $O(^1D)$ atoms produced by O_2 photodissociation at altitude z is given by:

$$n_{O(^1D)} = \frac{P_{O_2Phot}[O(^1D)]}{A_{^1D} + k_7 n_{O_2}(z) + k_6 n_{N_2}(z)} \qquad (4.16)$$

where $A_{^1D}$ is the Einstein coefficient for $O(^1D)$ and is equal to 6.81×10^{-3} sec^{-1}, k_6 is the quenching rate of $O(^1D)$ by N_2 and is equal to 2.3×10^{-11} cm^3 sec^{-1}.

Following the derivation in the previous section, one can also calculate the production rate of $O_2(^1\Sigma)$ and its contribution to the O_2 Atmospheric (0-0) band volume emission rate from the

photodissociation of O_2 by

$$P_{O_2,\text{Phot }O(^1D)}\left[O_2(^1\Sigma)\right]k_7 n_{O_2}(z)(0.75)n_{O(^1D)}(z) \tag{4.17}$$

and

$$\eta_{O_2,\text{Phot }O_2(^1\Sigma)}(z) = \frac{F_c P_{O_2,\text{Phot }O(^1D)}\left[O_2(^1\Sigma)\right]A_{^1\Sigma}}{\text{Quen}}. \tag{4.18}$$

4.2.2 Determination of O_3 Density

As stated earlier, the underlying assumption of this technique is that $O_2(^1\Sigma)$ has four production mechanisms: O_2 photodissociation, O_2 resonance scattering, O recombination, and O_3 photolysis. The volume emission rates of the subsequent emission in the (0-0) transition produced by O_2 photolysis, O_2 resonance, and O recombination can be calculated following the techniques described in the previous sections. The only contribution which is not known is the one due to O_3 photolysis, and it can be determined from the measured total emission rate by:

$$\eta_{O_3,\text{Phot }O_2(^1\Sigma)}(z) = \eta_{\text{Total }O_2(^1\Sigma)}(z) - \eta_{O_2,\text{Phot }O_2(^1\Sigma)}(z) - \eta_{O_2,\text{Res }O_2(^1\Sigma)}(z) - \eta_{O_2,\text{Rec }O_2(^1\Sigma)}(z) . \tag{4.19}$$

The production of $O_2(^1\Sigma)$ due to O_3 photolysis is very similar to the production due to O_2 photodissociation. The first step is the production of $O(^1D)$ via

$$O_3 + h\nu\ (175\text{nm} < \lambda < 310\text{nm}) \rightarrow O(^1D) + O_2^*. \tag{R8}$$
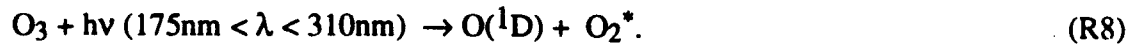
The $O(^1D)$ atom then reacts with O_2 to produce $O_2(^1\Sigma)$,

$$O(^1D) + O_2 \rightarrow O_2(^1\Sigma) + O(^3P). \tag{R9}$$

Similar to O_2 photodissociation, the amount of $O(^1D)$ produced by O_3 photolysis depends on both the solar flux and the dissociation cross-section for O_3, $\sigma_{\text{dis}O_3}$. Hence, the production rate of $O(^1D)$ in Reaction (R8) at an altitude, z, is given by:

$$P_{O_3,\text{Phot}}[O(^1D)] = n_{O_3}(z) \int_\nu \pi F(\nu,z)\sigma_{\text{dis }O_3}(\nu)\, d\nu \tag{4.20}$$

where $\pi F(\nu, z)$ is the solar flux attenuated by O_2 and O_3 and is calculated in the same manner as in Eq. (4.14). Consequently, the volume emission rate of $O_2(^1\Sigma)$ due to O_3 photolysis can be written as:

$$\eta_{O_3, \text{Phot } O_2(^1\Sigma)}(z) = \frac{F_c P_{O_3, \text{Phot } O(^1D)}\left[O_2(^1\Sigma)\right]A_{^1\Sigma}}{\text{Quen}} \qquad (4.21)$$

where $\eta_{O_3 \text{ phot}}$ is determined from the measurements, and F_c, $A_{1\Sigma}$, and Quen have all been defined previously. Solving Eq. (4.14) for $P_{O_3, \text{Phot } O(^1D)}$, one obtains,

$$P_{O_3, \text{Phot } O(^1D)}\left[O_2(^1\Sigma)\right] = \frac{\eta_{O_3, \text{Phot } O_2(^1\Sigma)}\text{Quen}}{F_c A_{^1\Sigma}}. \qquad (4.22)$$

Substituting Eq. (4.22) into Eq.(4.21), we have:

$$\frac{\eta_{O_3, \text{Phot } O_2(^1\Sigma)}\text{Quen}}{F_c A_{^1\Sigma}} = n_{O_3}(z)\int_v \pi F(v,z)\sigma_{\text{dis } O_3}(v)dv \qquad (4.23)$$

and the density of O_3 can then be determined by

$$n_{O_3}(z) = \frac{\eta_{O_3, \text{Phot } O_2(^1\Sigma)}\text{Quen}}{F_c A_{^1\Sigma}\int_v \pi F(v,z)\sigma_{\text{dis } O_3}(v)dv}. \qquad (4.24)$$

4.3 Error Assessment

We have implemented the above algorithms to recover number densities of $O(^1D)$ and O_3 based upon the $O_2(^1\Sigma,v'=0)-O_2(^3\Sigma,v''=0)$ volume emission rate profile calculated by the emission model of Bucholtz et al. (1986). The model generated an O density, N_2 density, O_2 density, temperature, and the emission rate profile. Because recovery of the $O(^1D)$ and O_3 number density is a highly non-linear problem, a Monte Carlo simulation technique was used to estimate how the errors in the band volume emission rate, atmospheric density and temperature profiles measured by DATES would affect the recovered $O(^1D)$ and O_3 density profiles.

Since measurement errors are generally assumed to have a standard normal distribution, the input profiles were first perturbed by randomly generated noises with zero mean and variance given by estimated errors that DATES measures. These perturbed profiles were then used to calculate the $O(^1D)$ and O_3 density profiles. This process of perturbing the inputs and then calculating the resulting $O(^1D)$ and O_3 density profiles was iterated for one thousand times, and the mean and the standard deviation of the resulting densities were calculated at each altitude. The derived mean $O(^1D)$ and O_3 density profiles are used to compare to the original inputs in order to test the validity of the recovery algorithm. The resulting standard deviations would indicate the statistical errors of the recovered $O(^1D)$ and O_3 densities for given errors in the measured total band volume emission rate, atmospheric density and temperature profiles. Figures 36 and 37 present the mean and errors of the recovered $O(^1D)$ and O_3 density profiles based upon estimated 5% errors for the O_2, and N_2 density measurements and 2% errors for the temperature and the total volume emission rate measurements under overhead sun conditions. Our analysis showed that, with simultaneous measurements of DATES, one can reasonably recover an $O(^1D)$ density profile with an accuracy of 5-20% and an O_3 density profile with an accuracy of 10-30% between 50 and 90 km.

It should be noted here that the error analysis performed here only represents the statistical errors. Any systematic errors arising from the uncertainties in our knowledge of solar fluxes, absorption cross-sections, rate coefficients, etc., were not included here. The remote sensing technique presented here is either the only existing one [for example, the $O(^1D)$ measurement] or similar to the one already developed [such as the O_3 measurement from $O_2(^1\Delta)$ emission following O_3 photolysis]. In conclusion, we believe that DATES, a simple optical remote sensing instrument, can provide measurements of many of the important atmospheric parameters needed for complete understanding of the complex chemistry, energetics and dynamics of the lower atmosphere.
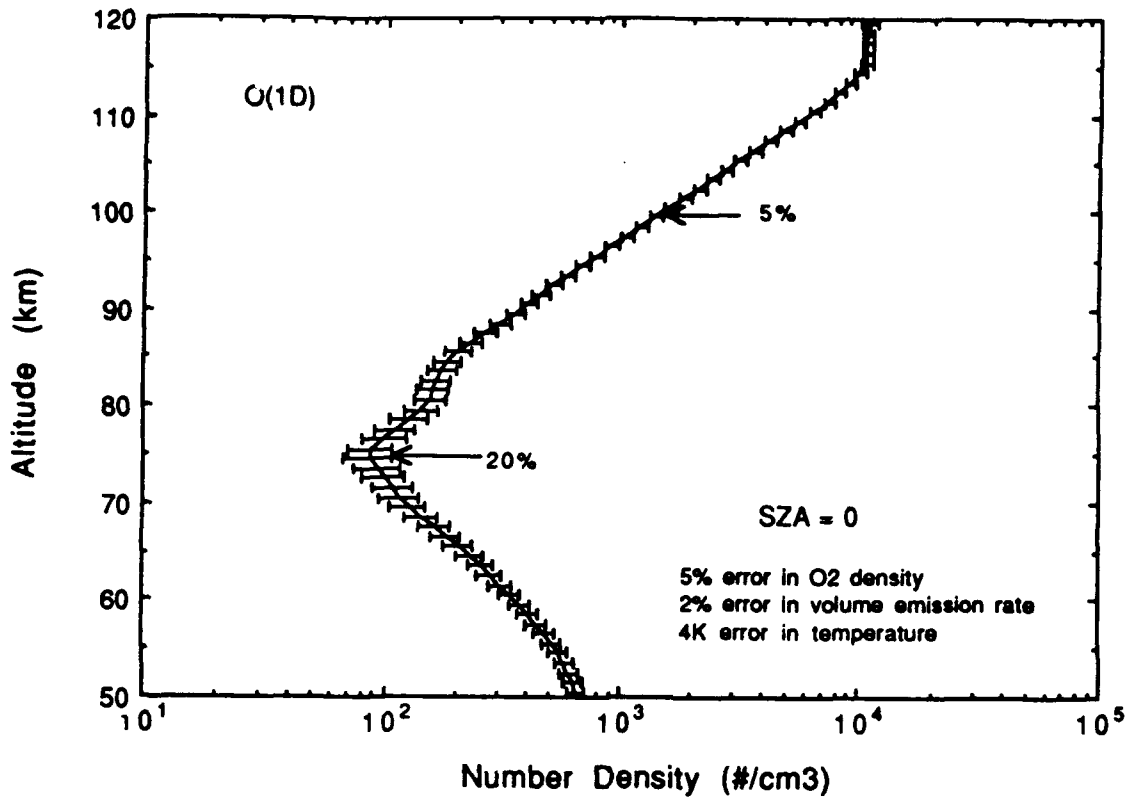
Figure 36
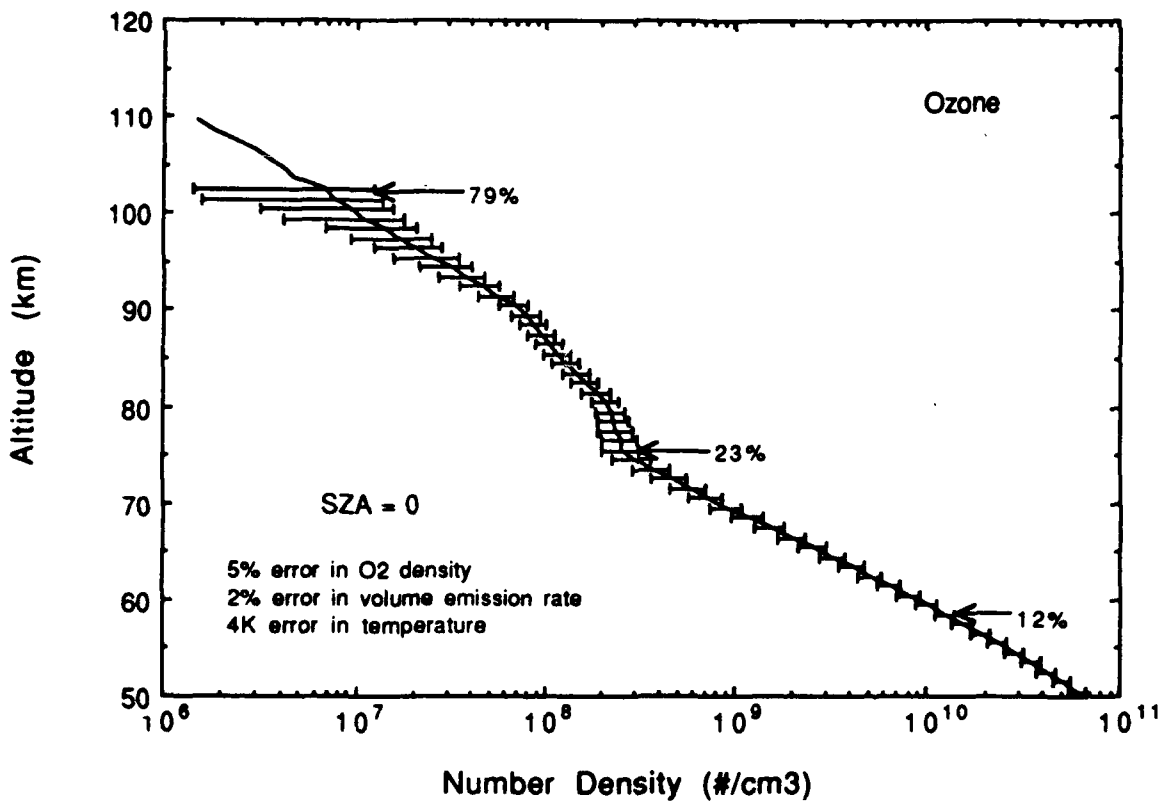
Figure 37

References

Babcock, H.D. and L. Herzberg (1948) Fine Structure and the Red System of Atmospheric Oxygen Bands, Astrophys. J., **108**, 167.

Banks, P. M. and G. Kockarts (1973) *Aeronomy*, Academic Press.

Bucholtz, A., W.R. Skinner, V. J. Abreu, and P. B. Hays (1986) The Dayglow of the O_2 Atmospheric Band system, Planet. Space Sci., **34**, 1031.

Dunkerton, T.J. (1982) Wave Transcence in a Compressible Atmosphere, 3. The Saturation of Internal Gravity Waves in the Mesosphere, J. Atmos. Sci., **39**, 1042.

Fesen, C.G., R.E. Dickinson and R.G. Roble (1986) Simulation of Thermospheric Tides at Equinox with the National Center for Atmospheric Research Thermospheric General Circulation Model, G. Geophys. Res., **91**, 4471.

Fuller-Rowell, T.J. and D. Rees (1981) A Three-Dimensional Time-Dependent Simulation of the Global Dynamical Response of the Thermosphere to a Geomagnetic Substorm, J. Atmos. Terr. Phys., **42**, 553.

Garcia, R.R. and S. Solomon (1983) A Numerical Model of the Zonally Averaged Dynamical and Chemical Structure of the Middle Atmosphere, J. Geophys. Res., **88**, 1379.

Garcia, R.R. and S. Solomon (1985) The Effect of Breaking Gravity Waves on the Dynamics and Chemical Composition of the Mesosphere and Lower Thermosphere, J. Geophys. Res., **90**, 3850.

Garcia, R.R., S. Solomon, S.K. Avery and G.C. Reid (1986) Transport of Nitric Oxide and the D-Region Winter Anomaly, J. Geophys. Res., submitted.

Gerard, J.C. and R.G. Roble (1986) The Role of Nitric Oxide on the Zonally Averaged Structure of the Thermosphere: Solstice Conditions for Solar Cycle Minimum, Planet. Space Sci., **34**, 131.

Hays, P.B., G.R. Carignan, B.C. Kennedy, G.G. Sheperd, and J.C.G. Walker (1973) The Visible Airglow Experiment on Atmosphere Explorer, Radio Sci., **8**, 369.

Hays, P.B., V.J. Abreu, C.R. Cornish, J.J. Horvath, M. Luo, W.R. Skinner, and J.H. Yee (1988) Remote Measurement of Upper Atmospheric Density: A Feasibility Study, Final Report, AFGL Report Number TR-88-0139. **ADA199292**

Hedin, A.E. (1987) MSIS-86 Thermospheric Model, J. Geophys. Res., **92**, 4649.

Holton, J.R. (1982) The Role of Gravity Wave Induced Drag and Diffusion in the Momentum Budget of the Mesosphere, J. Atmos. Sci., **39**, 791.

Holton, J.R. (1983) The Influence of Gravity Wave Breaking on the General Circulation of the Middle Atmosphere, J. Atmos. Sci., **40**, 2497.

Janesick, J. R., K.. Klassen, and T. Elloit (1987) Charge-Coupled-Device Charge-Collection Efficiency and the Photon-Transfer Technique, Optical Engineering, **26**, 972.

Killeen, T.L. and P.B. Hays (1984) Doppler Line Profile Analysis for a Multichannel Fabry-Perot Interferometer, Appl. Opt., **23**, 612.

Kurucz, R.L., I. Furenlid, J. Brault, and L. Testerman (1984) Solar Flux Atlus from 296 to 1300 nm, National Solar Observatory, Atlas No. 1.

Leovy, C. (1964) Simple Models of Thermally Driven Mesospheric Circulation, J. Atmos. Sci., **21**, 327.

Lindzen, R.S. (1967) Thermally Driven Diurnal Tide in the Atmosphere, Quart. J.R. Meteorol. Soc., **93**, 18.

Lindzen, R.S. (1968) The Application of Classical Atmospheric Tidal Theory, Proc. R. Soc., London, Ser. A., **303**, 299.

Lindzen, R.S. (1981) Turbulence and Stress Owing to Gravity Waves and Tidal Breakdown, J. Geophys. Res., **86**, 9707.

Luo, M. J.-H. Yee, and P.B. Hays (1988) Image Plane Detector Spectrophotometer: Application to O_2 Atmospheric Band Nightglow, Appl. Optics, **27**, 3255.

McClatchey, R.A., W.S. Benedict, S.A. Clough, D.E. Burch, R.F. Calfee, K. Fox, L.S. Rothman and J.S. Garing (1973) AFCRL *Atmospheric Absorption Line Parameters Compilation, Environmental Research Papers*, No. 434, AFCRL-TR-73-0096, National Technical Information Service, Springfield, Virginia. AD762904

McDade, I.C., et al. (1986) ETON 2: Quenching Parameters for the Proposed Precursors of $O_2(b^1\Sigma_g^+)$ and $O(^1S)$ in the Terrestrial Nightglow, Planet. Space Sci., **34**, 7889.

Roble, R.G., R.E. Dickinson and E.C. Ridley (1982) Global Circulation of the Thermosphere with High Latitude Plasma Convection, J. Geophys. Res., **87**, 1599.

Schoeberl, M.R., D.F. Strobel and J.P. Apruzese (1983) A Numerical Model of Gravity Wave Breaking and Stress in the Mesosphere, J. Geophys. Res., **88**, 5249.

Twomey, S. (1977) *Introduction to the Mathematics of Inversion in Remote Sensing and Indirect Measurements*, Elseview, New York.

Wasser B. and T. M Donahue (1979) Atomic Oxygen between 80 and 120 km: Evidence for Latitudinal Variation in Vertical Transport Near the Mesopause, J. Geophys. Res., **84**, 1287.